

MICROSPHERICAL PHOTONICS FOR ENHANCING RESOLUTION OF
OPTICAL MICROSCOPY AND SENSITIVITY OF FOCAL PLANE ARRAYS

by

Aaron Brettin

A dissertation submitted to the faculty of
The University of North Carolina at Charlotte
in partial fulfillment of the requirements
for the degree of Doctor of Philosophy in
Optical Science and Engineering

Charlotte

2018

Approved by:

Prof. Vasily Astratov

Prof. Glenn Boreman

Prof. Michael Fiddy

Prof. Yuri Nesmelov

Prof. Victor Cifarelli

©2018
Aaron Brettin
ALL RIGHTS RESERVED

ABSTRACT

AARON BRETTIN. Microspherical Photonics for Enhancing Resolution of Optical Microscopy and Sensitivity of Focal Plane Arrays. (Under the direction of PROF. VASILY ASTRATOV)

It is shown that the resolution of virtual images of dye-doped dielectric nanospheres obtained through dielectric microspheres can be increased beyond the classical diffraction limit by decreasing the period of nanoplasmonic array used for localized plasmonic structured illumination of these objects. In addition, it is also shown that post-imaging processing, which represents an intrinsic part of structured illumination microscopy, is not required for achieving the super-resolved images. This observation is interpreted due to the fact that the radiation of objects placed at the surface of nanoplasmonic arrays with sufficiently short periods can be almost completely redirected into folded dispersions of nanoplasmonic array, so that the diffraction orders responsible for super-resolution are more efficiently coupled to dielectric microspherical antenna compared to that for the uncoupled radiative modes.

Focal plane arrays (FPAs) are pixelated arrays of photo detectors which are widely used for imaging. The problem of uncooled mid-wave infrared (MWIR) FPAs is related to their large thermal noise. In this work, it is demonstrated that the surface area and thermal noise of pixels can be reduced without sacrificing their sensitivity by using integration with dielectric microspheres, which can be achieved by a novel method of suction assembly of microspheres in microhole arrays. In addition, it is demonstrated that alternative solution of this problem is offered by integration with microconical light concentrators, which can be fabricated by various well-established

technologies including the use of the Nanoscribe. Using a simplified two-dimensional (2D) model, it is studied how the photocurrent depends on the geometrical parameters of microcones and on the angle of incidence.

The photoinduced aggregation of nanoparticles is of interest for material science and nonlinear optics applications. Light-driven assembly of nanoplasmonic particles is observed as an optical memory effect taking place due to the aggregation of 20 nm gold nanoparticles in the illuminated regions of the substrate after full evaporation of the liquid suspension. It is shown that the level of photoexcitation intensity required for observation of this effect is several orders of magnitude smaller compared to that in the previous studies of photoinduced aggregation typically performed using intense laser illumination. It is also demonstrated in a preliminary way that the photoinduced aggregation is facilitated in the spectral range resonant with localized surface plasmon resonances in nanoparticles.

Inverse scattering algorithms are of interest for many applications; however, they are usually based on low refractive index contrast approximations and measuring the phase distributions. In contrast, Globally Convergent Inverse Scattering (GCIS) algorithms in principle should allow phasless image reconstruction for high refractive index objects. In order to test the operation of GCIS algorithms, high-index ($n \sim 2$) barium titanate glass microspheres were assembled directly at a silicon chip of a cell phone camera and the scattering patterns resembling the shape of the Airy disks were detected using a set of narrow spectral filters throughout a broad range of wavelengths in the visible regime. The results were found to be in a good agreement with the image calculations and can be used for the object reconstruction based on GCIS algorithms.

ACKNOWLEDGMENTS

Foremost, I wish my deepest gratitude to my advisor, Prof. Vasily N. Astratov. Over the past several years, he has patiently and continuously supported my research efforts with immense knowledge and insight. He has diligently prepared me for all of my scientific presentations, challenging me to know and understand the information as much as possible. Without his guiding hand, albeit oftentimes in a frustrating manner, the work presented in this dissertation would not be possible.

I would like to thank my committee members; Prof. Glenn Boreman, Prof. Michael Fiddy, Prof. Yuri Nesmelov, and Prof. Victor Cifarelli. The time and effort all of you have committed to the growth of both me and my career is greatly appreciated. I would also like to state my appreciation of Prof. Douglas Knight for pushing me to look at science in a more hands on manner, Prof. Susan Trammell for the invaluable guidance you gave throughout my undergraduate career, and Prof. Donald Jacobs for the invaluable guidance you gave me through my Master's degree.

I would like to state my appreciation to Prof. Mikhail Klivanov, Prof. Loc Nguyen, and Dr. Nikolay Koshev for their insight to the inverse scattering problem.

I am very thankful for Dr. Nicholas Limberopoulos, Dr. Augustine Urbas, and Dr. Dean Brown for enabling my internships at the Air Force Research Laboratory at Wright-Patterson Air Force Base. I am also thankful for stimulating interactions with Dr. Dennis Walker Jr., Dr. Jarrett Vella, Joshua Duran, Dr. Imran Vakil, Michael Noyola, Dr. Andrew Green. I am also very thankful for Andrew Browning, Jason Hickey, and Joseph Breedlove; without you the work at AFRL would not have

been possible.

I am grateful to Dr. Lou Deguzman, Dr. Robert Hudgins, and Scott Williams for their patience while teaching me how to operate the equipment in the UNCC optics center. I am also grateful to Elisabeth Butler, Wendy Ramirez, Elyse Poston, Renee Collins, and Mark Clayton for helping me through numerous complicated endeavors.

I am also grateful to Dr. Vladamir Liberman and Dr. Mordechai Rothschild from MIT Lincoln Laboratory for the invaluable insight to nanoparticle aggregation.

I am thankful to Dr. Patricia Pellett and Mrs. Amy Jablonski and Mrs. Jennifer Marks for their help working and operating different microscope systems.

During my graduate studies, I had the privilege of being a part of the Mesophotonics Laboratory at UNCC. The interaction between members, both current and past, has been invaluable. Discussions with Farzaneh Abolmaali and Dr. Kenneth Allen in particular have helped drive and steer my research to completion. Prof. Astratov has brought a multitude of people into the Mesophotonics Laboratory in which I have had the privilege to work with from Boya Jin, Cobey McGinnis, James Page, and Prof. Luiz Poffo all of which assisted in my development.

I was supported financially by the GASP award throughout my graduate studies. I am thankful for the Department of Physics and Optical Sciences, as well as the Department of Mathematics and Statistics for supporting me. My research assistantships in Prof. Vasily Astratov's Mesophotonics Laboratory were supported through his grants from the National Science Foundation.

Lastly, I would like to acknowledge that none of this would be possible without the love and support of my family to whom I dedicate this dissertation to.

TABLE OF CONTENTS

LIST OF FIGURES	x
LIST OF TABLES	xiv
CHAPTER 1: INTRODUCTION	1
1.1. Outline and Overview of this Dissertation	1
1.2. Photonic Nanojet	6
1.3. Localized Surface Plasmon Resonance (LSPR)	17
1.4. Super Resolution Nanoscopy	28
1.4.1. Scanning Near Field Coupling	30
1.4.2. Metamaterial Lenses	32
1.4.3. Non-Linear Effects	35
1.4.4. Theory of Microspherical Nanoscopy	36
1.5. Focal Plane Array Enhancement	40
1.5.1. Materials and Structure of IR Detectors	43
1.5.2. Microlens Array	48
1.6. Mie Theory	48
1.6.1. Born Approximation	50
1.7. Photo Induced Aggregation	51
1.8. Statement of Task	57
CHAPTER 2: QUANTIFICATION OF RESOLUTION OF SLABS WITH EMBEDDED MICROSPHERES FOR IMAGING DIELEC- TRIC NANOSPHERES	58
2.1. Introduction	58

	viii
2.2. Fabrication of Slabs	61
2.3. Justification of use of nanospheres	65
2.4. Quantification of Resolution	67
2.5. Conclusions	70
CHAPTER 3: QUANTIFICATION OF RESOLUTION OF SLABS WITH EMBEDDED MICROSPHERES FOR IMAGING BIOMED- ICAL OBJECTS	72
3.1. Introduction	72
3.2. F-Actin Fabrication	74
3.3. Experimental Results	75
3.4. Conclusions	77
CHAPTER 4: ENHANCEMENT OF MID-WAVE IR FOCAL PLANE ARRAY BY INTEGRATION WITH DIELECTRIC MICROSPHERE- AND MICROCONE-ARRAYS	81
4.1. Introduction	81
4.2. Assembly of Microspherical Arrays	83
4.3. Enhancement by Microcone Arrays	90
4.4. Conclusions	100
CHAPTER 5: OBSERVATION OF PHOTOINDUCED AGGREGA- TION OF PLASMONIC NANOPARTICLES IN A SOLUTION	102
5.1. Introduction	102
5.2. Previous work performed at MIT Lincoln Lab	105
5.3. Experimental Results	110
5.3.1. Size Dependence	110
5.3.2. Frequency Dependence	114

	ix
5.3.3. Intensity Dependence	115
5.4. Conclusion	115
CHAPTER 6: INVESTIGATION OF LIGHT SCATTERING BY DIELECTRIC MICROSPHERES AIMED AT APPLICATION OF INVERSE SCATTING ALGORITHMS	119
6.1. Introduction	119
6.2. Experimental Set Up and Results	122
6.3. Simulation Results	125
6.4. Conclusion	128
CHAPTER 7: CONCLUSIONS AND FUTURE WORK	130
REFERENCES	133

LIST OF FIGURES

FIGURE 1: Photonic nanojets for different refractive indices.	8
FIGURE 2: Backscattering Enhancement.	10
FIGURE 3: 3D Photonic Nanojet.	12
FIGURE 4: 3D Backscattering Enhancement.	13
FIGURE 5: Photonic nanojet distance.	14
FIGURE 6: Microwave Jet.	16
FIGURE 7: Nanojet created by Latex microsphere.	17
FIGURE 8: Plasmon.	19
FIGURE 9: Nanosphere lithography.	24
FIGURE 10: Spectroscopic measurement techniques.	25
FIGURE 11: LSPR shift.	27
FIGURE 12: NSOM.	33
FIGURE 13: Perfect lens.	34
FIGURE 14: Superlens, Far-Field Superlens, Hyperlens.	35
FIGURE 15: Fiber induced evanescent fields for super resolution.	36
FIGURE 16: SiO_2 Microsphere super resolution.	37
FIGURE 17: Conventional-, Confocal-, Microspherical- Microscopy.	39
FIGURE 18: FPA history.	41
FIGURE 19: SWaP of HgCdTe detectors.	42
FIGURE 20: Detector and Optics limit.	43
FIGURE 21: HgCdTe photodiode.	45

FIGURE 22: InSb detector.	46
FIGURE 23: nBn detector.	46
FIGURE 24: Microbolometer.	47
FIGURE 25: Microlens array.	48
FIGURE 26: Scattering efficiency.	51
FIGURE 27: Coffee Ring Effect.	52
FIGURE 28: Evaporation of spheres and ellipsoids.	53
FIGURE 29: Confocal imaging of spheres and ellipsoids.	54
FIGURE 30: Marangoni Effect.	55
FIGURE 31: Photophoetic forces.	56
FIGURE 32: Optical trapping.	56
FIGURE 33: Virtual image.	62
FIGURE 34: Microsphere Embedded Elastomer Slab.	62
FIGURE 35: Embedding Microspheres.	65
FIGURE 36: End product.	66
FIGURE 37: Deposition of nanosphere.	67
FIGURE 38: Cross section of nanoplasmonic structure.	68
FIGURE 39: Nanosphere resolution results.	69
FIGURE 40: Conventional Microscopy vs Microsphere Assisted Microscopy.	74
FIGURE 41: Three configuration of microscopy.	75
FIGURE 42: Olympus IX71 40x objective resolution.	77
FIGURE 43: Olympus SD-OSR 60x objective resolution.	78

FIGURE 44: Deltavision OMX SR 60x objective resolution.	79
FIGURE 45: Suction array schematic.	84
FIGURE 46: Mechanical drilling results.	85
FIGURE 47: Etching results.	86
FIGURE 48: Etching results.	87
FIGURE 49: Microsphere and Micropillar.	89
FIGURE 50: Microsphere vs Microcone.	92
FIGURE 51: Normal incidence differ pixel size.	94
FIGURE 52: Normal incidence different pillar heights.	95
FIGURE 53: Electric field maps of different pillar heights at normal incidence.	96
FIGURE 54: Angular dependence on different mesa sizes.	97
FIGURE 55: Electric field maps at an angle which is half maximum of enhancement factor for different mesa sizes.	98
FIGURE 56: Angular dependence of different pillar heights.	99
FIGURE 57: Electric field maps of angular dependence of different pillar heights.	100
FIGURE 58: Transmission and enhancement of nanoparticles.	108
FIGURE 59: Nanoparticle clusters.	109
FIGURE 60: Experimental schematic of nanoparticle aggregation.	112
FIGURE 61: Experimental Result showing aggregation in the form of a letter A.	113
FIGURE 62: Frequency dependence for aggregating.	114
FIGURE 63: Experimental results showing intensity dependence of Au nanoparticles.	116

FIGURE 64: Inverse scattering experimental set up.	123
FIGURE 65: Schematic of inverse scattering experimental set up.	124
FIGURE 66: Inverse scattering images of different narrow band filters.	126
FIGURE 67: Experimental, collaborative simulation, and numerical results.	127
FIGURE 68: Inverse scattering comparison.	127

LIST OF TABLES

TABLE 1: Different super-resolution microscopy techniques.	31
--	----

CHAPTER 1: INTRODUCTION

1.1 Outline and Overview of this Dissertation

In this dissertation we investigate optical waves interacting with dielectric spheres. The bulk of this work will focus on optical waves interacting with dielectric spheres. The spheres of interest will vary in size, diameter of the sphere d_{sphere} ; from spheres that are much larger to spheres that are much smaller than the wavelength of light, λ , the object is interacting with. The spheres that are much larger is said to be in the geometrical optics regime, $d_{sphere} \gg \lambda$. The spheres that are comparable to the wavelength is said to be in the Mie regime, $d_{sphere} \approx \lambda$. The spheres that are much smaller is said to be in the Rayleigh regime, $d_{sphere} \ll \lambda$. All three have different considerations that must be taken into account when working in the respective regimes.

These spheres, mainly those in the Mie regime, are of great interest due to their ability to manifest photonic states [153, 203, 141, 176, 136, 115, 81, 188, 23, 45, 193, 15, 217, 107, 219, 221, 17, 174, 116, 117, 213, 212, 165, 79, 154, 171]. The photonic states can produce some interesting optical effects. These effects are seen in enhanced imaging capabilities [220, 94, 52, 65, 32, 158, 140, 145, 232, 227, 147, 111, 150, 200, 50, 225, 231, 146, 230, 9, 24, 38, 39, 27] , highly concentrated optical beams [29, 124, 12, 8, 43, 151, 102, 144, 118, 44, 70, 59, 58, 138, 139, 75, 74, 61, 128, 129,

161, 177, 77, 76, 37, 78, 84, 133, 96, 119, 175, 160, 30, 233, 143, 144, 70], and finally the scattering information has unique characteristics.

Chapter 2 and Chapter 3 will focus on the enhanced imaging capabilities whereas Chapter 4 will focus on the highly concentrated optical beams ultimately diverting to the creation of similar effects of concentration of optical beams using shapes other than spheres. We will push the limits of this highly concentrated optical beam in Chapter 5 of by attempting to aggregate nanoparticles using microspheres in a solution.

Chapter 6 will be investigating the scattering effects of dielectric microspheres which are in the Mie regime. Relating the scattered pattern generated to generate information about the object that created the pattern.

Due to the fact the technology of fabrication of microspheres is different from that in standard semiconductor structures and due to intrinsically high surface quality for many such fabrication technologies, the whole area of fabrication, photonic engineering and application of such structures formed by spherical building blocks can be viewed as a special division within the modern photonics. In previous works of the Prof. Vasily N. Astratov's Mesophotonics laboratory a terminology of, "microspherical photonics," was introduced to reflect the special properties of such structures formed by microspheres. The main properties representing such microspherical photonics are the fact that the minimization of the surface energy tend to favor perfect spherical shape of microspheres. This is apparent for microspheres obtained in a form of liquid droplets by laser-induced melting fiber, such microspheres can acquire a perfect spherical shape under the influence of surface tension forces in the process of their free falling motion and solidification before they landed on a substrate [216]. To some ex-

tent similar tendencies favoring the perfect spherical shape are common for many fabrication technologies. Another property characterizing such microspherical photonics is represented by the size uniformity of such spherical micro resonators. Internal resonances in microspheres, so-called whispering-gallery modes, can be coupled very efficiently if these resonances spectrally overlapped in different microspheres. In principle, such microspherical building blocks with extraordinary uniform resonant properties can be selected or sorted by different methods and such sorted microspheres can be used for building coupled-cavity structures and devices with engineered photonic dispersions. In this regard, microspherical photonics allows manipulation with and sorting of individual spheres which is not possible for other micro resonators such as micro disks or micro rings fabricated on the same chip. Such properties allow to speak about microspheres as, "photonic atoms," and about clusters of microspheres as, "photonic molecules." Another feature of microspherical photonics is related to a broad range of applications of structures and devices built from microspherical building blocks. The work performed previously by the Mesophotonics laboratory at University of North Carolina Charlotte was devoted to applications of microspherical photonics as well as to fundamental understanding of near-field aspects of optical coupling and imaging in microspheres and other similar structures such as various micro resonators with circular symmetry and microcones. Roughly it can be divided into the following areas: a) super-resolution imaging by microspheres and microfibers [173, 13, 172, 10, 11, 50, 52] b) infrared photodetectors and focal plane arrays [3, 6], inverse scattering [134], resonant optical forces which can be used for sorting microspheres [153, 171, 170, 154], optical scalpels [114, 113, 49], and photonic nanojets and whispering gallery modes

[152, 168, 7, 51, 48, 212, 122, 229, 228, 107, 26, 22, 124, 18, 123, 57, 21].

In this Ph.D. thesis work, we concentrate on properties of structures and devices based on microspheres (and in some applications on microcones) which use rather focusing, imaging, and scattering capabilities of microspheres and to less extent their resonant properties. The aspects which are important for this thesis work are an ability of contact spherical microlenses to catch the object's optical near-fields as well as an ability of spherical microlens to create tightly focused beam termed, "photonic nanojet." [151] These aspects are characterized with some involvement of near-field optics and evanescent fields. In this regard, the description of electromagnetic fields in the wavelength-scale proximity to the spherical interface can have special features in comparison with well-known far field solutions usually obtained using approximations of geometrical optics. We consider different optical properties of such microscale objects, not only imaging and focusing. An example of this is represented by scattering of light by high-index microspheres which can be used as a model system for testing inverse scattering algorithms. One more subject included in this thesis work goes beyond the microspherical photonics and is related to photo induced aggregation of nanoplasmonic particles in a solution.

Chapter 1 is a literature review on relevant material existing in imaging, solution evaporation, and inverse scattering problems. There is no way of making this into a list that will only relate to a single chapter as nearly all following chapters are interconnected in some way having multiple explanations for the phenomena of interest described in each chapter.

In Chapter 2, we will use high index microspheres embedded in rigid elastomer

slabs for quantifying the resolution of dye doped dielectric nanospheres. This is a well-known super resolution imaging technique which has provided lateral resolutions of $\sim \lambda/7$ in nanoplasmonic dimer arrays. This is compared to the theoretical limit of $\sim \lambda/4$, which comes from Abbe's limit. In this chapter we will address the question about how to increase the resolution of objects which do not possess nanoplasmonic resonant properties themselves. The main technique considered in this chapter is based on using nanoplasmonic arrays for structured illumination of such objects. This chapter will begin with the fabrication of the slabs, give some justification as to why we chose the nanospheres as an object, move on to the quantification process of resolution of the nanospheres, and finish with connections to work done in Chapter 3 using F-Actin proteins as an object.

In Chapter 3, we are expanding on the results from Chapter 2. We explore a different object and quantify the resolution of an optical system using a contact microsphere embedded in the rigid elastomer slab described in Chapter 2. It must be stated that this is the first work in which a biological object is used to quantify the resolution of the optical system using a contact microsphere. This chapter will begin with the fabrication of the F-Actin proteins, move to the experimental results, and finish with the conclusions of this original work.

In Chapter 4, we will focus on enhancing the photocurrent of photodetectors by coupling arrays of dielectric microsphere- and microcone-arrays. This chapter will begin with work attempting to assemble microspherical arrays for enhancing an entire sensor, move onto enhancement by microcone arrays by simulations along with first attempts to fabricate these microcone arrays, we will then make conclusions on this

work.

In Chapter 5, we will be reporting some initial results which came about in attempting to have a reversible process to aggregate plasmonic nanoparticles in a solution. We will look at results focusing on frequency of illumination and the concentration of illumination for creating this aggregation. We will conclude with future work that needs to be done on this in order to have a more complete understanding of the phenomena.

In Chapter 6, we will be investigating the light scattering properties of high index dielectric microspheres. These microspheres create a scattered pattern which is then used for reconstruction of the shape and refractive index which created it. The reconstruction will ideally state what the object is in three dimensions using inverse scattering techniques. We focus on the experimental aspect of this application. Focusing on the experimental set up and results and why they are important in the optical regime of the electromagnetic spectrum.

In Chapter 7, we draw conclusions and propose future work that would expand upon the content of this dissertation.

1.2 Photonic Nanojet

Since 2004, a substantial amount of literature [124, 43, 151, 102, 118, 44, 70, 160, 30, 233, 143, 144, 70] has developed regarding the existence, properties, and potential applications of the photonic nanojet. These photonic nanojets have some key properties which include: (1) it is a non-evanescent, propagating beam that can maintain a subwavelength waist full-width half-maximum (FWHM) transverse beam

width along a path that can extend more than $\sim 2\lambda$ beyond the dielectric cylinder or sphere. (2) It has a minimum FWHM beam waist that can be smaller than the classical diffraction limit, in fact it can be as small as $\lambda/3$ when using microspheres. (3) It is a non-resonant phenomenon that can appear for a wide range of diameters of the dielectric micro cylinder or microsphere from $\sim 2\lambda$ to more than 40λ if the refractive index contrast relative to the background medium is less than 2:1. (4) It has a high intensity that can significantly exceed that of the illuminating wave. Finally, (5) inserting a nanoparticle, d_n , within the nanojet the nanoparticle perturbs the far-field backscattered power of the illuminated microsphere by an amount that varies as d_n^3 for a given wavelength. This perturbation is much slower than the Rayleigh scattering dependence which follows d_n^6 for the same isolated nanoparticle. This leads to a situation where the nanojet serves to project the presence of a nanoparticle to the far field. For example for a $3\ \mu\text{m}$ microsphere backscattering could double from a $30\ \text{nm}$ nanoparticles being inserted into the nanojet, despite the nanoparticle having only $1/10,000$ the cross section.

These properties show potentially an important aspect of the applications of photonic nanojets for detecting and manipulating nanoscale objects, sub diffraction resolution nanopatterning and nanolithography, low-loss waveguide, and ultrahigh-density optical storage.

The initial work on photonic nanojet was done and reported by Chen et al [43]. They are the ones that coined the term, "photonic nanojet," even though the idea of highly concentrated electromagnetic radiation was of interest in microsphere dry laser cleaning [166, 167, 238] and periodical patterning [112] years before the coining

of this term. Even with this, the photonic nanojet concept was rigorously researched using high-resolution finite-difference time-domain (FDTD) computational solutions of Maxwell's equations [215]. This FDTD simulation used a plane-wave illuminations propagating onto a micro-scale, circular dielectric cylinder which generated a narrow, high-intensity, sub-diffraction beam waist that propagates into the background medium from the shadow side of the cylinder.

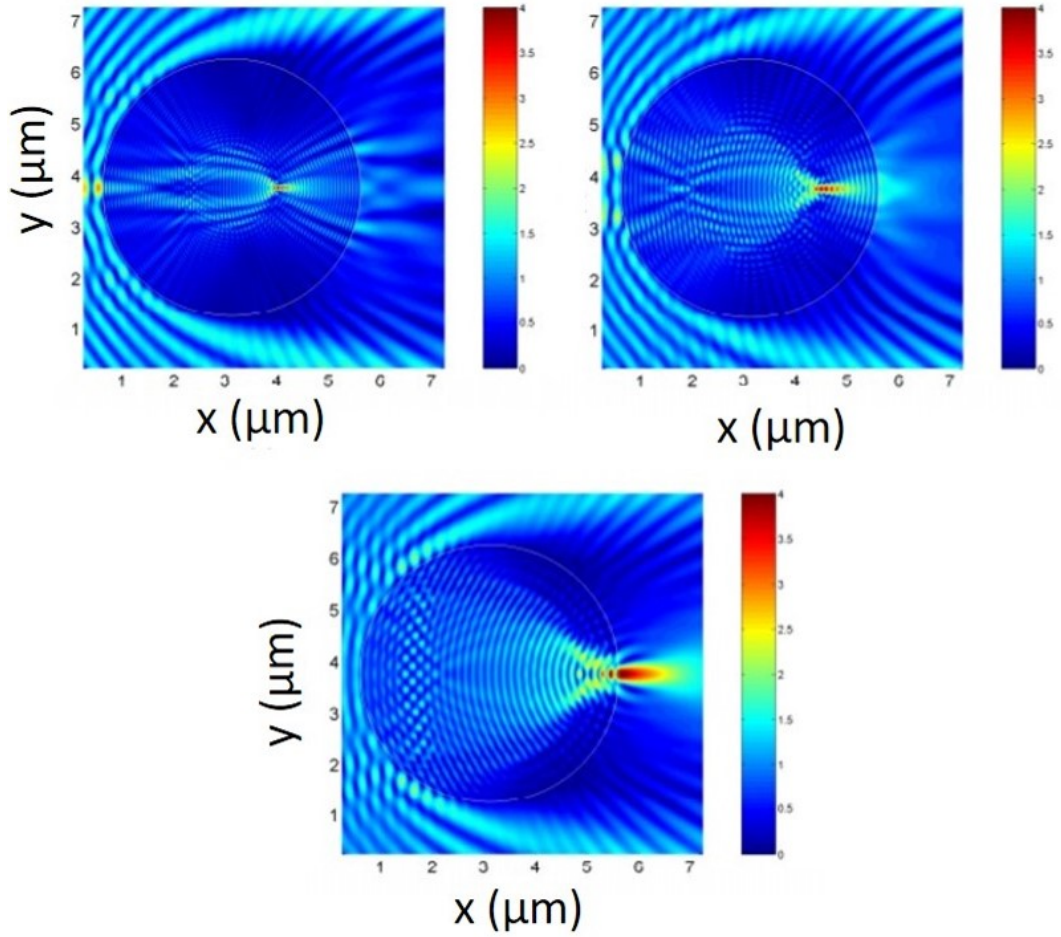


Figure 1: Visualizations of the evolution of a photonic nanojet as the refractive index of a dielectric cylinder decreases. The FDTD computed envelope of the electric field of a propagating plane wave interacting with a $d = 5$ micron diameter cylinder of uniform refractive index. (a) $n=3.5$ with a photonic nanojet inside of the sphere (b) $n = 2.5$ with a photonic nanojet inside of the sphere and (c) $n = 1.7$ with a photonic nanojet outside of the sphere [43].

Chen et al's work first reviewed the validity of its FDTD computational technique, which employed a uniform square cell size of 1.25 nm and the perfectly matched layer absorbing outer grid boundary condition [43]. This was compared using several different scattering cross sections including homogeneous, isotropic, circular dielectric cylinders with the exact series solution. It was found to be within 1 dB over entire range of scattering angles for all cases.

Reference [43] reported detailed two-dimensional computational studies of the internal and near-external fields of a series of homogeneous, isotropic, lossless, infinitely long, circular dielectric cylinders. Each cylinder was assumed to be illuminated by a plane wave polarized with the incident electric field parallel to the cylinders infinite axis. Photonic nanojets creation depends greatly on the refractive index of the circular dielectric cylinder, it can be seen that Chen et al shows the focusing of the dielectric cylinder is inside of the cylinder for refractive indices greater than 2 and are outside of the cylinder when the refractive index reaches $n_{cylinder}=1.7$, see Figure 1. In these simulations a circular cylinder of uniform refractive index and diameter of 5 μm embedded within an infinite vacuum with refractive index $n=1.0$ was simulated. A wavelength of $\lambda=500$ nm propagating from left to right into the micro cylinder, see Figure 1. It was not until the refractive index of the micro cylinder was below $n=2.0$ a photonic nanojet emerged from the shadow side of the object, see Figure 1 (c). This emerging photonic nanojets have a length between 800 nm to 1000 nm ($1.60\lambda-2.00\lambda$) with a FWHM intensity waist of 200 nm to 240 nm ($0.40\lambda -0.48\lambda$).

The final thing that Reference [43] stated was the impact of positioning a nanometer-scale object into the nanojet generated by the dielectric cylinder on the

backscattering of the nanometer-scale object. They showed that the use of different nanometer sized objects give a different backscattering enhancement between being inside of the nanojet and being isolated. They simulated this using a cylinder with diameter $6 \mu\text{m}$ with an index of refraction of $n_{cylinder}=2.3275$ surrounded by an index $n_{surrounding}=1.33$ illuminated with electromagnetic radiation of $\lambda=300 \text{ nm}$. They then placed a square dielectric nanoparticle of index 1.5 at the center of the nanojet generated by the $6 \mu\text{m}$ micro cylinder and the results are shown in Figure 2.

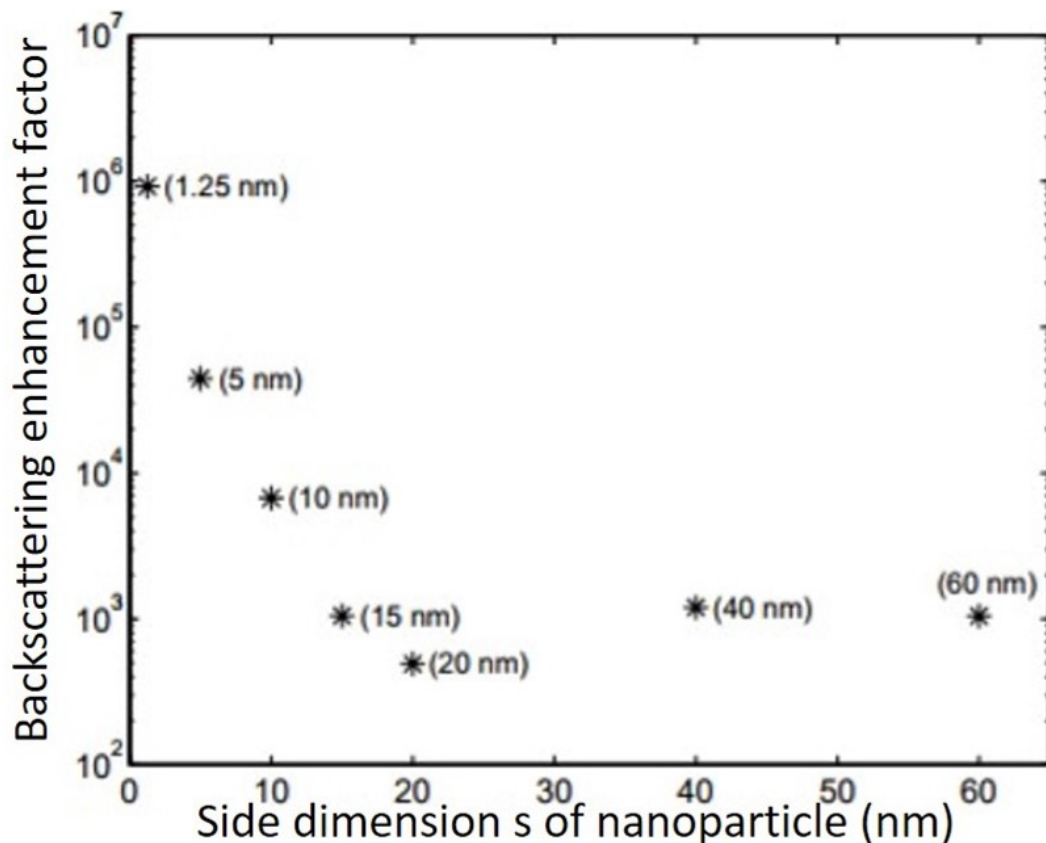


Figure 2: FDTD numerical results illustrating backscattering enhancement factor as a function of nanoparticle size behind a microcylinder of 6 microns. [51]

The initial identification of photonic nanojets for a dielectric sphere and not cylinder was reported by Li et al [151]. Their calculations implemented an exact eigen function series solution of Maxwells equations in spherical coordinates, to compute the

near field external to each plane-wave illuminated dielectric sphere of interest. It was shown that a plane-wave illuminated, micron-scale dielectric sphere can generate a fully three-dimensional photonic nanojet which has a sub-diffraction minimum beam width. These nanojets have similar properties to the nanojets generated by the cylinders; however, the nanojet generated by the dielectric sphere has an even higher intensity than the nanojet generated by the dielectric cylinder. Not only is this but the backscattered power of the dielectric sphere perturbed by a nanometer-scale particle is even greater than that of the dielectric cylinder.

These simulations first studied a series of homogenous, isotropic, dielectric microspheres of index of refraction $n_{sphere}=1.59$. Each sphere was illuminated by an x-polarized, z-propagating plane wave with wavelength $\lambda=400$ nm. They found that the FWHM of the created photonic nanojet increases as the size of the microsphere increases. The intensity of the photonic nanojet also increases as the size the microsphere increases. The FWHM of the generated photonic nanojet ranged from 130 nm to 210 nm (0.325λ - 0.525λ), see Figure 3.

A study was also done on the backscattered enhancement of a gold nanoparticle placed in the center of the photonic nanojet, this showed a vast increase to the enhancement factor over the enhancement of the cylinder backscattered enhancement factor, see Figure 4. This enhancement factor was computed using a generalized multiparticle Mie technique, which provides a rigorous analytical solution for electromagnetic wave scattering by multiple spheres based on vector spherical wave functions. The enhancement factor ranges from 3×10^4 to 2×10^8 as the size goes from 60 nm to 2 nm respectively. This represents a 30-fold to 200-fold enhancement over the cylinder

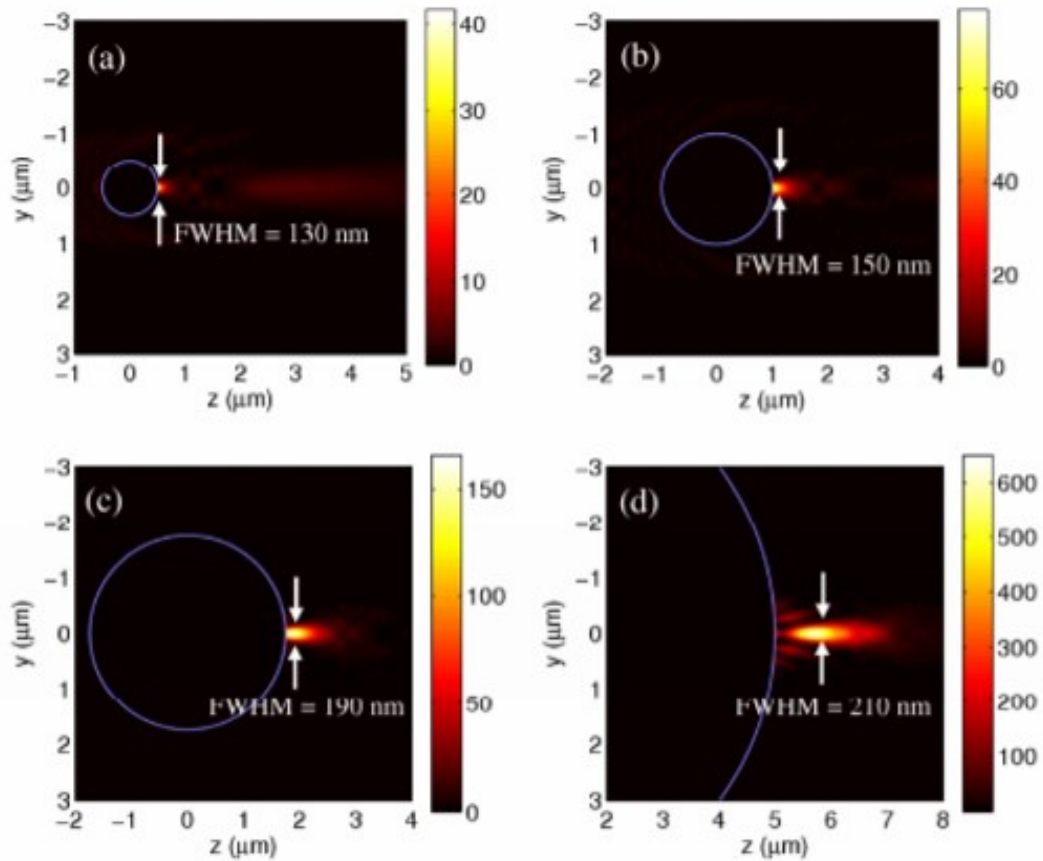


Figure 3: Photonic nanojets generated by illuminating dielectric spheres ($n=1.59$) with $\lambda=400\text{nm}$ of different sphere diameters D ; (a) $D=1$ micron (b) $D=2$ micron (c) $D=3.5$ micron (d) $D=8$ micron [151]

alone.

Further work was mathematically done by, Lecler et al [144]. Lecler applied Mie theory to analyze the general three-dimensional vectorial properties of the photonic nanojets generated by a plane-wave illuminating a dielectric microsphere in free space. It is this that reports that nanojets can be generated for a wide range of microsphere diameters, $\sim 2\lambda$ to greater than 40λ . They reported the sub-wavelength waist of the nanojet is a consequence of the proximity of the microsphere's shadow-side surface and its focus point in the exterior region of the microsphere, i.e. the microsphere

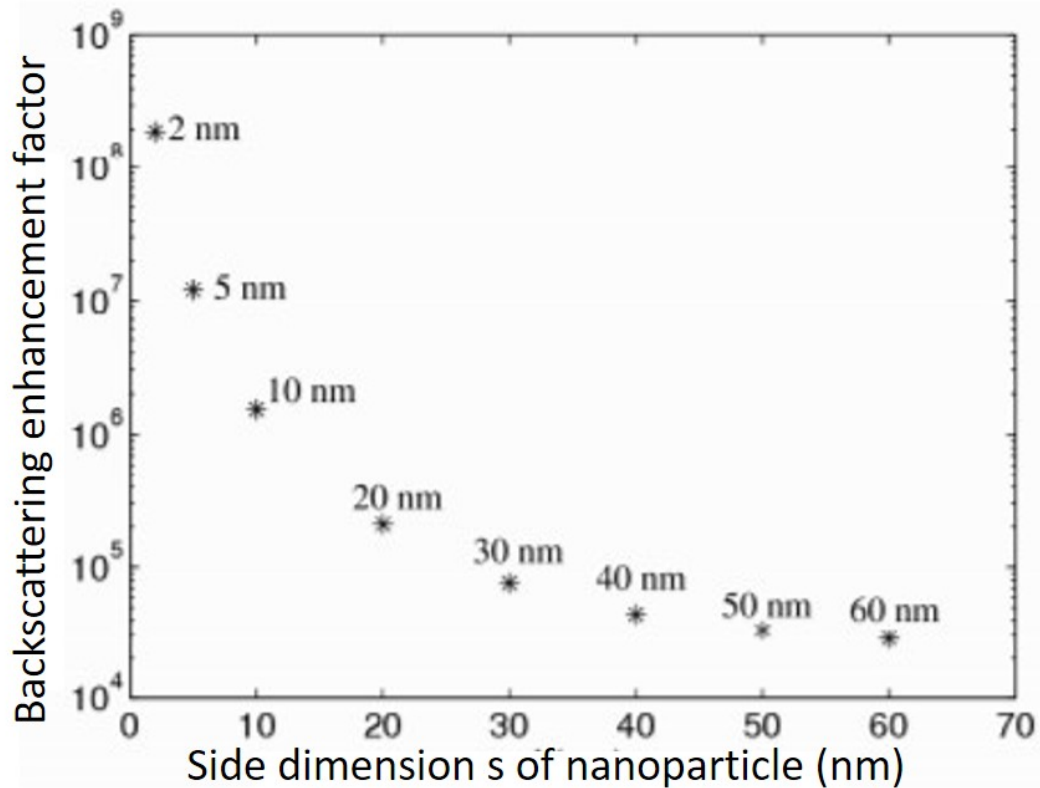


Figure 4: The backscattering enhancement factor for a gold nanoparticle of different size placed in the photonic nanojet generated from a microsphere with diameter $D=3.5$ micron, refractive index $n=1.5$ illuminated with a plane wave of $\lambda=400$ nm.[151]

is a microlens. They show that the distance where the FWHM stays smaller than the wavelength and the intensity is above half-maximum depends on the size and refractive index of the sphere, see Figure 5.

Other work done by Itagi and Challener [118] provided a detailed analysis of the optics of photonic nanojets in two dimensions for the case of a plane-wave illuminating an infinitely long dielectric cylinder. They began using eigen function solutions of the Helmholtz equation which was recast into a Debye series. The first term is of particular interest as it connects the physical and geometrical optical properties of the nanojet and allows for field analysis. Overall they concluded that, "jetting of the

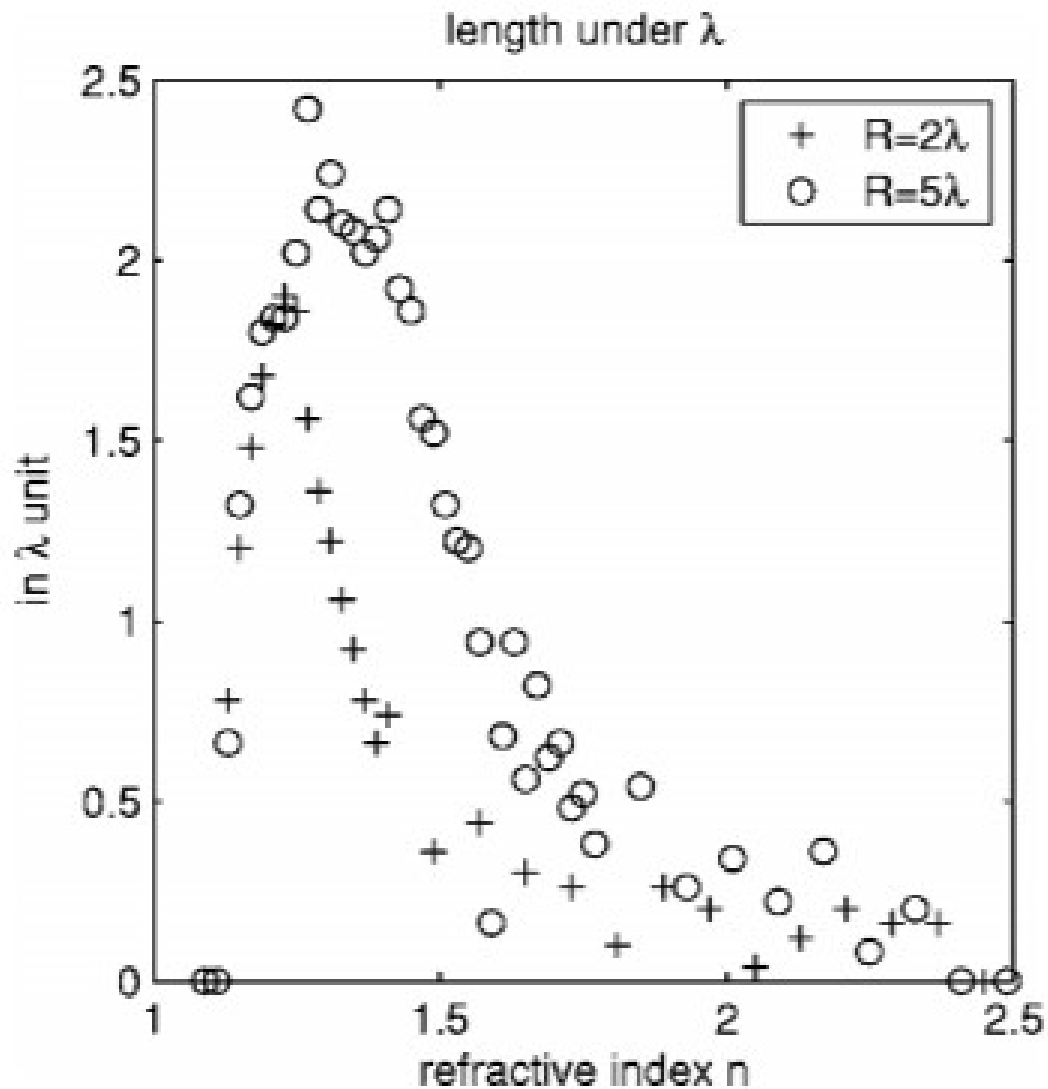


Figure 5: Distance along propagating direction where the FWHM stays smaller than the wavelength and the intensity is greater than half-maximum for spheres of radius 2λ and 5λ . [144]

nanoscopic optical spot over many wavelengths is a result of a unique combination of features in the angular spectrum, a peak in the angular spectrum at $s=\pm 1$, the finite content of propagating spatial frequencies, a small but finite content of evanescent spatial frequencies, and, most importantly, a peculiar distribution of the phase."

Further investigations were completed by Devilez et al [59] whom studied the

spatial and spectral properties of the three-dimensional photonic nanojet and quantitatively evaluated the contributions from all spatial frequency components, both propagating and evanescent. They do this study using both Gaussian illumination along with plane-wave illumination and focus most of their studies using Mie theory. They conclude that a decomposition of propagative and evanescent frequencies is dominated by the propagative with the evanescent field to play an important role in enhancing and sharpening the photonic nanojet distribution.

The first reported photonic jet created in an experimental setting came from Heifetz et al [102]. They used a 7.62 cm diameter acrylic sphere with a metal sphere placed in the photonic nanojet generated by illuminating the sphere is a $\lambda=1$ cm wave. They measured the backscattering perturbation caused by a 1 mm metal particle, see Figure 6. This is evidence that the generation of the jet is possible but it was in the microwave regime and not necessarily a photonic nanojet.

It was not until Ferrand et al [70] until a true photonic nanojet was formed at optical wavelengths. This was finally visualized by using a 5 μm latex microsphere with refractive index $n_{\text{sphere}} \approx 1.6$, see Figure 7 (a). Further investigation went to measuring the intensity of this electromagnetic radiation through the photonic nanojet generated, see Figure 7 (b,c). Finally they measured the FWHM was measured as a distance dependence from the microsphere, see Figure 7 (d).

Kapitonov and Astratov [124] have reported the use of photonic nanojets for low-loss optical waveguides. Yi et al [233] has reported an experimental observation of enhanced Raman scattering by self-assembled silica microspheres. Lecler et al [143] has reported an experimental observation of the nonlinear enhancement of two-photon

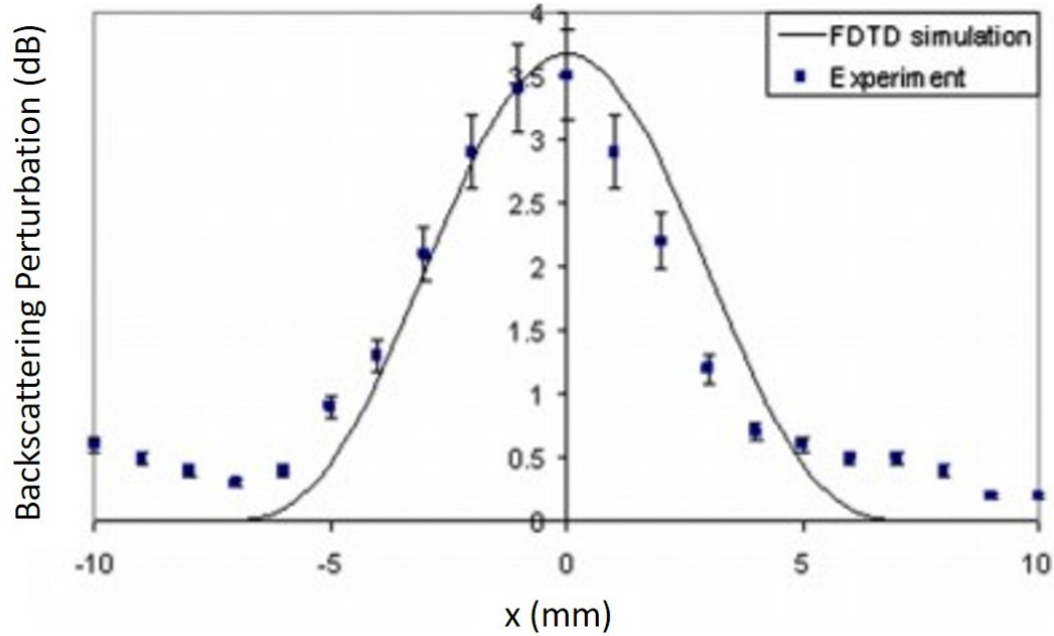


Figure 6: Measured and FDTD-calculated backscattering perturbation caused by a 1 mm metal particle scanned laterally across a microwave jet.

excited fluorescence from a molecular dye solution brought about by adding drops of a suspensions of silica microspheres. Wu et al [103] has reported an experimental demonstration of a mask-less subwavelength-resolution direct-write nanopatterning technique which uses a self-assembled planar array of transparent silica or polystyrene microspheres deposited on top of a photoresist in a single layer. Gerlach et al [79] has reported optical measurements of small symmetrical arrays of contacting latex microspheres for directional emission, this motivated the usage of the term, *“photonic molecule.”* Chen et al. [42] has patented means to perform optical metrology of semi conductive wafers using photonic nanojets. Cui et al [47] have started work for optically trapping nanoparticles within a photonic nanojet. Kong et al [137] have computationally and experimentally investigated the potential application of the use of photonic nanojets to implement ultrahigh density optical data-storage.

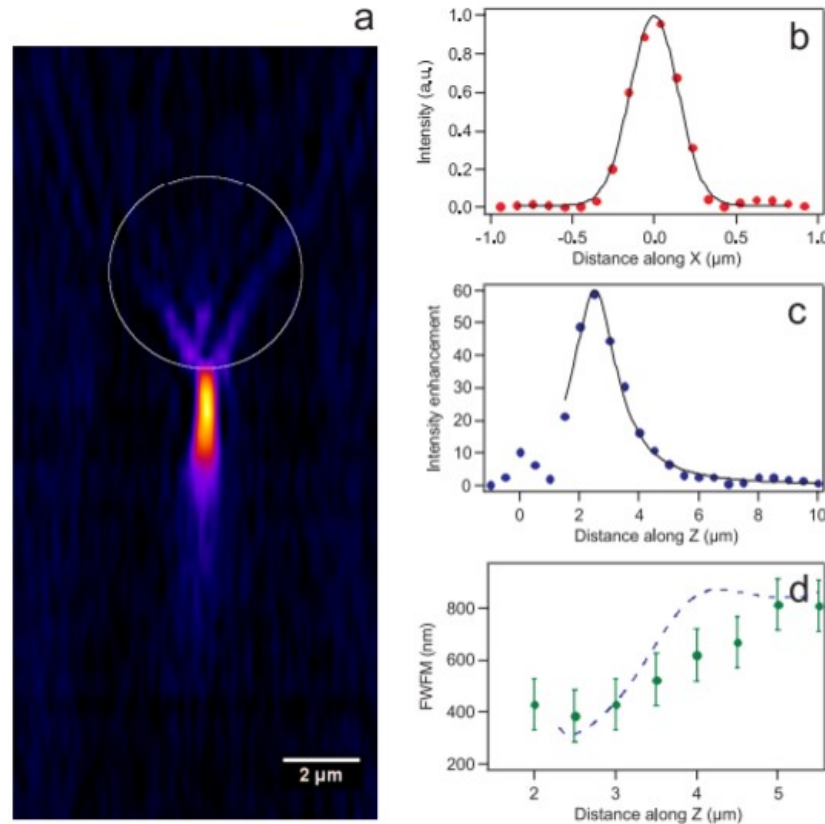


Figure 7: (a) Visualization of the experimentally measured photonic nanojet generated by a 5 micron latex microsphere (refractive index $n_{sphere} = 1.6$) on a glass coverslip. The illumination is a downward propagating plane wave with $\lambda = 520$ nm (b) measured intensity normalized to the peak value of unity along a horizontal line cutting through the narrowest waist of the nanojet. (c) Measured intensity normalized to the incident wave along the vertical line below the microsphere at the center of the nanojet. (d) FWHM beamwidth of the nanojet versus distance below the microsphere. [70]

1.3 Localized Surface Plasmon Resonance (LSPR)

The idea of surface plasmon resonance (SPR) and materials that can support them are an important aspect of this dissertation work, Figure 8 (a). The generation of SPR require a material with a negative real and small positive imaginary dielectric constant. This allows for a resonance of coherent oscillations of the surface conduction electrons excited by electromagnetic (EM) radiation. Plasmonics is the study of

this light matter interaction which has a vast array of applications, surface-enhanced spectroscopies [120, 100, 202, 234, 237, 186, 135, 82], biological and chemical sensing [87, 68, 191], and lithographic fabrication [208, 127, 211]. Using controlled fabrication and manipulation of metallic structures on the nanoscale level, researchers have demonstrated new applications that take advantage of the localized surface plasmon resonance (LSPR). These LSPR do not propagate, see Figure 8 (b), but instead oscillate about the particle of interest.

For surface plasmon polaritons, plasmons propagate in the x- and y- directions, along the direction of the metallic film for several hundred microns and decays evanescently in the z-direction, into the dielectric media. The interaction of this interface leads to a plasmon resonance shift which can be observed in three methods: (1) angle resolved, (2) wavelength shift, and (3) imaging [208]. For the first 2 modalities measurements are typically taken by taking reflectivity measurements at either constant wavelength or constant angle respectively. The third maps the reflectivity of a surface with constant wavelength and angle.

For localized surface plasmons, the size of the particles that are interacting with light is much smaller with a large separation between them. This leads to a plasmon that oscillates locally around the nanoparticle with a frequency known as the LSPR [88, 126]. LSPR decay evanescently in all directions, theoretically, meaning that there are no polaritons involved. But similar to SPR LSPR are sensitive to changes in the local dielectric environment [181, 126, 121] and can use these for sensing wavelength-shifts along with angle-resolved sensing [92]. Typical measurements for LSPR are wavelength dependent with very few angle sensing applications being found.

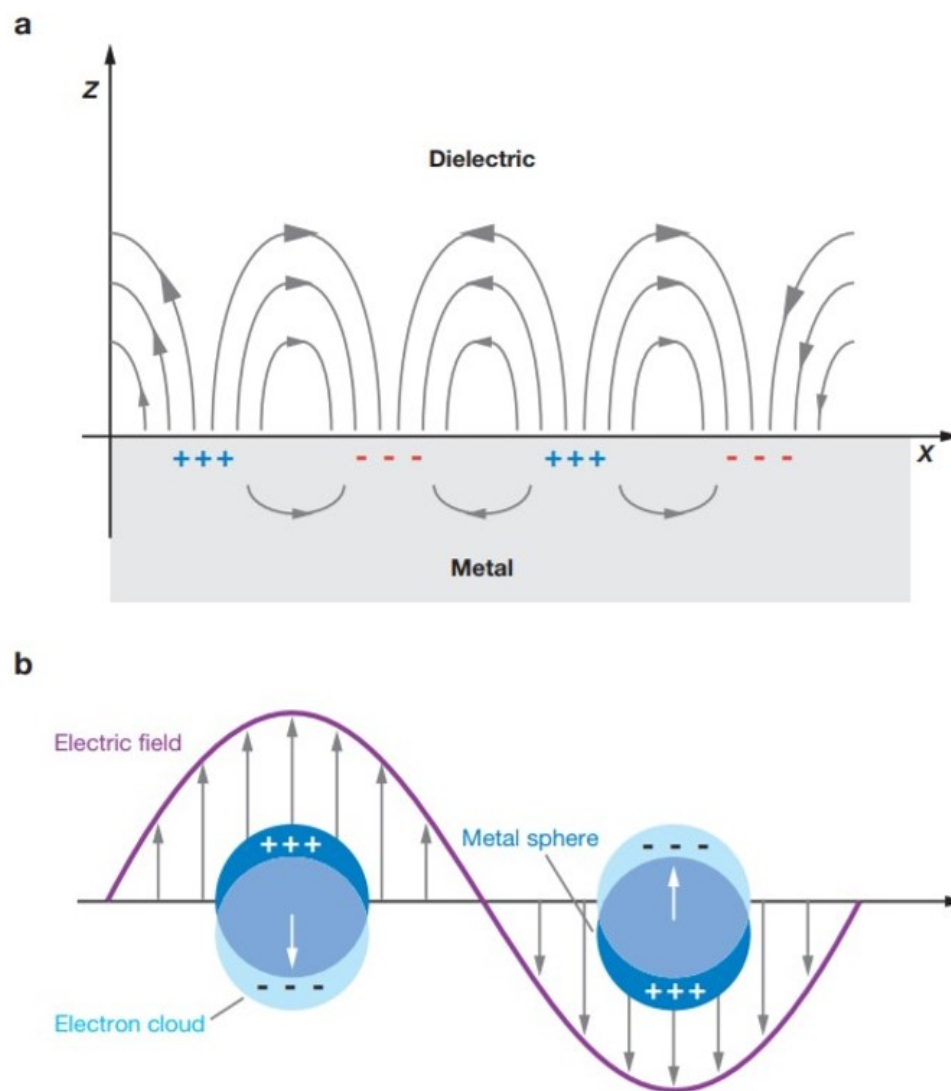


Figure 8: Schematic diagram illustrating (a) surface plasmon polariton and (b) localized surface plasmon.[222]

Investigations and understandings of both propagating and localized surface plasmons developed the discovery of surface-enhanced Raman scattering (SERS) [5]. Due to the complex nature of the metallic surface and the coupling of the incident radiation to the metallic surface a tremendous amount of theoretical and experimental effort has gone into understanding surface plasmons [237, 183, 98, 204]. A focus has been on how the size, shape, material, and local dielectric properties effect the surface

plasmons. It was discovered that all of these have a direct influence in determining the LSPR wavelength. Because of this plasmon spectroscopy enjoys a reputation as an ultrasensitive method for detecting molecules of both biological and chemical interest.

Currently SPR spectroscopy dominate commercial instrumentation; however, LSPR spectroscopy offers many of the same advantages for sensing along with several additional benefits [234, 89]. These benefits include the range and variability of the sensing applications. SPR sensing provides much high sensitivity for bulk changes in the refractive index over LSPR; however, LSPR rival if not surpass in single-nanoparticle sensing [204, 185]. Each different nanoparticle gives a different frequency shift for sensing; these parameters are determined by the shape, size, and material of the nanoparticles. They are also fairly robust being activate able by light from the visible to the infrared region of the electromagnetic spectrum.

Looking deeper into the theory of LSPR we should consider a single particle with radius a embedded in an external medium with dielectric constant ϵ_o and the sphere has dielectric constant ϵ_1 . We need to illuminate this particle with light, y-propagating and z polarized light.

$$E = E_x + E_y + E_z \tag{1}$$

Where E is the electric field, E_x is the electric field in the x direction, E_y is the electric field in the y direction, and E_z is the electric field in the z direction. The value of E_x , E_y , E_z are controlled by polarization, this forces E_x and E_y equal to zero

and E_z be equal to:

$$E_z = E_z^0 \cos\left[2\pi\left(\frac{x}{\lambda} - \nu t\right)\right] \quad (2)$$

Where E_z^0 is the initial electric field along the z direction, x is the location of interest along the x direction, λ is the wavelength of illumination, ν is the frequency of illumination, and t is the time.

It is possible to simplify (2) by substituting $2\pi/\lambda=k$ and $2\pi\nu=\omega$ and focusing on the physical meaning of the problem. By doing this Maxwell's Electrostatic equations are simplified due to the electric field being constant in time; the equations of interest become:

$$\nabla \cdot E = 0 \quad (3)$$

$$\nabla \times E = 0 \quad (4)$$

Where $\nabla \cdot E$ is the divergence of E and $\nabla \times E$ is the curl of E. Both of these must be zero to have physical meaning to the problem.

Converting from Cartesian coordinates to spherical coordinates a form of:

$$\nabla^2(r, \theta, \phi) = \frac{1}{r^2} \frac{\delta}{\delta r} \left(r^2 \frac{\delta}{\delta r} \right) + \frac{1}{r^2} \left[\frac{1}{\sin\theta} \frac{\delta}{\delta \theta} \left(\sin\theta \frac{\delta}{\delta \theta} \right) + \frac{1}{\sin^2\theta} \frac{\delta^2}{\delta \phi^2} \right] \quad (5)$$

With an assumption that the solution takes the form of:

$$\Phi(r, \theta, \phi) = F(r)Y(\theta, \phi) \quad (6)$$

With $F(r)$ being the radial component and $Y(\theta, \phi)$ being the polar and azimuthal components.

Going through separation of variables for radial, polar, and azimuthal angles:

$$G = \frac{r^2}{(F(r))} \left[\frac{\delta^2 F(r)}{\delta r} + \frac{2}{r} \frac{\delta F(r)}{\delta r} \right] \quad (7)$$

$$D = \left[\frac{\sin\theta}{P(\theta)} \frac{\delta}{\delta\theta} \left(\sin\theta \frac{\delta P(\theta)}{\delta\theta} \right) \right] + G \sin^2\theta \quad (8)$$

$$D = -\frac{1}{Q(\phi)} \frac{\delta^2 Q(\phi)}{\delta\phi^2} \quad (9)$$

After solving the radial, polar, and azimuthal equations combining them and applying boundary conditions:

$$E_{out}(x, y, z) \rightarrow E_{zo} \quad \text{as } r \rightarrow \infty \quad (10)$$

$$\varepsilon_{in} * E_r(in) = \varepsilon_{out} * E_r(out) \quad (11)$$

$$E_{in}(x, y, z) \rightarrow \text{finite} \quad \text{as } r \rightarrow 0 \quad (12)$$

$$E_\theta \quad \text{and} \quad E_\phi \quad \text{are continuous} \quad (13)$$

One ends up with

$$E_{out}(x, y, z) = E_0 z - \left[\frac{\varepsilon_{in} - \varepsilon_{out}}{\varepsilon_{in} + 2\varepsilon_{out}} \right] a^3 E_0 \left[\frac{z}{r^3} - \frac{3z}{r^5} (x + y + z) \right] \quad (14)$$

From this we now can easily see that when $\varepsilon_{in} \approx 2\varepsilon_{out}$ the EM field is enhanced relative to the incident field. This derivation is well known.

This is the basis towards knowing and understanding surface-enhanced Raman scattering (SERS). SERS is an interesting topic of study [222] as the enhancement factor is reliant on more than just the incident excite but also on the resulting Stokes shifted Raman fields.

There are two techniques in particular which we will discuss for fabricating these periodic arrays. These arrays can have a specific particle shape, placement, and orientation. These two methods are described below.

One technique in particular is nanospheres lithography (NSL) [98, 97, 112] which begins with a clean substrate, see Figure 9 (a-1), and deposits a solution of nanospheres onto the top face of this substrate, see Figure 9 (a-2). This solution is left to evaporate and forms a monolayer of nanospheres, see Figure 9 (a-3). After the nanospheres are completely dry metal is deposited normal to the substrate, see Figure 9 (a-4). Finally liftoff is done leaving a nanoplasmonic array on the substrate, see Figure 9 (a-5,b). Oftentimes it is desirable to check the deposition of the metallic layer, this can be done using atomic force microscopy (AFM) when the nanospheres are still attached to the substrate, before liftoff. The quality of this film can determine the quality of the final nanoplasmonic array, see Figure 9 (c).

Another technique, although more time-consuming and expensive, offers this

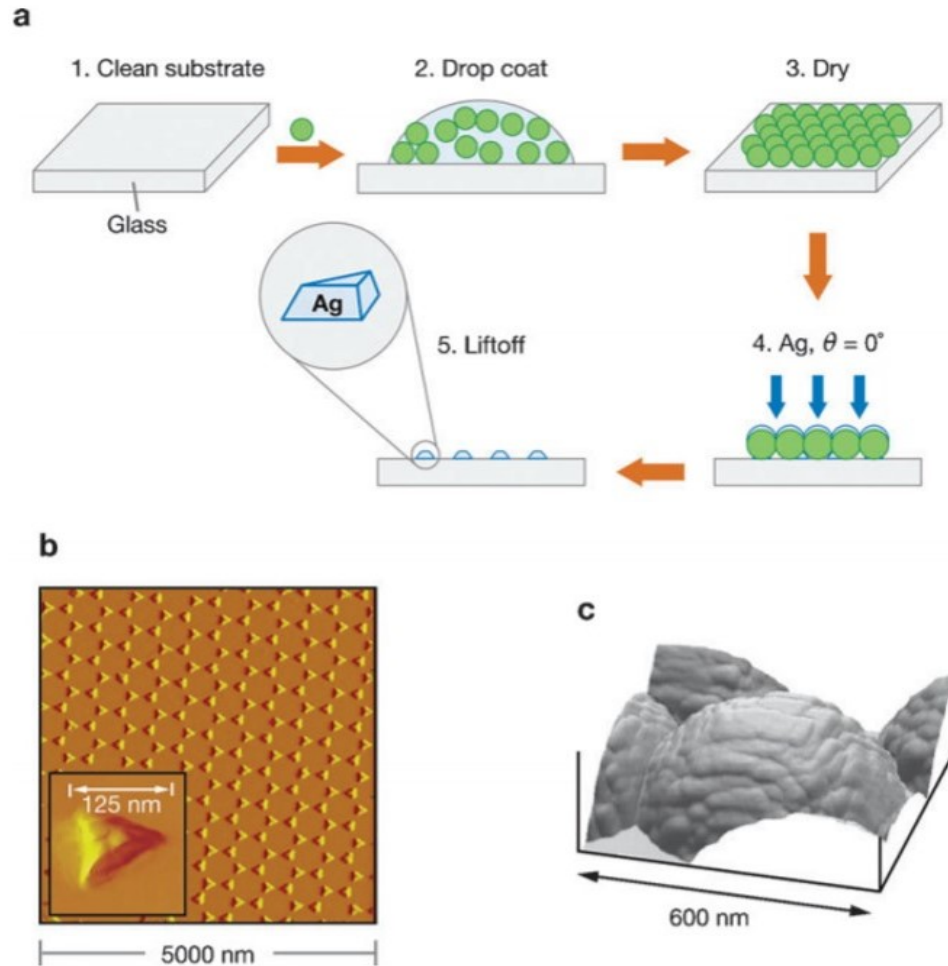


Figure 9: (a) Illustration of the process of nanosphere lithography showing self-assembly of nanospheres, to metal deposition, and finally lift off. (b) Atomic force microscopy (AFM) image of a nanoplasmonic substrate after lift off (c) AFM image of a film while nanospheres are still on the surface [222].

advantage of creating arbitrary size, shape, and space for a nanoplasmonic array being electron beam lithography. Many research groups have used this technique to study plasmonic coupling between nanoparticles with different spacing [106, 142, 72, 21]. These nanoparticle arrays are the backbone to creating LSPR as they confine the electrons to oscillate together and do not allow them to couple to neighbors localizing the oscillations.

There have been several approaches to measure LSPR spectra. If the sample

is optically transparent then transmission white light spectroscopy can be used, see Figure 10 (a). This uses a white light source coupled into a fiber allowing the light to pass through the nanoplasmonic array and this light is then coupled into a spectrograph with CCD ultimately allowing for the user to determine the LSPR. This is not always possible, if the sample is opaque to a white light source, reflective white light spectroscopy has to be used, see Figure 10 (b). This sends light onto the sample and collects the reflected light into the spectrograph with CCD. If one is looking for measuring a single nanoparticle these two methods are generally not the best for this as dark field microscopy is best for this, Figure 10 (c). This focuses light down using a high NA objective and introducing an aperture in the beam path to limit the light that the detector sees, ideally only signal from a single nanoparticle will be seen.

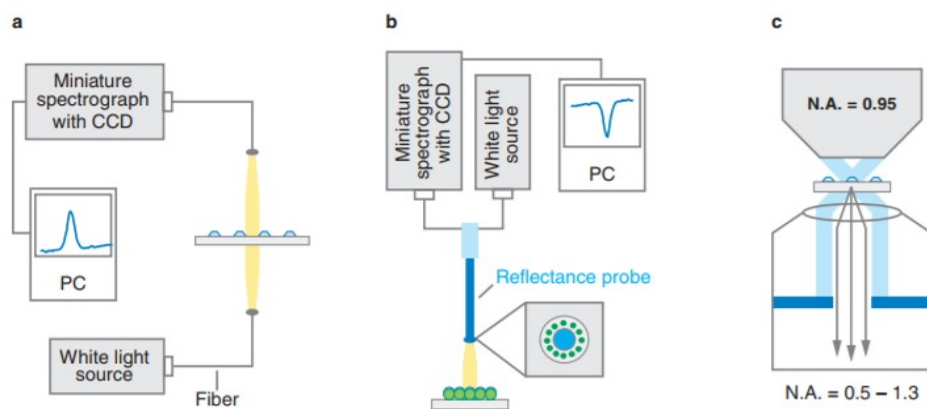


Figure 10: (a) Transmission and (b) reflection geometries for measuring extinction spectra of nanoparticle arrays. (c) Dark-field scattering experimental setup for measuring single-nanoparticle scattering spectra. [179]

One way of controlling the shape and size is the use of electrochemical oxidation, this is often times used with spectroscopy in order to observe systematic trends of the different nanoparticles. These techniques are rather important due to the inherent heterogeneity among individual nanoparticles and single-nanoparticle spectroscopy

[222] can be used to find a true distribution of resonance wavelengths for a given shape and size of nanoparticle. The use of these techniques have shown that shapes such as rods, triangles, and spheres [178] show different refractive-index sensitivities. There are two conditions one must look at in order to state a nanoparticle yield a new plasmon resonance: (1) Its near fields must be most intense at the polar regions of the nanoparticle, and (2) it must be thicker than the skin depth of the material [222].

To understand the relationship between the evanescence EM-field decay length and relative properties of the material, researchers have conducted initial experiments by measuring LSPR wavelength shifts of NSL-fabricated triangles using self-assembled alkanethiol monolayer and multilayers to understand the short-range and long-range distance dependence of the evanescent field [91, 90]. They concluded that LSPR frequency shift decreases when (a) the nanoparticle in plane width increases or (b) the nanoparticles out of plane height increases [91, 90].

The use of atomic layer deposition (ALD) [83, 194] has shown that even a single atomic layer of metal will shift LSPR and the sensitivity decreases with nanoparticle out of plane height, see Figure 11.

With extreme attention to detail Dieringer et al [60] proved that the distance dependence of SERS actually fits an equation:

$$I_r = \left(1 + \frac{r}{a}\right)^{-10} \quad (15)$$

Where I_r is the intensity of the Raman mode, a is the size of the nanoparticle,

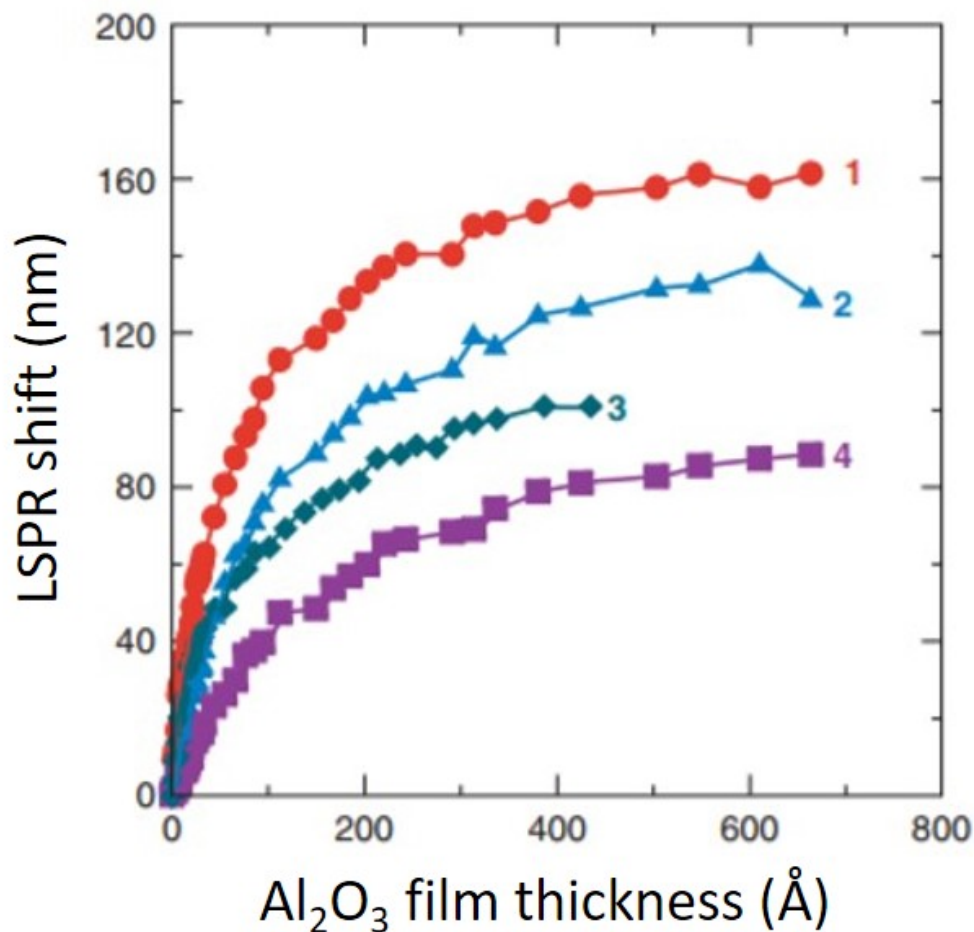


Figure 11: Localized surface plasmon resonance (LSPR) shift versus Al_2O_3 film thickness for (1) 30 nm thick Ag triangles with in plane widths of 90 nm, (2) 40 nm thick Ag triangles with in plane widths of 90 nm (3) 52 nm thick Ag hemispheres with in plane width of 104 nm (4) 51 nm thick Ag triangles with in plane widths of 90 nm. [60]

and r is the distance from the surface to the adsorbate.

Another areas that LSPR is used in spectroscopy is in Surface-enhance resonance Raman scattering (SERRS) [99] which has shown enhancement factors on the order of 10^{11} - 10^{12} . These are used mostly when the LSPR is close to the resonance of the molecule of interests. These wavelengths shifts are vastly different than what is expected based on simple refractive-index changes.

1.4 Super Resolution Nanoscopy

The concept of resolution is one of the main focuses of this dissertation. There are two distinct types of resolution that ultimately matter, axial resolution and lateral resolution. We will be focused on spatial resolution, where a conventional far-field imaging system is ultimately restricted by the diffraction of light. A point object in the object plane will result in a finite sized object in the image plane, as a manifestation of the diffraction limit. If the object on the object plane is a theoretical direct delta function then the resulting image is a consequence of a convolution between the delta function and the point spread function of the imaging system [93].

This limit is present in all imaging systems; including aberration-free imaging systems. In order to quantify the resolution of an imaging system several criteria have been proposed such as Abbe [2], Rayleigh [192], Sparrow [207], and Houston [110]. All of these criteria are built around the minimum separation of two theoretical point sources projected onto an image plane and having the ability to distinguish the objects in the resulting irradiance pattern. All these have several assumptions, one of which is an incoherent light source.

Ernst Abbe developed a theory that images formed due to light diffracted by an object [2]. The collection of light of this diffraction process is limited due to the finite size of lens of the microscope objective. Abbe theorized this diffraction limited imaging system where Helmholtz [71] ultimately solved it mathematically, although Abbe generally gets the credit for the limit:

$$\varepsilon = \frac{\lambda}{2NA} \quad (16)$$

Where λ is the wavelength of the object, ε is the resolution, and NA is the numerical aperture of the optical system.

Lord Rayleigh [192] has a resolution criterion that is based on a common sense concept. This concept is that for two point sources, the resulting finite irradiance pattern has one point that has a minimum at the second points maximum. It can be shown that this definition leads to the following formula:

$$\varepsilon = \frac{0.610\lambda}{NA} \quad (17)$$

The Sparrow [207] resolution criteria is due to the, undulation condition, and is very sensitive to irradiance differences. This makes this criterion appealing when there are no well-defined zeros in the image.

$$\varepsilon = \frac{0.473\lambda}{NA} \quad (18)$$

The final and most useful resolution criterion, known as Houston [110], was proposed in the early 20th century that stated that two equal intensity point sources are resolved if the distance between the central maxima of the summation of their irradiance profiles is equal to the full-width half maximum (FWHM) of the irradiance profile of either point.

$$\varepsilon = \frac{0.515\lambda}{NA} \quad (19)$$

It should be noted, that these criteria neglect to consider signal-to-noise (SNR), which is always present during experimental measurements. It is considered to be a super resolved image is the resolution of an object goes beyond these criterions. There are several different ways of achieving this but there is always information about the object before the post processing is done. Some of these techniques are structured illumination microscopy (SIM) [85], Stimulated Emission Depletion Microscopy (STED) [105], Photo-Activated Localization Microscopy (PALM) [33], and Stochastic Optical Reconstruction Microscopy (STORM) [199], see Table 1 for a short explanation of each.

We will also be looking more carefully at specific super resolution microscopy such as Scanning near field coupling, metamaterial lenses, non-linear effects, and the theory of microspherical nanoscopy.

1.4.1 Scanning Near Field Coupling

From the Abbe limit it is a powerful tool in determining the two different features to obtaining finer features. These being decreasing the wavelength of light and increasing the index of refraction of the object plane. There are limitations of these though. The first one being that ultraviolet light is not always desirable owing to the high risk of irreversible damage to the sample, especially biological objects. And for the high refractive index larger refractive indices always follows with absorption and chromatic dispersion [14].

For the past seven decades researchers have focuses on evanescent waves and evanescent fields. The focus is due to the fact that evanescent fields are fundamentally

Table 1: Information on different methods of breaking the diffraction limit and achieving a super resolved image [214]

Super Resolution Methods			
	Structured Illumination Microscopy (SIM)	Stimulated Emission Depletion (STED) Microscopy	Photo-Activated Localization Microscopy (PALM) and Stochastic Optical Reconstruction Microscopy (STORM)
Principle	Uses interference generated light patterns to create a moire effect from which higher information can be extracted	Reduces the effective excitation volume with a depletion laser	Stochastically activates photoswitchable probes at a time, and then determines the centroid position of each point spread function.
Microscopy	Wide-field	Laser scanning confocal	Wide-field
Lateral resolution	100-130 nm	20-70 nm	10-30 nm
Axial resolution	~ 300 nm	40-150 nm	10-75 nm
Temporal resolution	Milliseconds to Sec.	Milliseconds to Sec.	Sec. to Min.
Photodamage	Low to moderate	Moderate to High	Moderate
Photobleaching	Moderate to high	Moderate to high	High for single fluoreophores, low overall
Considerations	Straightforward multicolor experiments and sample preparation. Reconstruction algorithm may cause artifacts.	Best temporal resolution at the highest spatial resolution; however, maximal in plane can be at the expense of axial resolution	Highest spatial resolution; however, sensitive to labeling density. Crosstalk between fluorophores

different than propagating fields. The effective wavelength allows for researchers to break the diffraction limit of visible light. The wave vector of evanescent waves have a form:

$$K_e = k_p + ik_o = \left(\frac{2\pi}{\lambda}\right)^2 \quad (20)$$

Where k_p is the parallel wave vector at the boundary and k_o is the perpendicular wave vector at the boundary. This shows that a subdiffraction-limited detail can be visualized using the evanescent field [93], as long as this detail is captured, magnified, and projected to the far-field. Near field scanning optical microscopy (NSOM) uses a probe, originally a sharply pointed metal object with a sub-diffraction aperture at the tip. This was used to scatter and collect the evanescent field to resolve details below the diffraction limit, see Figure 12. This is an illustration of what a near-field probe looks like for a typical NSOM device. It allows for illumination and detection from the probe through an aperture at the end of the probe. The advances in NSOM lead to other probe detection techniques; such as scanning tunneling microscopy [36] and atomic force microscopy [198].

1.4.2 Metamaterial Lenses

In 2000, John Pendry [190] published his paper with the concept of having materials with the permittivity and permeability both be negative. These materials have come to be known as metamaterials. This concept shows that it is possible to have a, "perfect lens," $n=-1$. This lens has the power to focus all Fourier components, both propagating and evanescent, of a two-dimensional image. Pendry proposed this

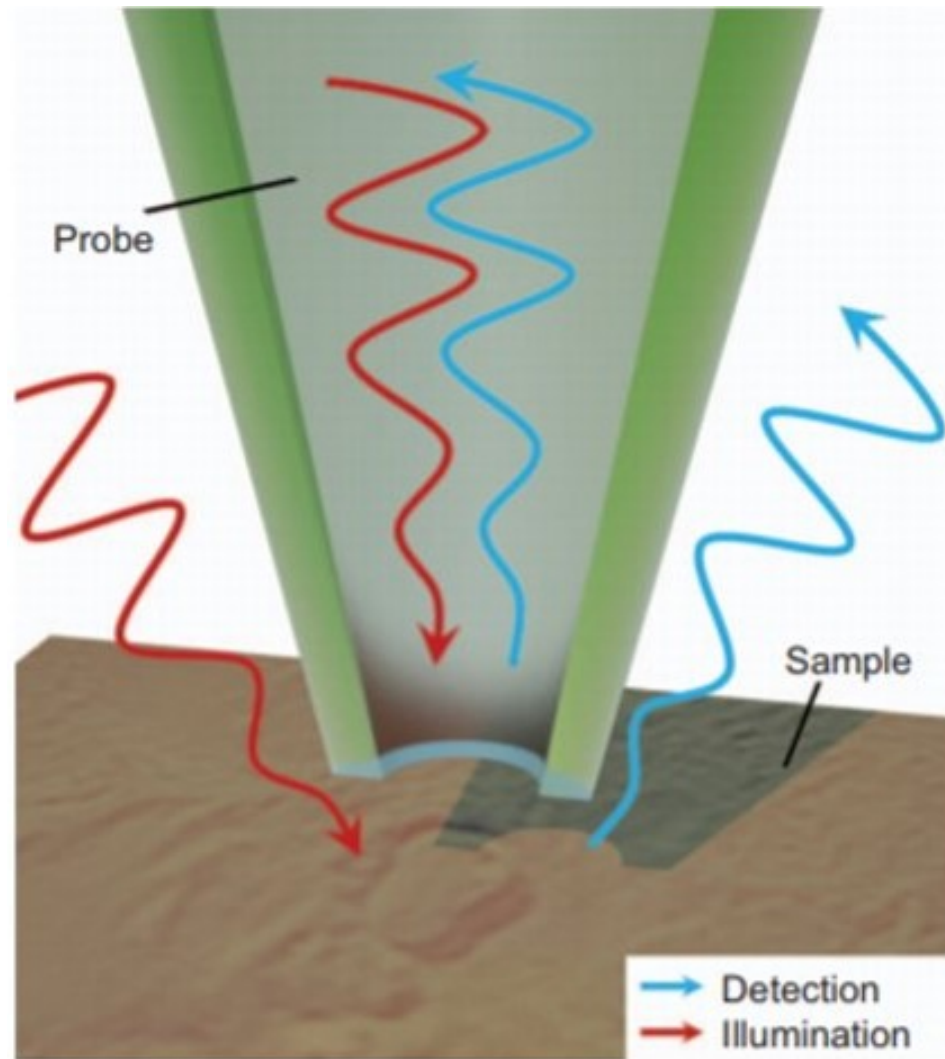


Figure 12: Schematic illustration of the near-field scanning optical microscope (NSOM). Depicted here is a probe with an aperture which is used to illuminate and collect near field information from an evanescent field generated by the sample.[93]

using a silver slab and showing the electric field generated at the object plane being near delta functions and the electrostatic field at the image plane will carry much higher frequency information when using this silver slab, see Figure 13.

This concept of a metamaterial lens further progressed after Pendry published his paper. The concept is to couple the information of the near field and project the effect into the far field. The super lens [224] did this by inscribing the object in

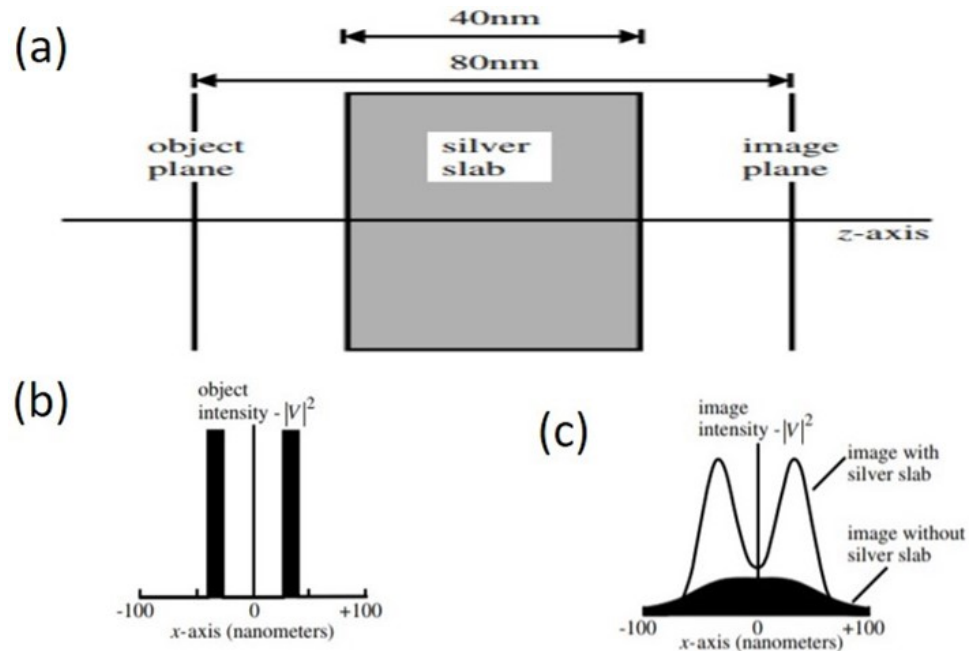


Figure 13: (a) View of the new lens in operations. A quasi electrostatic potential in the object plane (b) electrostatic field in the object plane (c) electrostatic field in the image plane.[190]

chrome (Cr). Then layering 40 nm of PMMA photoresist on top of the Cr object. placing a 35 nm thick silver film on top of the PMMA photoresist. They then recorded the image in another layer of photoresist directly on top of the Ag, see Figure 13 (a). Ultimately Pendry's lens forms an image on the opposite side of a slab but still needed to be seen by the far-field optics, and, at this stage, the super-resolution would be lost.

More work was done by Liu et al [162], see Figure 14 (b), with optimal parameters $a = 35$ nm, $b = d = 55$ nm, $c = 100$ nm, $e = 45$ nm, and $f = 105$ nm to generate a far-field optical super lens. That group ended up expanding on this idea for the two dimensional far field super lens, see Figure 14 (c), made up of 20 pairs of 15 nm/20nm dielectric and Ag-dielectric subwavelength gratings. The thickness is 55 nm, period

is 160 nm, and Ag filling ratio is 0.3 [224]. The group ultimately created a hyperlens, see Figure 14 (d), which is a half-cylindrical cavity fabricated on a quartz substrate with a periodic stack of 35 nm of Ag and 35 nm of Al_2O_3 [163]. This method solves the problem of the super resolution being seen by the far-field optics by amplification of near fields followed by the diffraction at the surface grating.

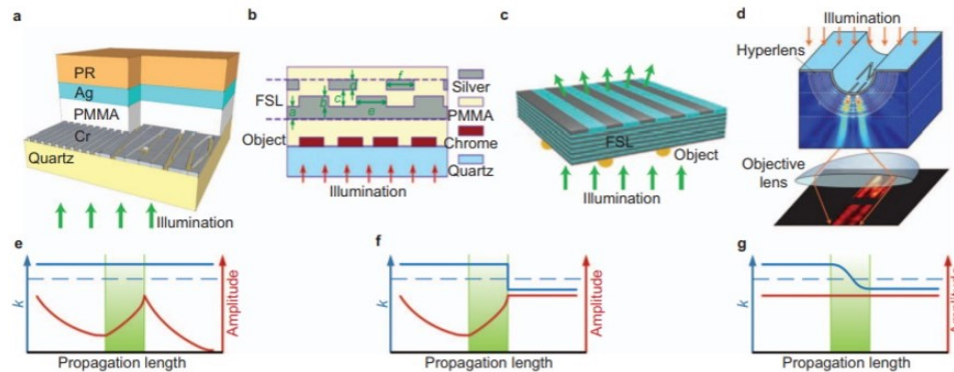


Figure 14: Schematic of (a) superlens, (b) far-field super lens, (c) 2-D far field super lens (d) hyperlens. theoretical comparison (e) Superlens (f) Far-Field Superlens (g) Hyperlens [69, 162, 224, 163]

1.4.3 Non-Linear Effects

Evanescence fields are such a powerful concept and can, in theory, have infinitely small resolution. Work has been done to introduce an exponentially decaying field to an optical system. By introducing the evanescent field illumination from a fiber, see Figure 15 (a), and imaging different planes, see Figure 15 (b-e), we have a better understanding of the effect of introducing this evanescent field as the illuminating wavelength. They did this by flame heating and drawing a commercial single mode fiber and then precisely positioning the fiber onto the sample using a piezoelectric positioning stage.

In this experiment they positioned a fiber directly on top of the desired pattern

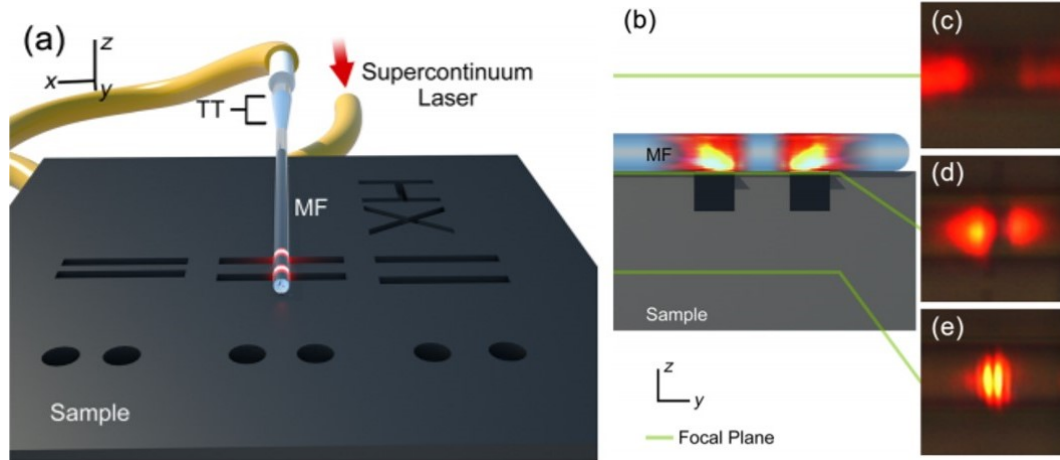


Figure 15: (a) 3D structure of experimental system. (b) the relative position of micro-fiber, sample, and focal plane, (c-e) images of the sample obtained in the experiment.[95]

and imaged the system using a microscope. It is clear from the figure that when imaging through the micro-fiber and obtain resolution enhancement from the coupling of the evanescent field.

1.4.4 Theory of Microspherical Nanoscopy

In 2011, Wang, et. al, [220] showed the ability to resolve objects with sizes less than 100 nm in size. They did this using silica microspheres with index, $n \approx 1.46$, and sphere sizes ranging from, $D = 2 \mu\text{m}$ to $9 \mu\text{m}$. These microspheres were deposited onto a sample and a virtual image was captured by imaging through the sphere, see Figure 16. This figure shows the SEM image of stripes which are 360 nm thick and separated by an edge to edge gap of 130 nm, see Figure 16 (a), as well as a GeSbTe nano star with 90 nm corners, see Figure 16 (c). The virtual image of each respective structure is shown in Figure 16 (b,d).

In this original paper the authors lay claim that the resolution that can be achieved is 50 nm for white light illumination [220]. The interpretation of the ob-

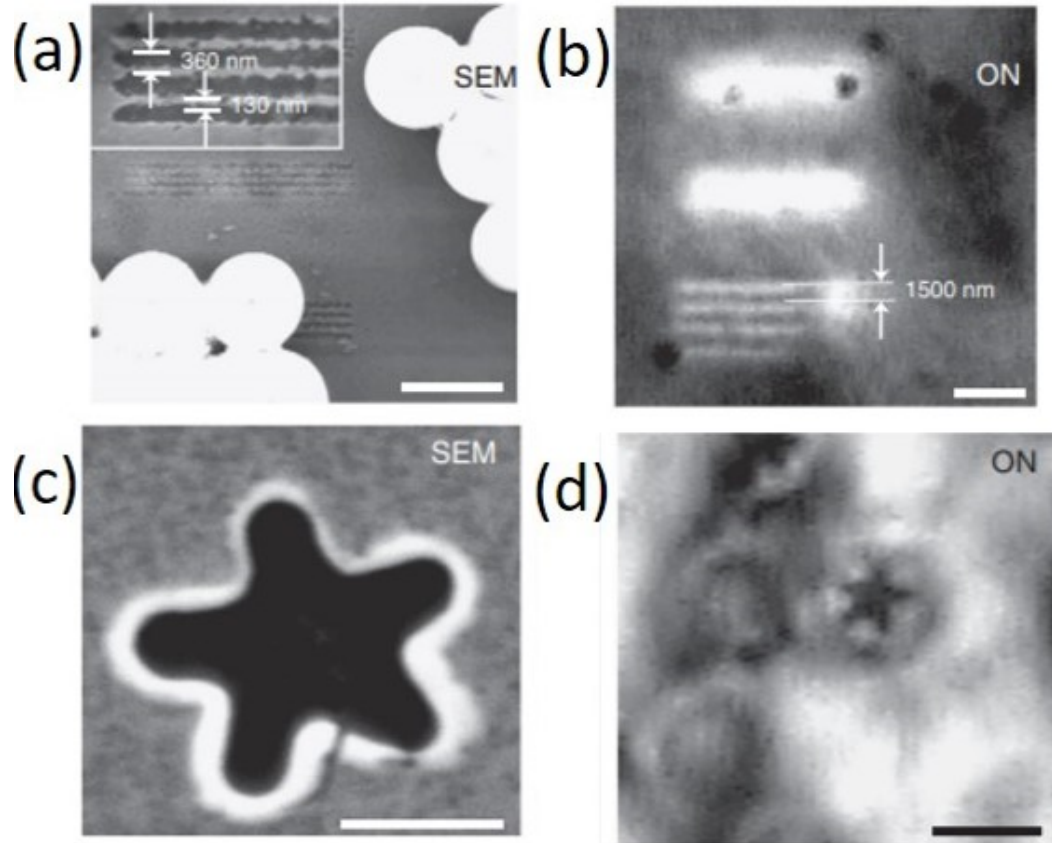


Figure 16: (a) Microsphere superlens imaging of 360-nm wide lines spaced 130 nm apart (b) Reflection mode imaging of a nano star structure made on GeSbTe thin film. (c) Virtual image of (a). (d) Virtual image of (c). Scale bar 500 nm SEM and 5 μm [220]

served effects was made based on the reciprocity principle which allows to relate sharp focusing by microspheres to their super-resolution properties. However, the close analogy between the focusing and imaging application of microspheres is not apparent and the rigorous application of the reciprocity principle suggested in [?] requires further experimental and theoretical proof. The refractive index of the sphere is the main limiting factor of this imaging through the microsphere, $n_{\text{sphere}} < 1.8$.

More recently a group of Prof. Vasily Astratov has given more insight into this microsphere-assisted optical super resolution technique [52]. This work has been

developing over several years and the biggest stride involves the limitation of the refractive index of the sphere [28]. Initial experimental set ups involved imaging an array of Au nanoplasmonic dimers and commercially available Blu-ray disks. These used high index microspheres, $n \approx 1.9-2.1$, that were fully immersed in a contrast agent, see Figure 17 for experimental comparison. The information that is necessary is the edge to edge gap which is g , the pitch d , and the diameter of the object D . From Figure 17 (a) g is 60 nm, d is 150 nm, and D is 100 nm. Figure 17 (b) shows the virtual image acquired by using a 15 μm BTG $n \approx 1.9$ microsphere directly on the lattice shown in Figure 17 (a). Figure 17 (c,d) shows the results of conventional microscopy and confocal microscopy of the same structure. It is clear that more detail can be seen by the microsphere assisted microscopy technique.

Using this technique resolution values of $\sim \lambda/7$ were found for wavelength-scale spheres using the discernibility of the smallest features as a semi-quantitative resolution criterion. This beats the diffraction limit set forth by Abbe in Eq. 12. But for larger spheres the resolution decreased down to this diffraction limit set forth in Eq. 12. Although with greater resolution limitations on the field of view can be seen as a linear function of the diameter of the sphere [52].

The defining feature of a microscope system as it is stated previously, in [52] the resolution is quantified using the discernibility of the smallest features as a semi-quantitative resolution criterion. This approach was further developed in [14] where a convolution with 1-D point spread function was used for calculating images objects which in real physical geometry were represented by circles with 2-D geometry. This approach can be viewed as an advance compared to initial work represented in [220,

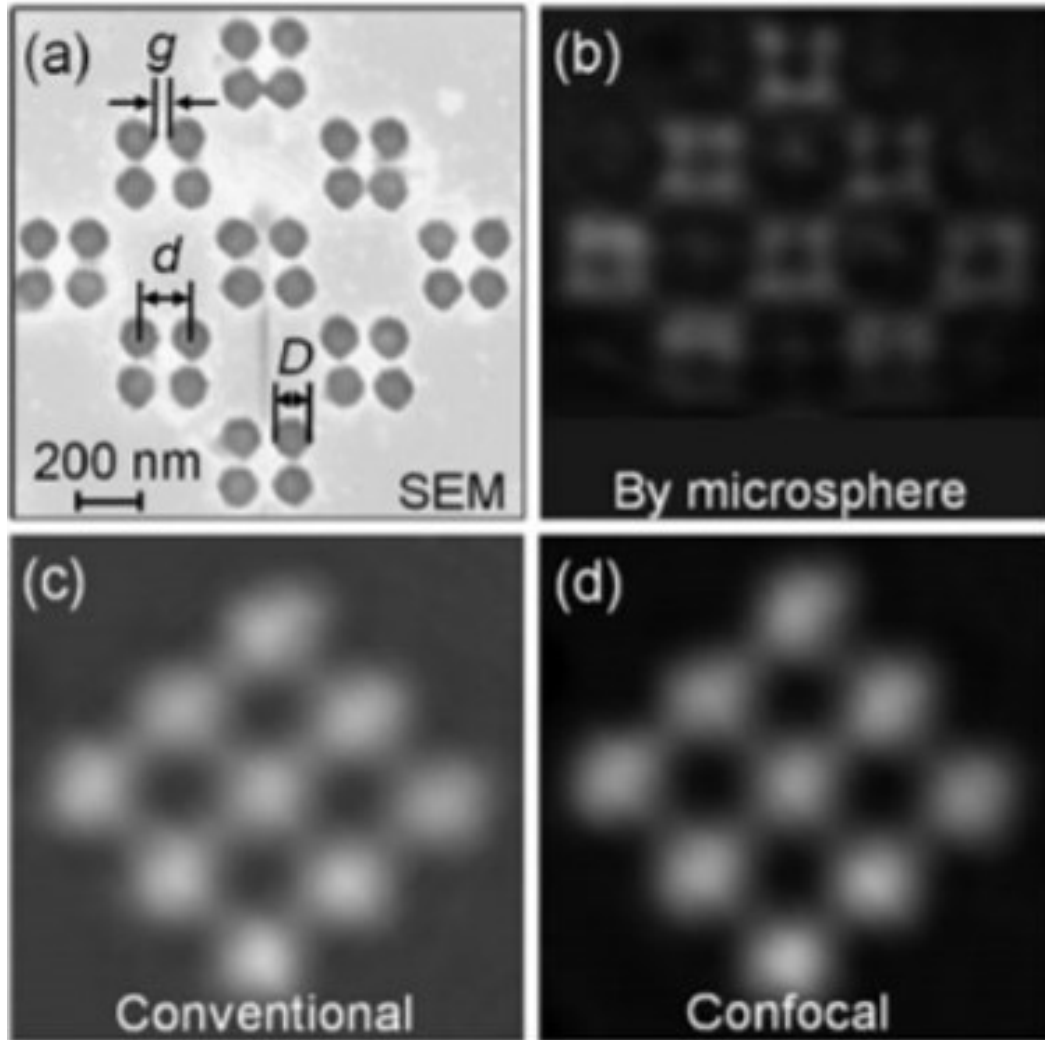


Figure 17: (a) SEM of Au nanoplasmonic structure. (b) microspherical microscopy. (c) image of conventional microscopy (d) Confocal microscopy. [14]

52], but it is still only a step towards a proper and more complete resolution quantification procedure based on using stand-alone objects with 2-D geometry (in fact, all objects have 3-D geometry, but the thickness is usually a small parameter convoluted with 2-D point spread function. This correct and complete approach was not used before the further development of this work took place in the Ph.D. dissertation of Dr. Kenneth Allen defended in 2014 [10, 11, 14]. The technique of using microspheres for imaging have shown to have a higher resolution over conventional and confocal

methods of microscopy, see Figure 17.

1.5 Focal Plane Array Enhancement

Thermal imaging devices operate in a range of wavelengths (λ) from 3 to 5 μm , these imaging devices are typically called mid-wave infrared (MWIR) focal plane arrays (FPAs). We are going to focus on this realm as they are critical components in many military and civilian applications and imaging systems. These sensors are highly anticipated for Astronomers in particular [197]. This is because of the transmission window in the atmosphere in the IR regime [67]. The history of the IR detector began during the 1940s and have been growing rapidly in the past three decades, see Figure 18. It is clear from the figure that until HgCdTe detectors in the 1st generation which is just a scanning system dominates the infrastructure for the advancement in IR detectors. The 2nd generation which is a staring system-electronically scanned ultimately lead to the 3rd generation. This generation differs from the previous generation with respect to the amount of pixels that the detector has as well as having the ability to read out two distinct colors. The step up to the 4th generation is again an increase in the amount of pixels that the detector has as well as the amount of colors, increased to 4, and an on-chip functionality. It should be noted that thermal detectors were used for IR detection before 1940 and still dominate the market today.

Most modern infrared photodetectors today are often called focal plane arrays (FPA). They have been around since the mid-1970s and are typically operated at cryogenic temperatures [195]. These devices are cooled in order to decrease the noise that the photo detector has. This noise has a multitude of mechanisms associated

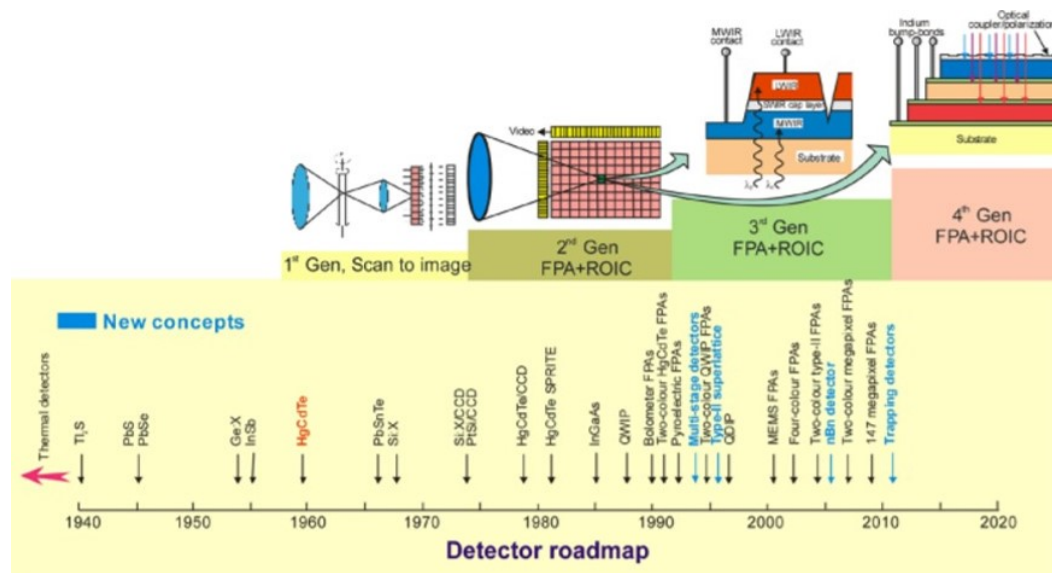


Figure 18: The history of infrared detectors. [197]

with it; however, the main contribution of noise that we are going to focus on is noise associated with the dark current of the detector. The ultimate goal is the fabrication of high operating temperature (HOT) detectors which are detectors that have a dark current less than the system background flux current [197]. An added benefit of increasing the working temperature is the reduction of the size, weight, and power consumption. If the same detector goes from working at 80 K to 110 K, the power consumption is reduced 30%; however, if one were to want to efficiently increase the operating temperature the detector itself would decrease in size. This decrease in size will also decrease the weight and power consumption of the device as well, see Figure 19.

The idea of HOT detectors the size, weight, and power consumption of the device can be improved. Although this is the ideal situation and with cooled detectors the sensitivity is generally the limiting factor with uncooled IR imaging systems it seems to be limited by pixel resolution rather than sensitivity [148]. Pixel reduction is

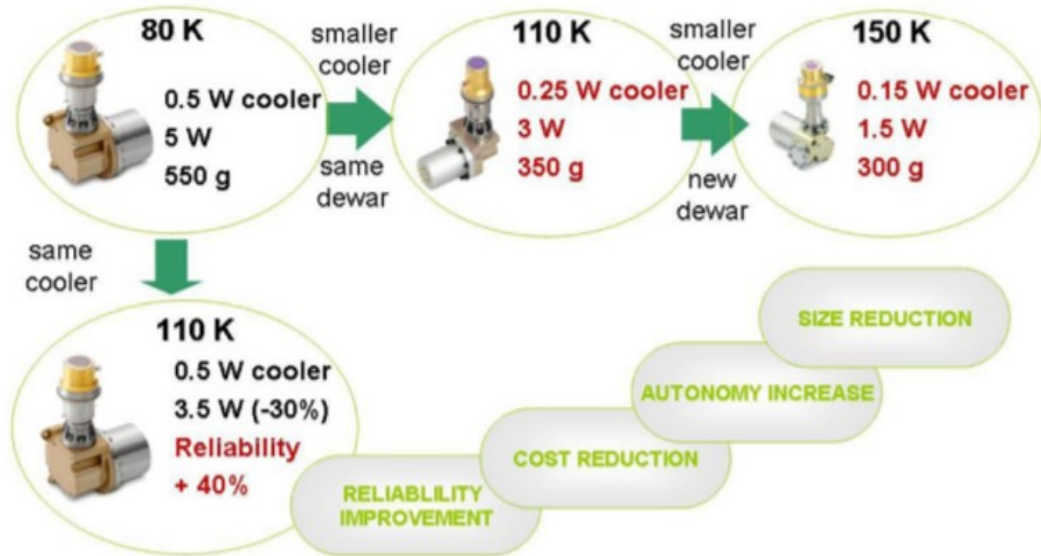


Figure 19: Higher operating temperature HgCdTe detectors showing different size weight and power consumption for different detector types [169].

mandatory for reducing the cost of the optical system. The fundamental pixel size is limited by the diffraction of light [63, 109]. The diffraction spot is defined as:

$$d = 2.44\lambda F \quad (21)$$

where d is the diameter of the airy disk spot, λ is the wavelength, and F is the F-number of the optics above the detector. This is important to when looking into the actual system itself, as if the IR system is detector-limited decreasing the detector size has a dramatic effect [101]. Whereas, if the IR system is limited by the optics above the detector decreasing the detector size has a minimal effect on performance [108]. This comes about from the distinction between wide field-of-view systems (WFOV) and narrow field-of-view (NFOV) systems. WFOV have relatively low F-number with shorter focal lengths whereas NFOV have relatively high F-number with longer focal lengths. With short focal lengths the material properties dominates the operation of

the detector whereas with longer focal lengths the optical properties dominate the detector, see Figure 20. It needs to be noted that there are several challenges that must be addressed in fabrication of FPA, these being: (1) pixel delineation, (2) pixel hybridization, (3) unit cell capacity, and (4) dark current [131, 132].

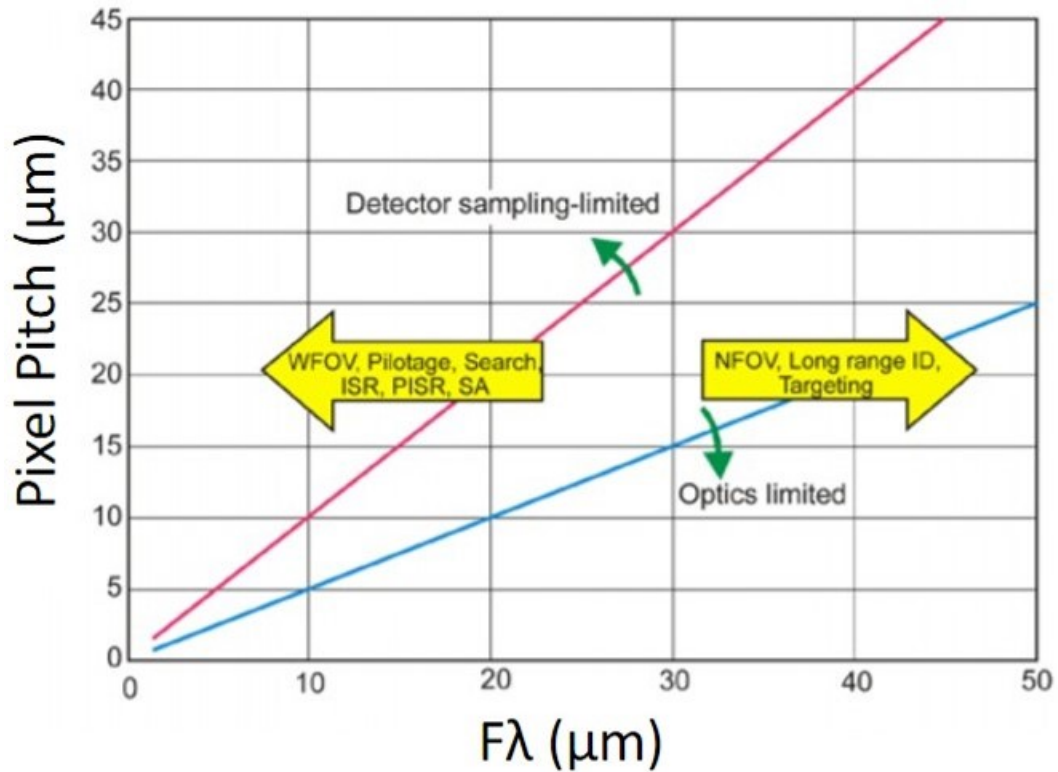


Figure 20: Classical infrared system design [63].

1.5.1 Materials and Structure of IR Detectors

There are several different types of accepted FPA ranging from HgCdTe photodiodes, see Figure 21, InSb FPAs, see Figure 22, nBn FPAs, see Figure 23, and microbolometers, see Figure 24. The microbolometers are currently the dominant type of uncooled IR detector technology with more than 95 percent of the market as of 2010 [196]. These microbolometers, see Figure 25, are typically made from VO_x material; however, other types of microbolometers are made from amorphous silicon,

barium strontium titanate (BST), and silicon diodes.

In Figure 21 there are two distinct types of detectors; Mesa, see Figure 21 (a), and Planar, see Figure 21 (b). Mesa detectors generally are much more difficult to fabricate and can lead to faulty pixels and have a lower dark current as the dark current is proportional to the active region and having a mesa shrinks this area. Planar detectors are generally easier to fabricate but suffer from having a larger dark current as the entire area of the detector is taken is a part of the active region of the detector.

Figure 22 depicts a typical InAsSb p-i-n detector. This is typically a layer for contact and reading out the photocurrent which is followed by an absorbing volume which is the largest volume in the detector, shown to be $3\ \mu\text{m}$ thick. There is a barrier layer placed directly on top of this absorber to ensure that there is a difference in the two contact layers for reading out. This layer is made of a different material as well. The barrier layer is depicted at being $0.3\ \mu\text{m}$ thick and made of AlAsSb instead of InAsSb.

The final type of photodiode that is presented is the nBn detector. This is a n type barrier n-type detector array. Similar to the InAsSb detector only instead of having a p-type substrate to n-type, it is both n-type. Figure 23 depicts a GaAs substrate with the absorber and collector layer being separated by the barrier layer. Each collector is separated from one another into individual pixels in a mesa design. These are generally favorable over the other types of photon detectors as they can be changed to have different spectral bandwidth of operations.

The dominate type of IR detector actually comes from microbolometers. These

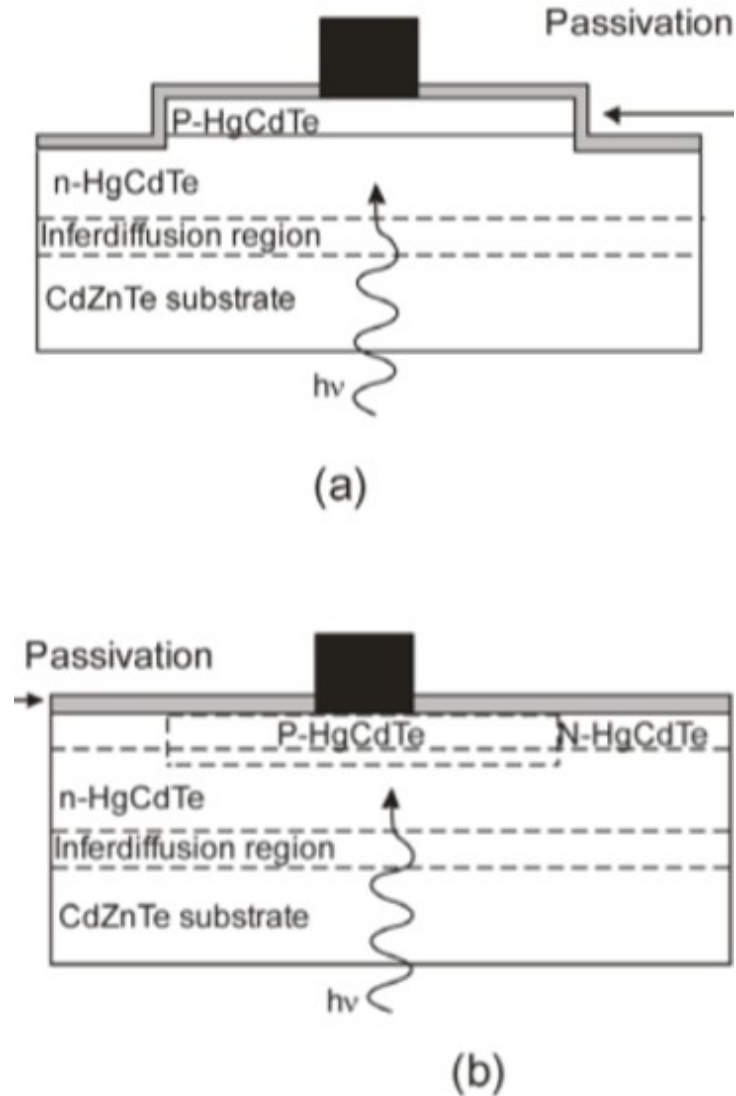


Figure 21: Cross section of n-on-p HgCdTe photodiodes (a) mesa structure, (b) planar structure. [197].

are thermal detectors which returns a signal based on the radiant power incident on the detector. This means that they are relatively insensitive to the spectral content of radiation incident on the detector. The problem is one has to wait for the materials to heat and cool which makes them slower than the photon-based detectors and historically have large center-to-center spacing of the elements. From Figure 24 we see this material for heating and cooling having a beneath the IR absorber and elevated

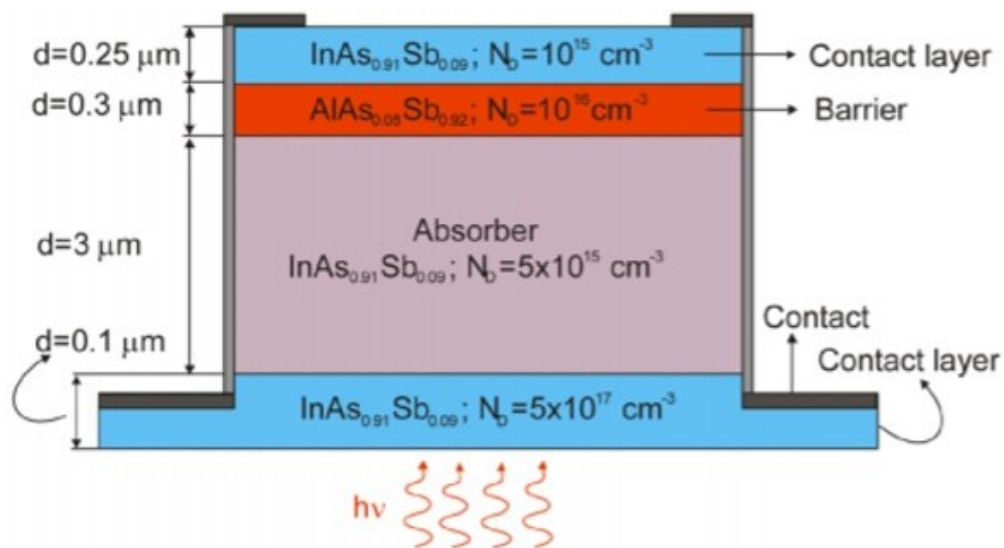


Figure 22: InAsSb/AlAsSb MWIR detector (a) the device structure (b) the dark current density vers bias voltage as a function of temperature. [64].

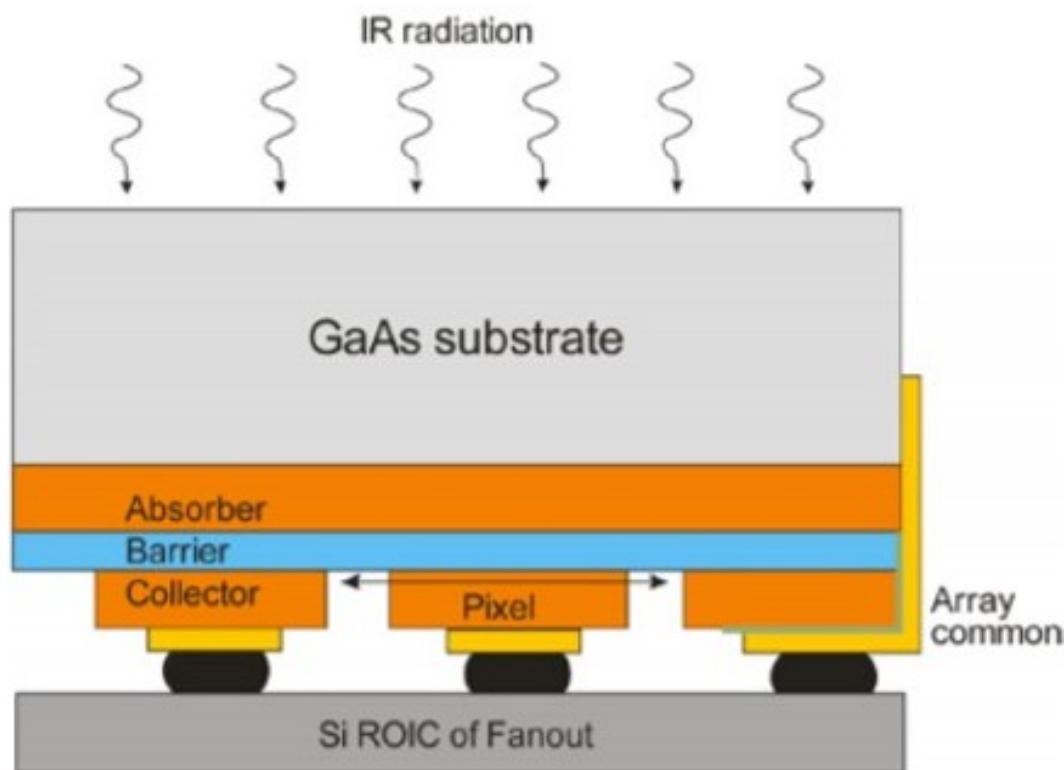


Figure 23: nBn detector array architecture [197].

from the substrate by support legs with a cavity between the material for sensing and the wafer. The wafer is connected to a ROIC, see Figure 24.

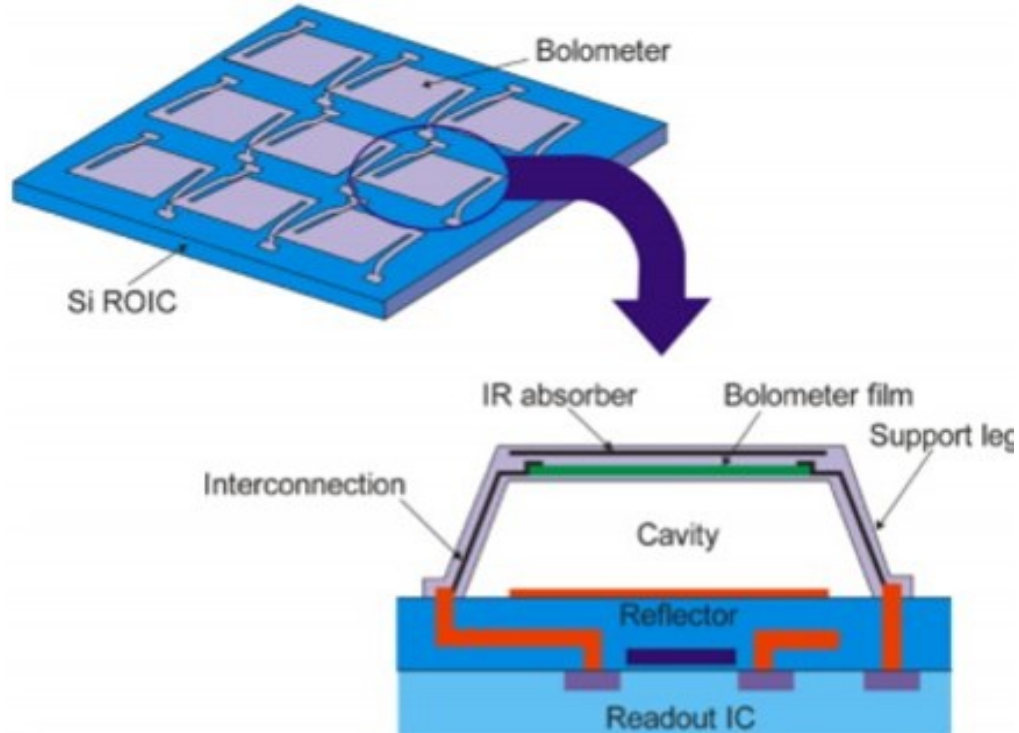


Figure 24: The structure of the microbolometer uncooled FPA and its pixel [197]

Even though for uncooled IR detectors pixel resolution is a limiting factor the sensitivity of the detector is still the parameter that is focused on when fabricating over resolution [130]. This could be due to the difficulty of decreasing the pixel size. Unlike visible sensor, which have a pixel size $\sim 1.1 \mu\text{m}$ in size IR pixels are much more difficult to scale below $5 \mu\text{m}$. This difficulty comes in as, /bump-bonding,/ readout integrated circuit (ROIC), signal integrating capacitance, and SNR. It also needs to be stated that with a decrease in pixel size the photon flux is reduced and because of this reduction integration time for the imaging system is greatly increased.

Looking at (4) of the challenges that are addressed in fabrication of FPAs the dark current [197]:

$$I_{dark} = q(G_{th} * V_{diff} + G_{dep} * V_{dep}) \quad (22)$$

where q is the electron charge, G_{th} is the thermal generation rate in the base region, V_{diff} is the volume of the active region, G_{dep} is the generation rate in the space charge region, and V_{dep} is the volume of the depletion region.

1.5.2 Microlens Array

Microlens arrays are used for collimating or focusing, for illumination, and for imaging [187], see Figure 25. The array is necessary due to the nature of γ generation 2γ detectors having a large number of pixels rather than a single pixel. It functions as a single lens focusing onto a single pixel only in a large amount.

These devices show a potential to reduce the size and simplify the architecture of analytical systems. They have shown advantages in chemical microchips, miniaturized total analytical systems, optical blood gas sensors, imaging systems for photolithography, smart mask lithography, and signal processing [187].

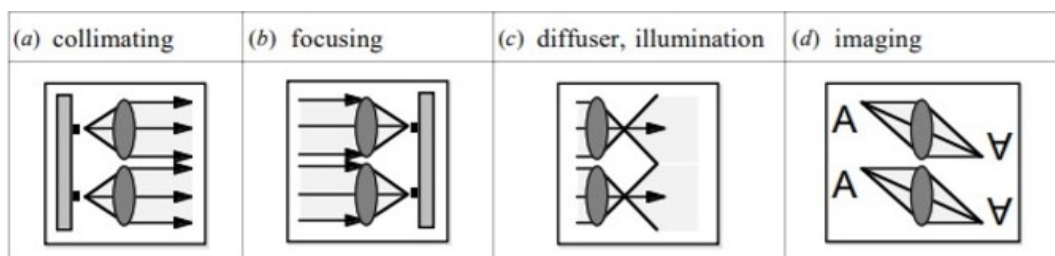


Figure 25: Basic optical functionality carried out by microlens arrays. [187]

1.6 Mie Theory

Initially Gustav Mie wrote a paper in 1908 on light scattering by dielectric spherical particles in order to explain the colorful effects with colloidal gold solutions

[180]. Today Mie's theory is applied to a much broader range of objects involving interstellar dust, near-field optics, and plasmonic characterization. Mie theory is still being applied in many areas because scattering particles are often homogeneous spheres and are approximated such that Mie's theory is applicable.

In Mie's 1908 paper he computed light scattering by small spherical particles using Maxwell electromagnetic theory [180]. He did this to explain the color of gold solutions which later has been interpreted in terms of surface plasmon resonances. Mie was not the first person to formulate electromagnetic scattering problem, which is commonly referred to as Mie theory. Alfred Clebsch [46] solved the elastic point source scattering problem using potential functions. His work dealt with perfectly rigid spheres so the problem can be considered differently.

In 1890 Ludvig Lorenz [164] published essentially the same results of Gustav Mie's calculations; however, he did not connect his derivation with Maxwell's theory of electromagnetics.

These calculations did not really receive the attention that they should have due to the scattering problems involved evaluating functions such as Riccati-Bessel functions and are quite extreme to do by hand. It was not until the invention and development of the electronic computer that these functions got the attention they deserved and have been growing ever since.

In order for the computer to process these problems early algorithms had to be developed. Deirmendjian et al. [56], Giese [80], and Dave [53] were the first to develop and publish these algorithms. Nowadays a number of efficient algorithms and FORTRAN programs are available.

Traditional Lorenz-Mie theory describes scattering by a spherical homogeneous dielectric particle illuminated by an incident plane wave; however, in practice this is not always possible. As a laser beam with Gaussian intensity distribution can be what illuminates the object. The scattered field on that has to have the Gaussian transformed into spherical vector wave functions or into a spectrum of plane waves [62].

1.6.1 Born Approximation

The exact equation for the scattering problem is the Lippman-Schwinger equation:

$$|\Psi \rangle = |\phi \rangle + \frac{1}{E - H_0 + i\epsilon} V |\Psi \rangle \quad (23)$$

One way of solving this equation is using perturbation theory which gives the 1st order approximation to be:

$$|\Psi \rangle = |\phi \rangle + \frac{1}{E - H_0 + i\epsilon} V |\phi \rangle + O(V^2) \quad (24)$$

And when one neglects the $O(V^2)$ correction it is called Born approximation. This scattering is good only when the scattering is weak. Most commercial software use this approximation when dealing with solving Maxwell's equations.

It needs to be noted that Mie theory is present throughout all of the work, in one way or another, throughout this entire dissertation. The concepts will be apparent in Chapter 6. An aspect particularly relevant to this dissertation is how scattering depends on the frequency of illumination, as well as the size of the object, see Figure

26.

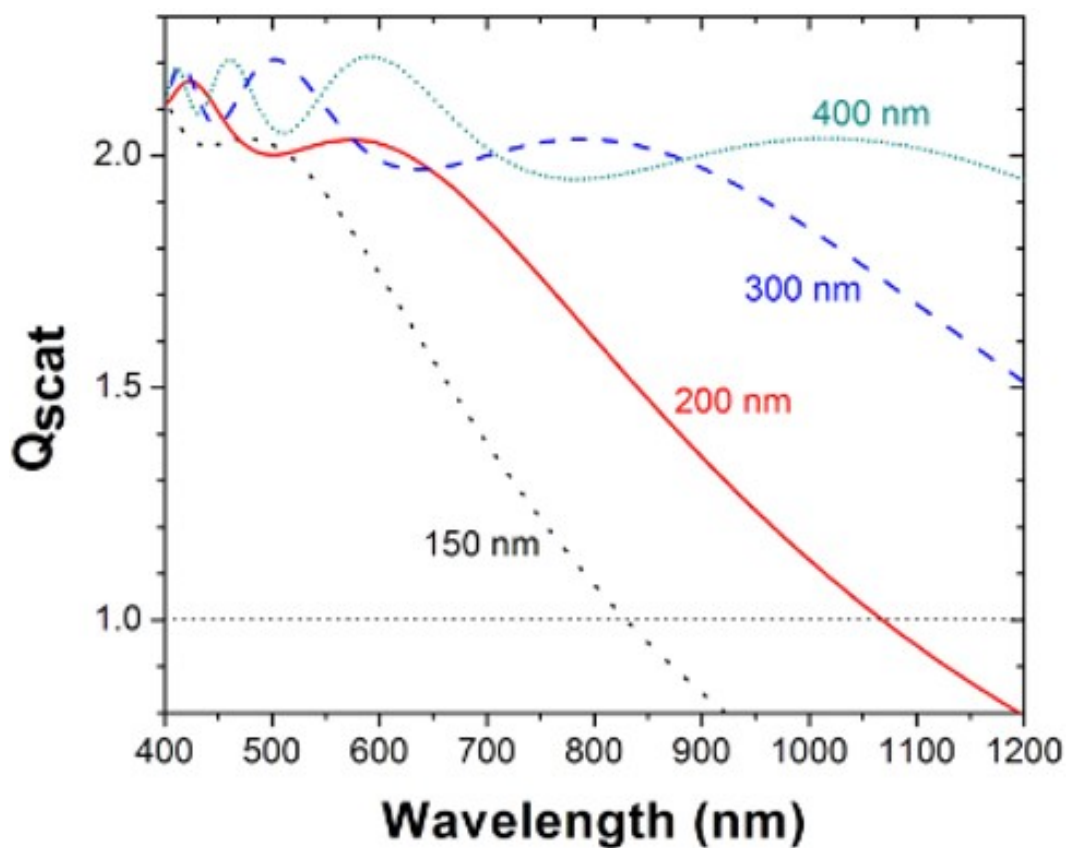


Figure 26: Simulated Mie scattering efficiency of SiO_2 spheres of spheres of different diameters embedded in an infinite medium. [184]

1.7 Photo Induced Aggregation

There are two different kinds of particle aggregation that can be distinguished. One is called coagulation which is when particles almost touch each other without losing their individual geometry. The second is called coalescence which is when particles grow irreversibly together and form a single new particle [236].

In aggregation of particles being dropped in a droplet onto a surface one may experience a so-called coffee-ring effect. This effect shows that there are more particles on the outside of the droplet than the center. There is a complex interplay

of various factors that causes these phenomena from fluid dynamics, surface tension, evaporation, and more. It is so complex due to the fact that evaporating solutions is a difficult to control non equilibrium system. This effect is seen in many systems such as large colloids [55], nanoparticles [35], and individual molecules [125]. Understanding this effect is important in many applications which call for uniform coatings, such as printing [189], genotyping [66], and complex assembly [54].

The ability to avoid the coffee-ring effect, see Figure 27, and control particle deposition could greatly benefit a wide range of applications, most notably for our application optical limiters. To understand this process we must look deeper into evaporating solutions of nanoparticles under different conditions. First we will discuss the process when it is allowed to evaporate just being in air. We then will discuss the difference if we introduce energy to the droplet in the form of light.

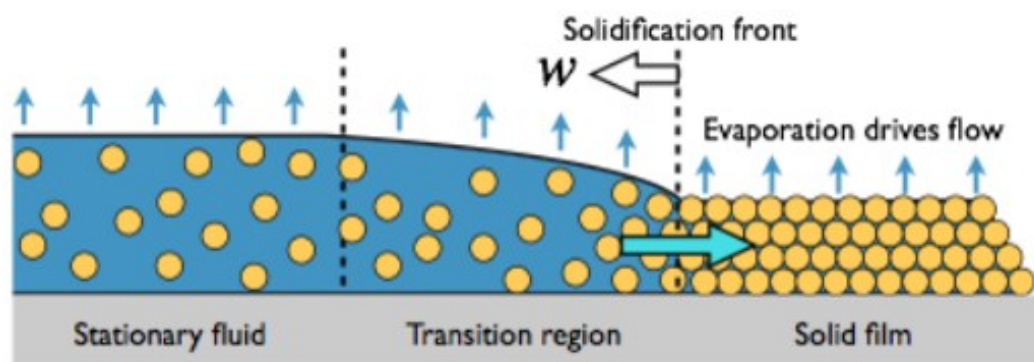


Figure 27: Illustration of the coffee ring effect. [149]

It is well known that evaporation of nanoparticle solutions are dependent on the size and shape of the nanoparticles. Nanospheres will cause a different pattern than Nano ellipsoids [236], see Figure 28. Figure 28 (a) shows a typical evaporation scheme of water on a substrate. When one introduces objects into the water solution

a difference in the residue after evaporation can be seen from ellipsoids, see Figure 28 (b), and spheres, see Figure 28 (c).

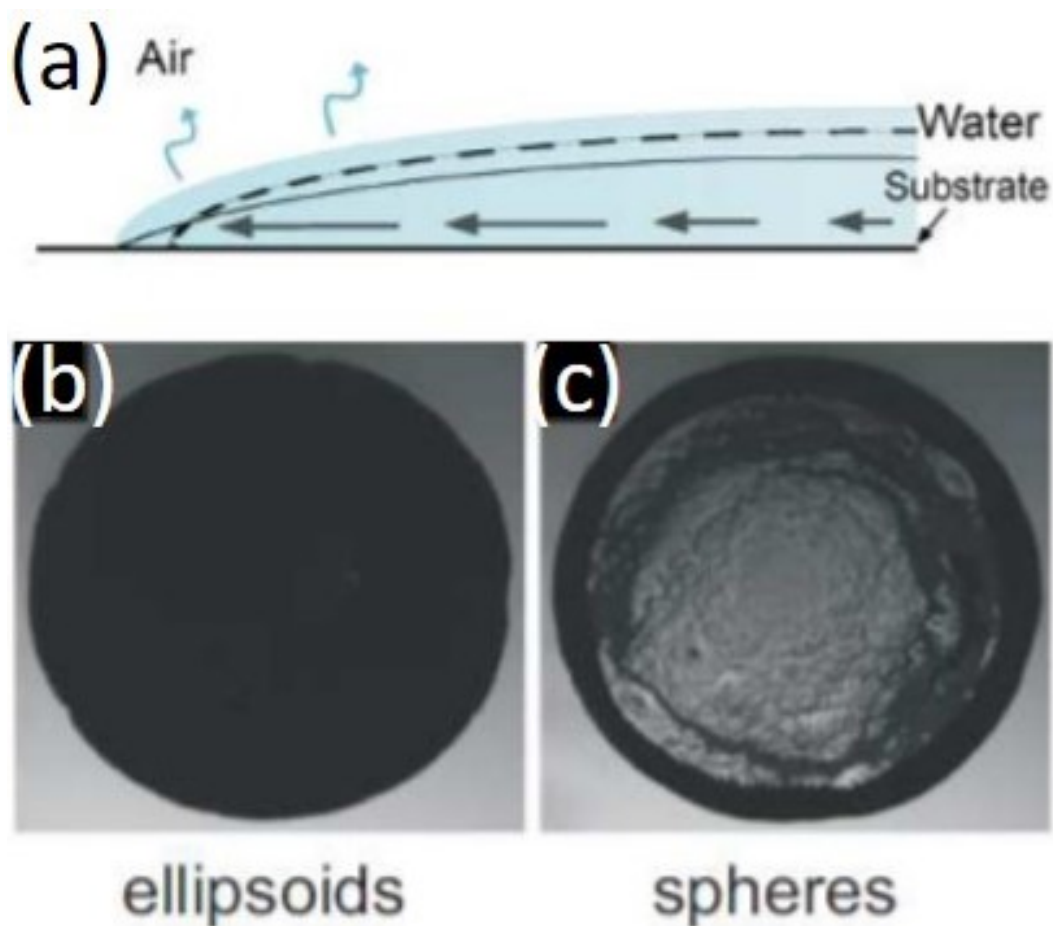


Figure 28: (a) Schematic diagram of the evaporation process. (b) final distribution of ellipsoids. (c) final distribution of sphere. [236]

It is believed that in bulk solutions the shape does not matter and they act similarly to one another; however, at the interface of the solution the behavior is dramatically different. This has been proven using confocal microscopy, see Figure 29.

Along with changing the shape of particles other ways of manipulating the drying behavior have been utilized in the recent years, in particular surfactants. A

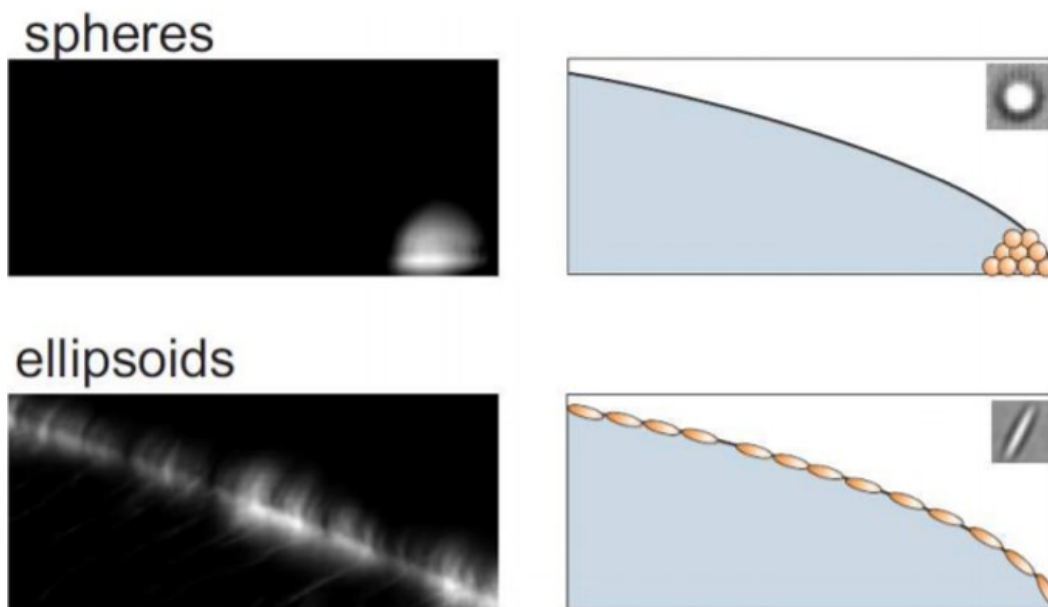


Figure 29: Confocal projections of suspension of spheres (top) and ellipsoids (bottom).[236]

surfactant is a surface-active molecule that consists of a hydrophobic and a hydrophilic part. They populate the interface with the hydrophobic part, //sticking out of the water,// reducing the water's surface tension [209].

The addition of surfactant leads to a flow that is induced from regions of low to high surface tension known as Marangoni flows [235], see Figure 30, and can result from differences in temperature of the droplet. This effect is different than the capillary effect. This is because the surface tension, σ in Figure 30, allows the solution to stick to the surface edge and the evaporation rate of the alcohol is greater than the evaporation rate of different solutions in the wine. This eventually leads to a disconnect between the top of the droplet and the bulk of the droplet. This can be caused by temperature fluctuations in the solution or by gravity. This can also be seen in the temperature difference is from the edge of the droplet and the center

of the droplet when the solution is on a flat surface. It has been shown that for low viscosity fluids n-octane these flows are present whereas when they looked at water these flows were not [201].

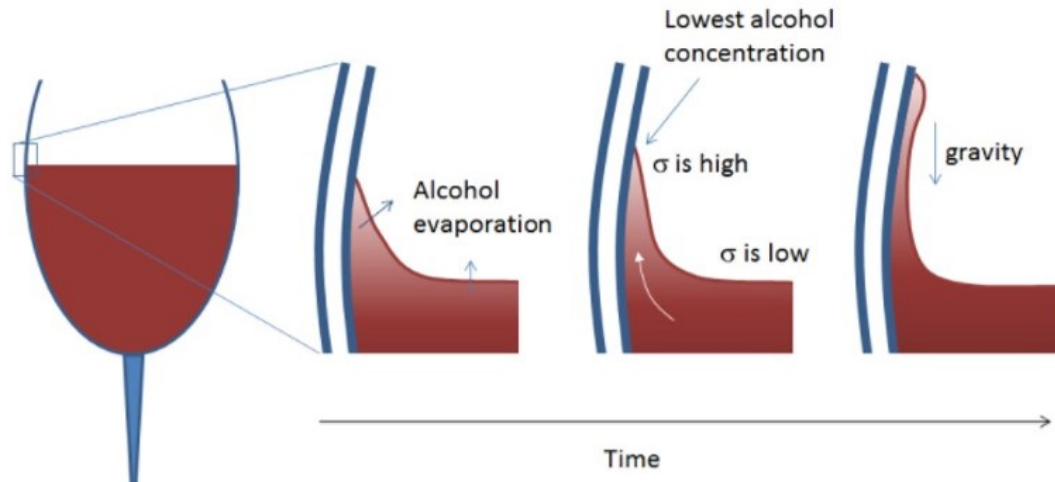


Figure 30: Illustration of the Marangoni effect demonstrated using a wine glass.[1]

When the system is more than just the solution evaporating, things becoming more complex. When adding energy to the system, one must take into account phoretic effects. Thermophoretic forces appear when different particles behave in different ways to a thermal gradient in a solution. A much more widely accepted version for liquid solution is known as the Soret effect. This effect states that when an area is heated the particles in the immediate vicinity of the localized thermal gradient will be pushed away and will show a gap in particles around the heated location. This is because there is a transfer of energy and the particles are imparted momentum away from the heated location to go to a cooled location. Photophoresis is light-induced thermophoretic forces, see Figure 31. These forces are not well understood in the liquid solution domain.

To combat these phoretic forces radiative pressure can be used in order to

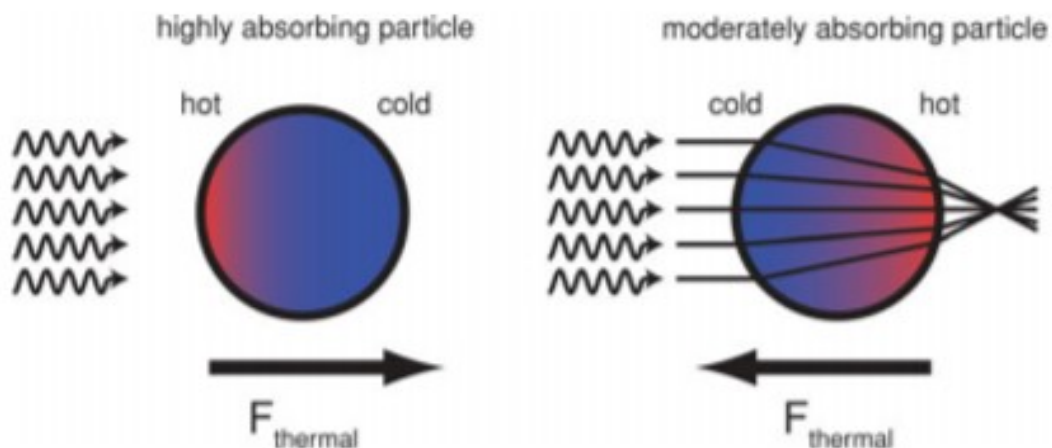


Figure 31: Illustration of photophoretic forces on a particle [20].

optically trap a particle along the path of the light, see Figure 32.

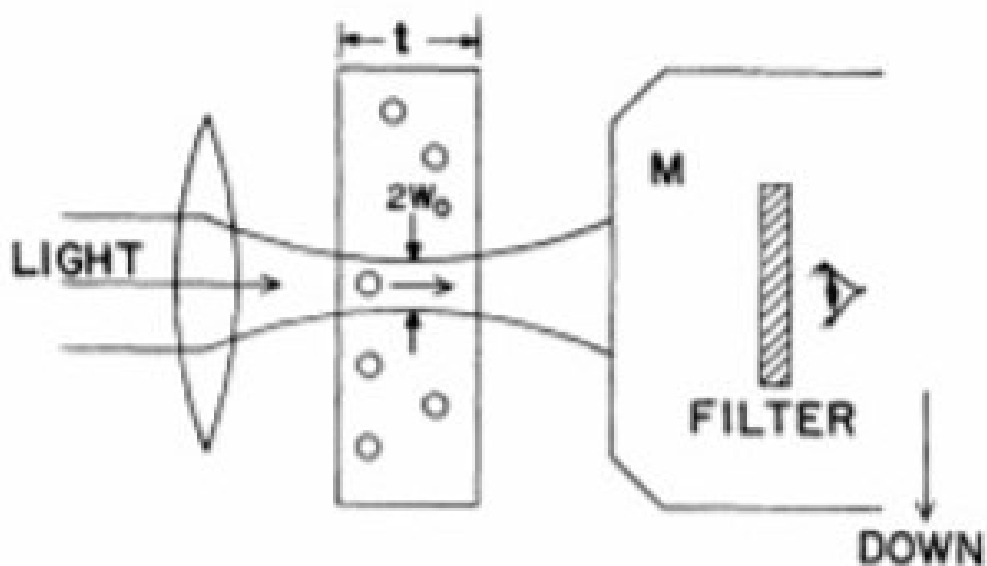


Figure 32: Schematic showing the ability to trap particles using light [19].

Photoinduced aggregation of nanoplasmonic particles is an area with interesting physical mechanisms. Typical techniques of exploring these mechanics requires high power pulsed lasers. This area is novel and is driven by applications in nonlinear optics.

1.8 Statement of Task

In Chapter 2 and 3, studies including the resolution of nanospheres of Au nanoplasmonic structure. Microspheres of high index $n \sim 2$ embedded in an elastomer. The studies were performed on a fluorescent microscope using a 100x NA=1.35 silicone oil objective for fluorescent nanospheres and a 60x NA=1.42 oil objective for F-Actin protein.

In Chapter 4, design, fabrication, and testing of microconical arrays were performed. The design was done using Lumerical FDTD software. The fabrication was done using Nanoscribe nanofabrication tool. The testing was done at AFRL on a short-wave infrared (SWIR) detector.

In Chapter 5, Observations of photo-induced assembly of nanoparticles was studied as a function of nanoparticle size, as a function of the spectral position of the excitation band, and as a function of intensity of photoexcitation.

In Chapter 6, experiments were designed for testing numerical modeling of Prof. Klibanov's algorithms.

CHAPTER 2: QUANTIFICATION OF RESOLUTION OF SLABS WITH EMBEDDED MICROSPHERES FOR IMAGING DIELECTRIC NANOSPHERES

2.1 Introduction

Microspherical nanoscopy (MN) emerged in 2011 as a method of super-resolution imaging based on using dielectric microspheres as contact microlenses [220]. The microsphere is placed in contact with the object and it creates its virtual image few micron below the object plane [23]. The virtual image is magnified (usually by the factor of 3) and formed with participation of the objects optical near-fields. Based on a solid immersion lens concept, an increase of resolution by the factor of n_{sp} , where n_{sp} is the index of the microsphere, can be anticipated.

Compared to advanced fluorescence (FL) superresolution techniques such as stimulated emission depletion (STED) [104] or localization [205] microscopies, the MN technique is extremely simple and versatile method of imaging which does not necessarily require FL labeling. Initially, it was realized for imaging in air [220]. Soon after, the most practical modification [28] of this method based on using high-index (n 1.8) microspheres immersed in a contrast medium was proposed [52, 50]. It made possible imaging of subcellular structures, viruses, and proteins in an aqueous phase which cannot be resolved by conventional microscopies. MN can be combined with the confocal and FL imaging. Scanning of large sample areas can be performed by translating the microspheres by a variety of techniques.

All these developments stimulated accurate quantification of resolution in this method. Initial studies were performed using subwavelength periodic structures such as a Blu-ray disk; however, gradually it was realized that the use of stand-alone objects with recognizable shape provides more reliable resolution quantification. For imaging the nanoplasmonic structures, the resolution at $\lambda/6$ - $\lambda/7$ level was demonstrated [52], where λ is the illumination wavelength. This level exceeds the maximal far field resolution ($\lambda/4$) which can be predicted based on the solid immersion concept for the lens with $n \approx 2$. Theoretically, the incoherent imaging of point-sources was studied by numerical solution of Maxwells equations [173]. It has been demonstrated that coherent illumination or resonant excitation of coupled plasmonic modes allows for increasing the resolution beyond the diffraction limit [38, 172, 173].

Microspherical nanoscopy was further advanced by a recent proposal to combine its large effective numerical aperture with structured illumination provided by nanoplasmonic arrays [86]. In this technique, the objects are placed directly at the top of the nanoplasmonic array and their high spatial frequency information gets, //smearred across frequency space, by the Fourier transform of the excitation pattern similar to the structured illumination microscopy (SIM) [86]. Use of periodic nanoplasmonic array as opposed to an interference pattern allows mixing with higher grating k-vectors. This approach has been initially realized without using microspheres and termed localized plasmonic structured illumination (LPSIM).

In classical SIM the superresolution stems from the multiple (m) images acquired at different phase shifts ($m\phi$). There are as many equations (images) as there are unknowns (information components) that allow finding components by inverting an

m x m matrix that is equivalent to a discrete Fourier transform with respect to the phase-shift variable ϕ . In this regard, all modifications of SIM including blind reconstruction or LPSIM method use postimaging processing.

Our approach is different as it is based on strong coupling of radiation of nanoscale objects to the folded dispersions of the periodic nanoplasmonic array. Such situation is well known for nanoplasmonic arrays and it manifests itself due to directionality of emission and due to the fact that high $k - vectors$ (near-field) of the source are folded into escape cone by the grating k-vectors. In this sense, this mechanism is reminiscent of the far-field superlens with the difference that attenuation of the zero-order waves is not needed since emission is provided in diffraction orders. Neither postimaging processing nor all-optical hardware after superlens such as beam splitters, lenses, and gratings are required in our approach [31].

The utilization of a series of nanoplasmonic arrays with variable periods has been employed for imaging fluorescent (FL) nanospheres. The spectral emission band of both objects matches the localized surface plasmon resonance in the Au plasmonic arrays. It is shown that decreasing a leads to coupling with the increasing array wavevectors,

$$k_{lp} = \frac{2\pi}{a} \tag{25}$$

which can be much larger than the radius of the diffraction-limited optical transmission function

$$k_{em} = 2\pi n_{sp}\lambda \quad (26)$$

It allows realizing $\lambda/7$ resolution of plasmonic dimers far beyond the classical diffraction limit.

2.2 Fabrication of Slabs

We begin with the creation of a rigid structure which has the ability to create a virtual image beneath. These structures have some specific requirements that we are looking for. As stated before Polydimethylsiloxane (PDMS) [11, 13] has been used for embedding spheres and placed on nanoplasmonic structure allowing for the microspheres to be moved in a controllable way. PDMS have some problems with the fact that it takes a very long time for the liquid lubrication layer to evaporate, it also allows for microspheres to float in the elastomer base and hardening agent making some microsphere unusable for super resolution treatment, and it also have problems when using high NA objectives ($NA > 1$). The viscosity of the oil makes moving the sample difficult, as the PDMS shifts slightly due to the oil. We designed a procedure for embedding high index microspheres ($n > 1.8$) into the rigid plastic coverslip.

One caveat to this is the fact that high index BTG microsphere are opaque in the visible regime of the electromagnetic spectrum the opaqueness is explained by two effects: 1) absorption and 2) high reflectivity. The reflectivity can be reduced when an optical index matching agent is added to surround the microsphere. The index matching agent which we chose to use resembles a traditional cover slip, $n \approx 1.5$. We chose this because cover slips do not have a problem when using high NA objectives

such as oil or water objectives. The coverslips with high index microspheres embedded inside of them also allows for the creation of a virtual image plane beneath the object plane, see Figure 33.

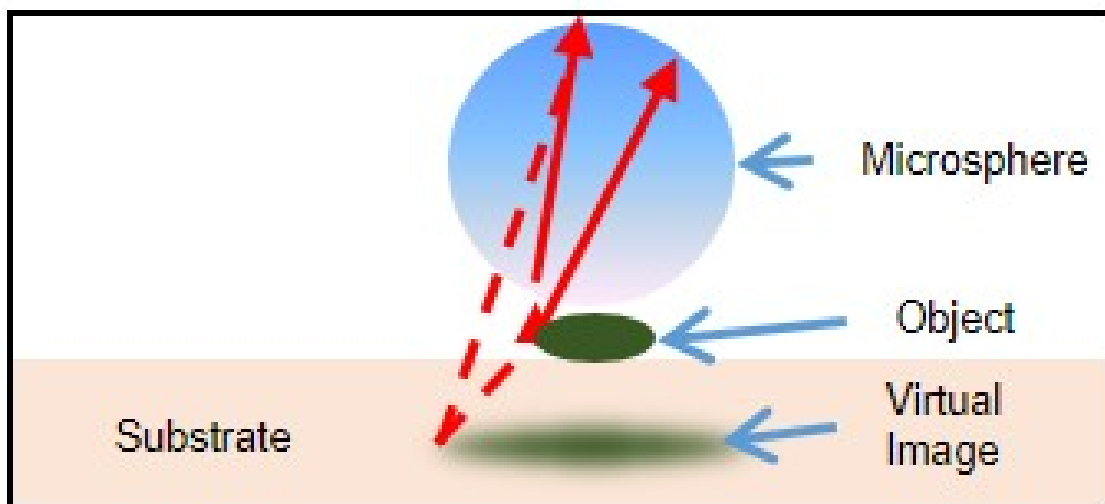


Figure 33: Illustration of the creation of the virtual image by a contact microsphere

This virtual image plane is magnified depending on the index of the slab, n_1 , index of the microsphere, n_{sp} , index of the sample, n_2 , radius of microsphere, r , and the gap between the microsphere and the object g ; see Figure 34 for illustration and Eq. 27 for formula [13].

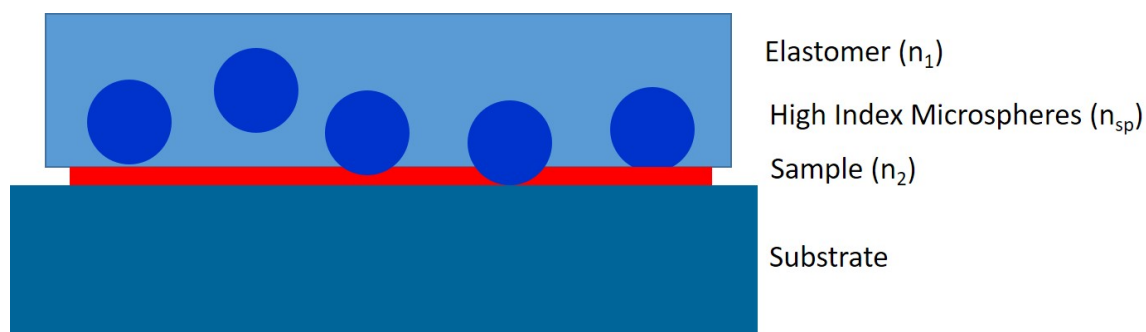


Figure 34: Illustration of the microsphere embedded cover slip with a sample between it and a substrate.

$$M(n_{sp}, n_1, n_2, r, g) = \frac{-n_{sp}n_1}{[n_1(n_{sp} - 2n_2) + (\frac{g}{r})(n_{sp}[n_1 + n_2] - 2n_1n_2)]} \quad (27)$$

A procedure was developed to accomplish the task of embedding high-index BTG microspheres inside of a plastic coverslip. This involves using a thermal press, see Figure 35 (a), two borosilicate glass microscope slides, four borosilicate coverslips (number 0 and number 1), Barium Titanate glass (BTG) microspheres (1 μm -53 μm in diameter), and a cellulose acetate (plastic) coverslip. The process begins with placing a borosilicate glass microscope slide on the bottom plate of the press and placing a plastic coverslip directly on top of the glass microscope slide.

The top of the press is heated to be $\sim 160^\circ\text{C}$ and lowered to be ~ 5 mm above the bottom plate. This configuration is left for 30 min to allow for the plastic to soften. After 30 minutes the top plate is lifted and microsphere are deposited directly onto the softened coverslip and 4 borosilicate coverslips are placed on the edge of the microscope slide. The desired thickness determines which glass coverslip is placed on the edge as spacers. For thinner microsphere embedded coverslips the use of number 0 glass spacer and typical coverslips number 1.

The top of the press is returned to its position to be ~ 5 mm above the bottom plate. This configuration is left to heat the plastic coverslip and it allows gravity to force the BTG produced by Mo-Sci Corp. microspheres into the plastic coverslip, see Figure 35 (b). The BTG spheres have 2 different modifications changing the index of refraction, the first being with a larger content of barium having an index $n_{sp}=1.9$ and the second with a larger content of titanium having an index $n_{sp}=2.1$ at the D_2

Fraunhofer line.

After this time the top plate is moved and a second microscope slide is placed directly on top of the microspheres and the top plate is heated to $\sim 170^{\circ}C$ and is lowered to be in contact with the bottom plate applying light force onto the microspheres. This configuration is left for 60 min. Afterwards the bottom plate is moved up ~ 2 mm and the top plate is forced down applying high force onto the microspheres. This configuration is left at high temperature for 60 minutes. After 60 minutes the heat from the top plate is removed and the configuration is left to sit for 2 hours to allow the system to cool. Afterwards the microsphere embedded coverslip is removed using a metal scalpel and is ready to be used, see Figure 35 (c).

These slabs are fairly robust with the ability to be moved without risk of breaking or tearing of the substance. With PDMS one large problem is removal of the slab and transferability. Oftentimes when removing the slab tearing happens limiting the size of the slab that is usable. The plastic coverslips are not without problems. We have found that the coverslips actually deform greatly in order to allow for larger microspheres to be embedded in the coverslip. This forces the coverslip to be used in an aqueous environment and has to be held in place by micro fluidics. This forces the microsphere to be extremely close to the objects. This small distance is optimal for near field coupling mechanics which can only happen when the object and the lens are separated by gaps $\sim \lambda/2$. With the microspheres protruding outside of the coverslip it is very easy to visualize microspheres that are usable while using high magnifying and/or NA microscope objectives. These microsphere embedded microscope slides are placed directly on the sample, see Figure 36.

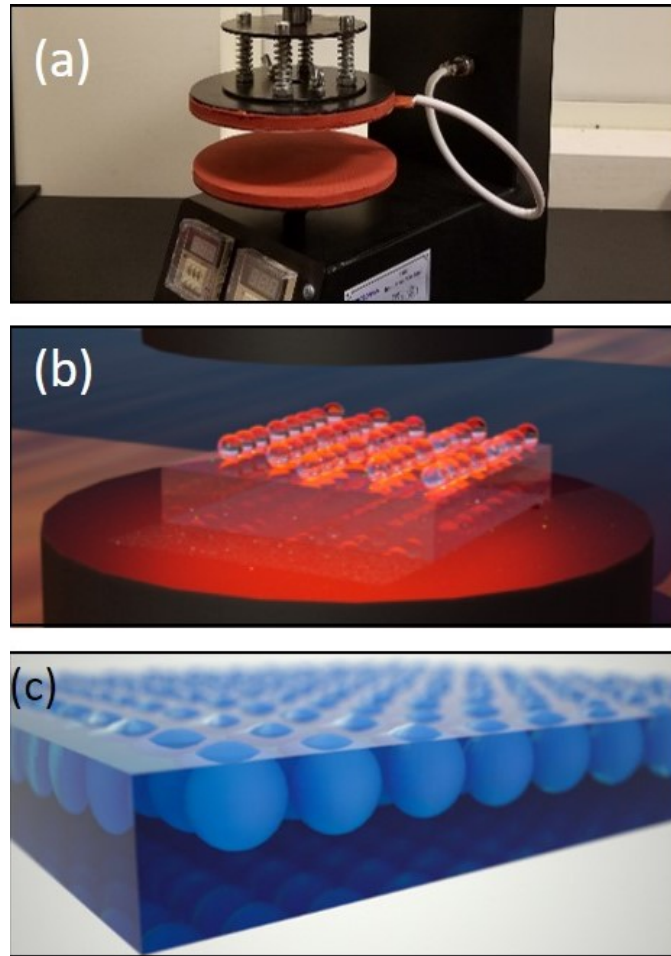


Figure 35: (a) Thermal press that was used to create the rigid coverslips with embedded microspheres. (b) Illustration representation of microspheres sitting on top of a plastic coverslip, which is being heated to allow for the microspheres to be embedded. (c) Illustration representation of the end product after cooling.

2.3 Justification of use of nanospheres

There are certain aspects that one looks for when attempting to quantify the resolution of an optical system. Ideally point sources are used; however, in real practical experimentation it is impossible to have a true point source. Because of this the best object would be something that can be modeled as a point source. A point source will be something that is completely constrained to an infinitesimal size in all three dimensions and when it is projected onto the virtual image plane creates airy

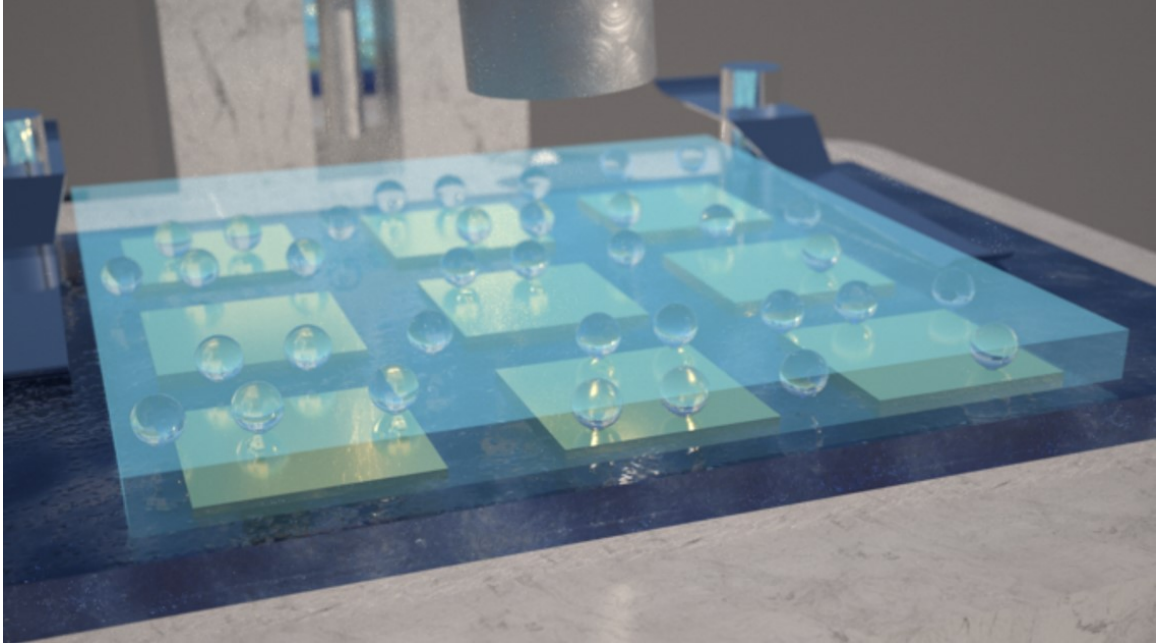


Figure 36: Illustration of microspheres embedded in an elastomer placed on top of a nanoplasmonic structure.

rings on the image plane of the optical system. We have chosen to use dye doped nanospheres. These are dye doped to be excited by a mercury lamp with excitation ~ 480 nm and has an emission at ~ 540 nm. The nanospheres are fabricated to be 47 nm in diameter with a 1% standard deviation from this mean. Because these nanospheres are so small compared to the wavelength of light that is illuminating the sample, they act nearly like a point source. Unfortunately they are in an unknown solution which involves water, surfactant is added in order for the nanosphere to repel each other and the surfactant is unknown to the writer of this dissertation as it is proprietary of the company we purchased the nanospheres from. These nanospheres are dye doped making the signal that is obtainable from the object compared to the background ideal. One problem with unlabeled dielectric materials is the contrast between the object of interest and the surrounding media makes the objects nearly

impossible to resolve.

2.4 Quantification of Resolution

In order to quantify the resolution of the system it is imperative to have a source that we are confident consists of an optically small object, ideally a single nanosphere. To do this the nanospheres were diluted using 10 drops ($\sim 350\mu\text{l}$) with $\sim 1\text{ml}$ of IPA. This mixture was mixed using a Bransom 1510 ultrasonic bath for 30 seconds. From this mixture $3\mu\text{l}$ has been pipetted directly onto a microsphere embedded coverslip, see Figure 37 (a). The sample of interest is then placed and pressed directly onto the microsphere embedded coverslip. This is so gravity will be working in favor of keeping the object close to the microsphere. This sample is then lifted to ensure good contact between the sample and the coverslip, see Figure 37 (b). If the hold is good the sample is used. If the hold is not good, the coverslip is discarded and the sample is cleaned using a solvent rinsed and another attempt is made.

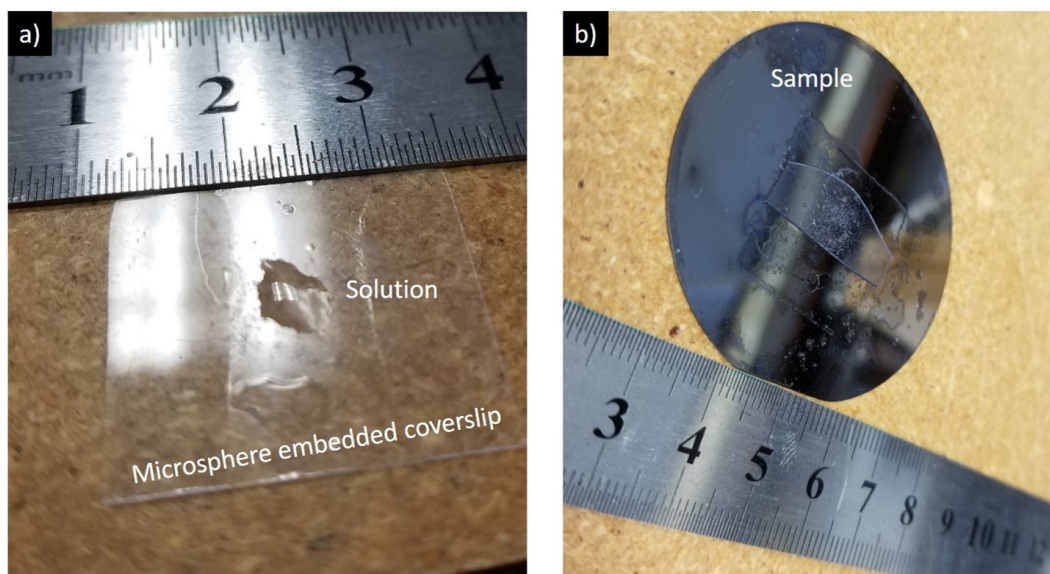


Figure 37: (a) Photo of $3\mu\text{l}$ drop on a microsphere embedded coverslip. (b) Photo of microsphere embedded coverslip secured onto a nanoplasmic sample.

The nanoplasmonic sample was fabricated at the Air Force Research Laboratory in Dayton, Ohio. The process begins with a polished c-plane sapphire wafer which has been solvent cleaned. Afterwards photoresist was spun onto the wafer. A layer of gold was deposited on top of the photoresist creating a conductive surface so the E-beam lithography machine can see the surface and write into the resist. After this process metal deposition occurs, for these samples 3 nm of titanium is deposited onto the sample followed by 17 nm of gold. Finally the excess metal is removed using a tape liftoff process. The process has not been published and is proprietary to the Air Force which is why the type of photoresist used has been omitted along with the thickness it is spun to, the thickness of gold before the E-beam lithography machine (JEOL EBX 6300FS), and the dose concentration of the E-beam lithography machine.

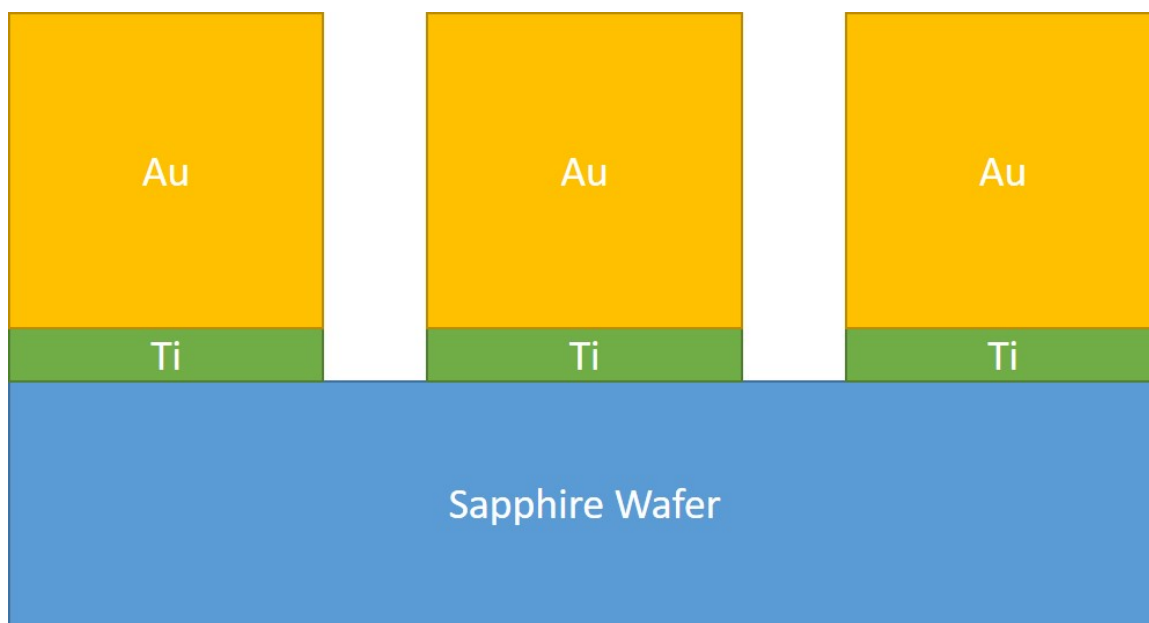


Figure 38: Cross section of nanoplasmonic structure.

A problem with this technique though is the random nature of how the microspheres are distributed around the coverslip and the random nature of deposition of

nanospheres on the sample a single microsphere could not be used in order to investigate all locations of interest. Multiple microsphere were used in gathering data in 8 distinct locations, see Figure 39 (a,b). A comparison between localized surface plasmon resonance (LSPR) and surface plasmon resonance (SPR) was of personal interest. These locations allow for a direct comparison between these two phenomena. The cylinders constrain the oscillations in three dimensions whereas the stripes only constrain in two dimensions, assuming the oscillation are constrained due to the thickness and does not bleed into the wafer. A representation of a typical grid is shown in Figure 39 (c,d). The size of the pillar or stripe stays static; however, the center to center distance is changed. The resulting resolution is depicted in Figure 39 (e).

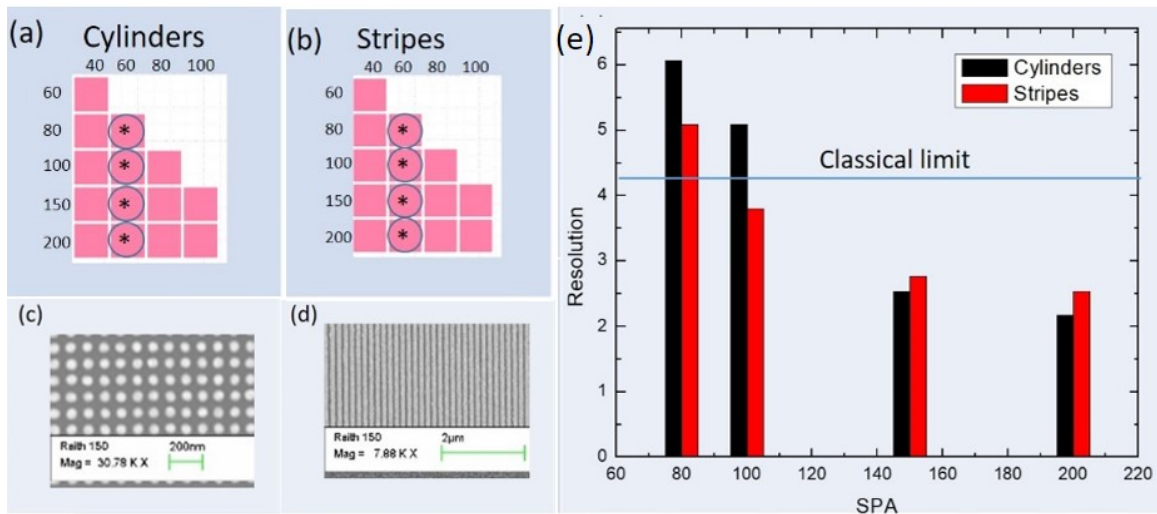


Figure 39: (a) Map of nanoplasmonic cylinders which are fabricated using an E-beam lithography machine. (b) Map of nanoplasmonic stripes which are fabricated using an E-beam lithography machine. (c) Representation of a typical cylinder after fabrication. (d) Representation of typical stripe after fabrication. (e) Resolution quantification of different structures with a relation to the classical limit.

The experiment was done using an Olympus IX71 inverted microscope utilizing

a 100x silicone oil immersed objective with NA=1.35. The quantification was done using the raw image obtained from the microscope. There are other groups doing similar work [34]; however, all other groups have some post-processing technique that they use in order to boost their resolution claims. Whereas with our process we take the image directly from the microscope and do our analysis on it.

In this dissertation work we have developed a Matlab code that does this process; however, the process is somewhat complex and will be described in detail here prior to the code being written. The first thing that was done was the microscope objective was calibrated. This calibration standard was used in the program Tracker and a line profile was obtained of the object of interest. The position with relative intensity values were imported into the program Origin and a Gaussian is fit to the curve according the parameters in Origin for fitting a Gaussian. The coefficient of determination, R^2 must be above 0.990 for a fit to be considered usable. The FWHM of this fitted Gaussian curve is then determined and that is the resolution of the image as per the Houston criterion. Multiple different nanospheres were used to quantify the resolution of the optical system itself.

2.5 Conclusions

New technology of embedding high-index BTG microspheres into a plastic slab has been developed. The technological processes is based on softening the slab by controllably heating the plastic near the softening point followed by pressing the microspheres into the plastic; similar to an embossing process. It is shown that plastic slabs have some advantages over PDMS-embedding technology used in the

previous studies. These advantages are related to achieving minimal gaps between the spheres and objects in the case of liquid samples.

Nanoplasmonic square arrays of Au nanodisks and nanostripes were fabricated with a broad range of geometrical parameters such as the characteristic dimensions and periods to provide efficient structured illumination of various objects placed directly at the surface of such arrays.

Dye-doped FL polystyrene nanospheres with the emission band matching the spectral position of the emission band of localized surface plasmon resonances in nanostructured metallic arrays were selected as objects for imaging and resolution analysis.

The interpretation of the observed effect is proposed based on strong coupling of the objects emission to the band structure formed by coupled LSPRs in Au nanodisks. An increased coupling to plasmonic band structures was observed previously [34] and it manifests itself due to directionality of the emission. Thus, the mechanism of the observed effects reminds the principles of Localized Plasmonic SIM (LPSIM) [34] and optical superlens [69]; however, in our case we show that the super-resolution can be achieved without postimaging processing and without additional optical components.

CHAPTER 3: QUANTIFICATION OF RESOLUTION OF SLABS WITH EMBEDDED MICROSPHERES FOR IMAGING BIOMEDICAL OBJECTS

3.1 Introduction

For thousands of years people have looked at objects for a better understanding of the universe around them. This understanding escalated drastically with the invention of the optical microscope. The utilization of optical electromagnetic radiation is used to see objects that are invisible to the naked eye. However, this is still limited by the diffraction nature of light. The limit is:

$$\varepsilon = \frac{\lambda}{2n_{object}\sin(\theta)} \quad (28)$$

This limit is known as the classical diffraction limit or Abbe diffraction limit. This was proven by Helmholtz after Ernst Abbe theorized that in an aberration free optical system the discernibility of two object is still limited. For many areas this limit has become a barrier to improving an understanding of many different research areas. There have been a few creative methods to circumvent this limitation with the most famous being stimulated emission depletion (STED), which received the Nobel Prize in Chemistry in 2014. Other methods include structured illumination microscopy (SIM), stochastic optical reconstruction microscopy (STORM), hyperlens, photo-activated localized microscopy (PALM), far-field superlens (FSL), low-index contact microlens, high-index contact microlens, and most recently localized plasmon

structured illumination microscopy (LPSIM).

All of these methods have tradeoffs between several factors such as resolution, speed, field of view, biocompatibility, sensitivity, and experimental complexity. The ideal situation will allow for very high resolution, such as STORM, but with the ability to capture images in real time, such as with high-index contact microlens. Recently, SIM has introduced plasmonics PSIM in the schematic to further improve the resolution of the system past the ~ 2 times enhancement from traditional SIM. This is because plasmonics have a grating has a very large separation in K space allowing for much finer features to be resolved. This means that it is very simple to use a commercial objective along with a coupling dielectric microsphere to investigate the surface of a structure. The mechanism behind this coupling is still debated in literature it is still widely believed that the use of high index contact microspheres increases the total effective NA of the optical system leading to an improved resolution. In this paper we report the resolution approaching $\lambda/7$ when finding the resolution of fluorescent dye doped biological objects. In doing this a virtual image is created beneath the object. This virtual image is magnified as defined by Eq. 29.

$$M(n', r, g) = \frac{-n'}{[2(n' - 1)(\frac{g}{r} + 1) - n']} \quad (29)$$

where M is the magnification due to the microsphere, n' is the index of refraction contrast of the object space and the medium surrounding the microsphere, r is the radius of the microsphere, and g is the gap between the microsphere and the object of interest. When taking into consideration this magnification of contact microsphere

microscopy it is clear that a better resolution is achieved than non-microspherical microscopy, see Figure 40.

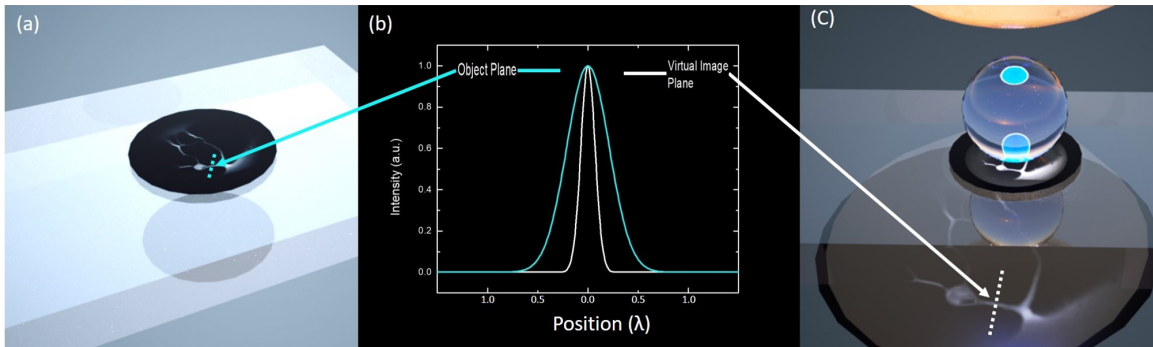


Figure 40: (a) Illustration of object taken with no microsphere. (b) Graphical illustration showing the Gaussian fit of objects on the object plane and the virtual image plane. (c) Illustration of a typical contact microsphere experimental set up.

3.2 F-Actin Fabrication

The biggest problem with biological samples are the non-reproducibility of the object, each sample will be slightly different than the last. All biological objects are unique making it impossible to have a standard object as a model. We decided to use well known filament Actin (F-Actin) and prepare due to its property of being confined in two dimensions, on the orders of a few nanometers, in the radial direction and on the order of several microns in the axial direction. Actin was prepared from rabbit back and leg muscles as described in [210]. F-actin was labeled with Alexa 555, cleaned from the excess label, re-polymerized, stabilized with phalloidin at a molar ratio of 1:1, and dialyzed for two days at $T=4C$ against the experimental buffer (20 mM MOPS (3-N-morpholino]propanesulfonic acid) pH 7.5, 50 mM KCl, 3mM $MgCl_2$). F-actin was diluted to a concentration of $0.5 \mu M$.

3.3 Experimental Results

The experimental sample was prepared in three distinct ways: first one being F-Actin on a coverslip with no nanoplasmonic structure and no microsphere above, see Figure 41 (a), second one being on a coverslip with no nanoplasmonic structure below and a microsphere above the F-Actin sample, see Figure 41 (b), and lastly being on a coverslip with a nanoplasmonic structure below and a microsphere above the F-Actin sample, see Figure 41 (c). The first (1) way is a traditional microscopy schematic, the second (2) way is considered to be microspherical assisted microscopy, and the third (3) way is plasmonic enhance microspherical assisted microscopy. The first two methods are used as a check to confirm that what we do does not break the Abbe limit for microscopy to give us more confidence in our results.

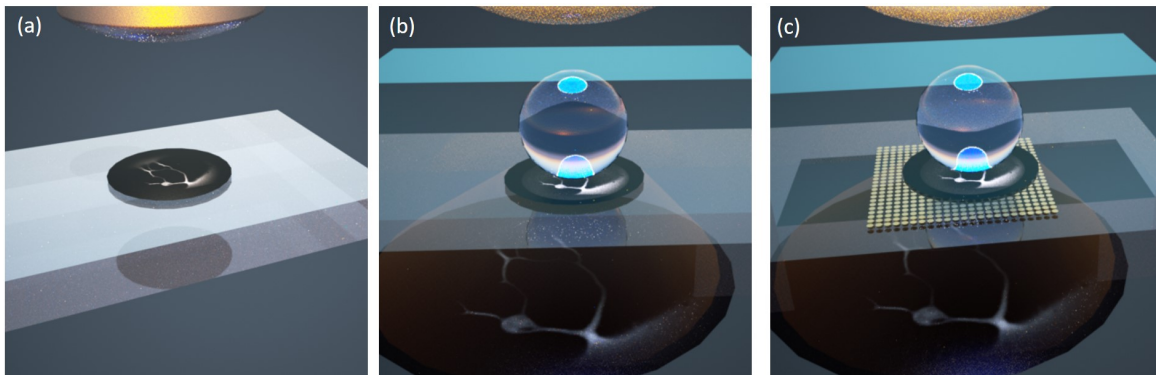


Figure 41: (a) Illustration of object taken with no microsphere and no nanoplasmonic array beneath the object. (b) Illustration of object taken with high index microsphere embedded in an elastomer and no nanoplasmonic array beneath the object. (c) Illustration of object taken with high index microsphere embedded in an elastomer and a nanoplasmonic array beneath the object.

The F-Actin was prepared in a similar manner as the nanospheres in the previous chapter. Some changes include the $0.5 \mu\text{M}$ solution of F-Actin was not placed in an ultrasonic bath, mixture was done using a pipette. Afterwards $3 \mu\text{l}$ of solution was

deposited directly onto a coverslip with embedded microsphere and the nanoplasmonic structure was placed and pressed into the microsphere embedded coverslip, excess liquid was gathered by a Kimwipe. Observation methods (1) and (2) from above were tested on two distinct microscope systems.

The first microscope system was an Olympus IX71 wide-field microscope utilizing a 40x (NA=0.60) air objective. This microscope used an HBO 100W / 2 short-art discharge mercury lamp with a mCherry filter. The mCherry filter allowed for excitation 542-582 nm with an emission wavelength of 607-683 nm. Resolution quantification was done at both the object plane and the virtual image plane, see Figure 42.

The second microscope system was Olympus SD-OSR confocal microscope utilizing a 60x (NA=1.35) silicone oil immersion objective. This microscope used illumination from a laser source operating at a wavelength $\lambda=461$ nm with a Texas Red filter. The Texas Red filter allows for the 461 nm laser to excite the Alexa-555 fluorophore and has an emission wavelength of 606-644 nm. Resolution quantification was done at both the object plane and virtual image plane, see Figure 43.

The third microscope system was Deltavision OMX SR wide-field microscope utilizing a 60x (NA=1.42) oil immersion objective. This microscope used illumination from a laser source operating at a wavelength $\lambda=525$ nm with a Texas Red filter. The Texas Red filter allows for the 525 nm laser to excite the Alexa-555 fluorophore and has an emission wavelength of 604-644 nm. Resolution analysis was done at both the object plane and virtual image plane, under two different conditions. The two conditions are with the nanoplasmonic structure beneath the object and with the

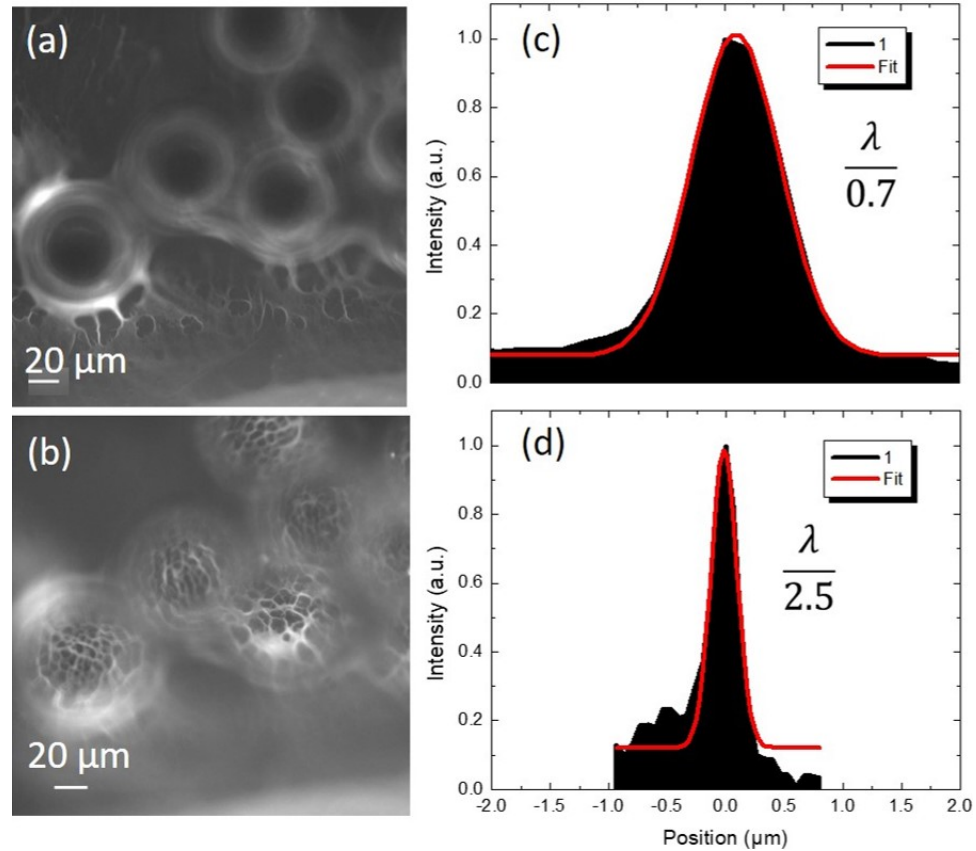


Figure 42: (a) Microscope image of the object plane showing Actin filaments along with microspheres. (b) Microscope image of the virtual image plane showing much finer details of the Actin filaments. (c) Resolution analysis of a typical Actin sample on the object plane. (d) Resolution analysis of a typical Actin sample on the virtual image plane.

nanoplasmonic structure absent from beneath the object, see Figure 45.

3.4 Conclusions

It is demonstrated that the F-actin protein filaments represent a convenient biological model system for the resolution quantification due to the nanoscale width of individual filaments and the micron-scale length. It is clear that the use of nanoplasmonic arrays have an enhancement in resolution over conventional and solid immersion microscopy. Without using nanoplasmonic arrays, the experimental resolution approaches the solid immersion lens limit $\sim \lambda/2n_{sp}$. Use of the sufficiently short-period

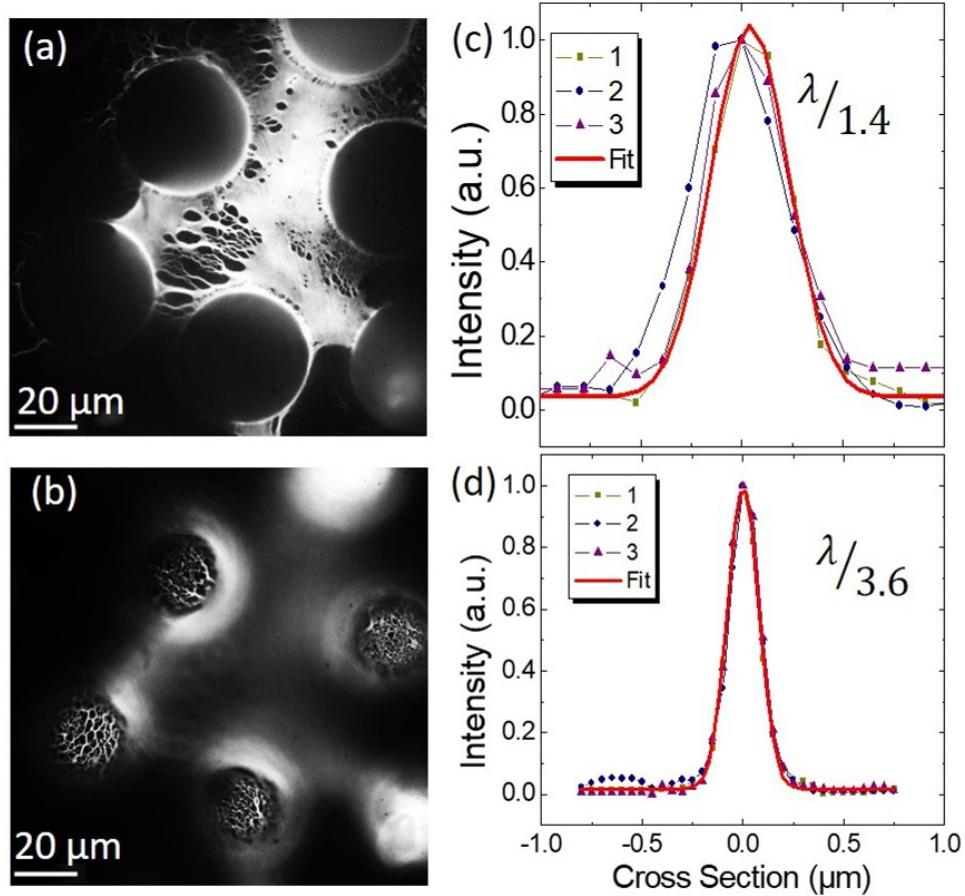


Figure 43: (a) Microscope image of the object plane showing Actin filaments along with microspheres. (b) Microscope image of the virtual image plane showing much finer details of the Actin filaments. (c) Resolution analysis of a typical Actin sample on the object plane. (d) Resolution analysis of a typical Actin sample on the virtual image plane.

nanoplasmonic arrays allows for further increasing resolution beyond the diffraction limit due to smearing of the high spatial frequency information across the frequency space. This increase is only seen when the nanoplasmonic array details are structured so that the k -vectors do not overlap. A specific feature of our method is that it does not require any post-imaging processing which is required by SIM, LPSIM, etc.

We experimentally show that additional optical elements of the far-field super-lenses required for attenuating the zero-order beams, amplifying the evanescent waves

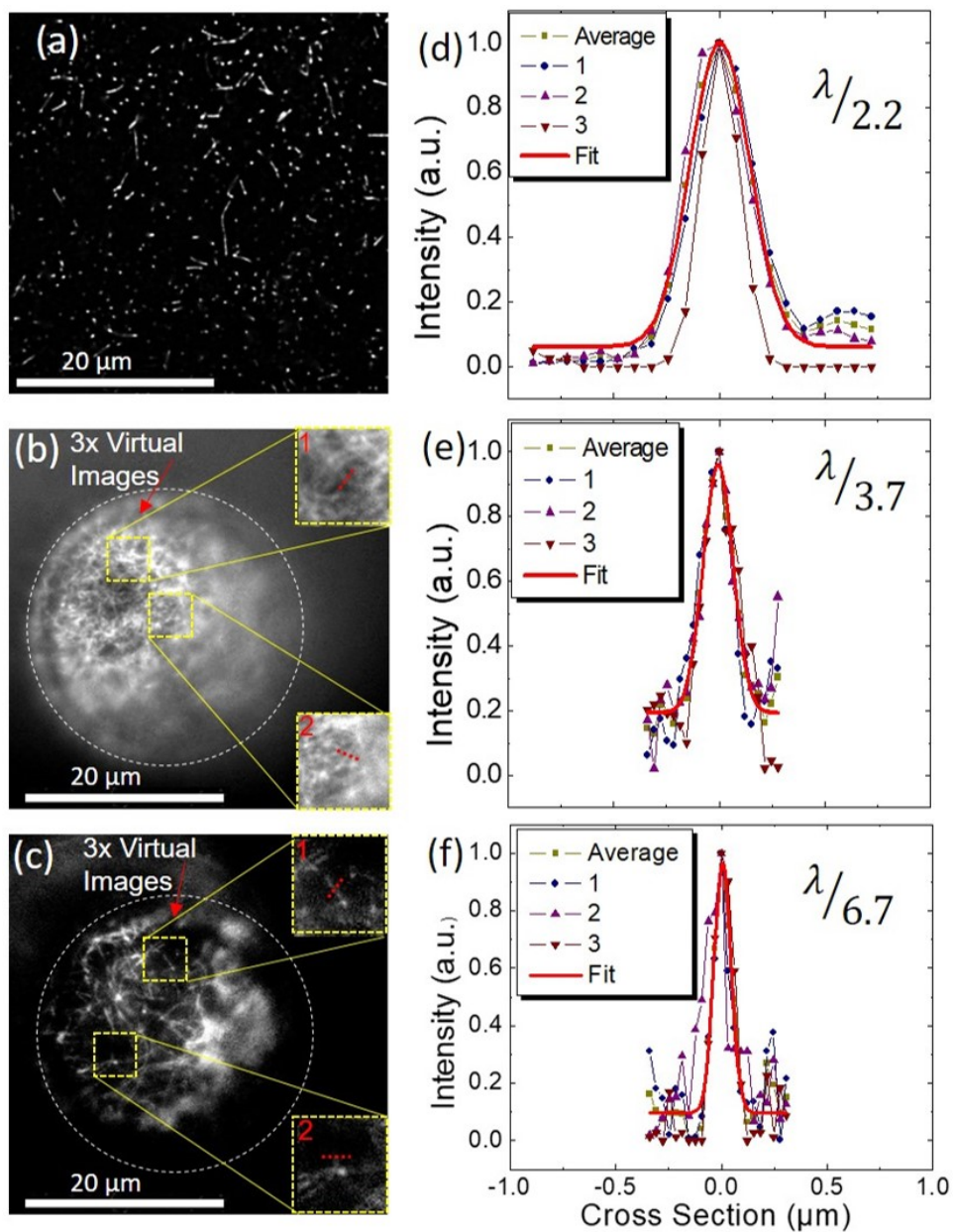


Figure 44: (a) Microscope image of the object plane showing Actin filaments along with microspheres. (b) Microscope image of the virtual image plane showing much finer details of the Actin filaments. (c) Resolution analysis of a typical Actin sample on the object plane. (d) Resolution analysis of a typical Actin sample on the virtual image plane.

and converting evanescent into propagating fields are not required in our approach. The likely explanation is related to the fact that the nanoplasmonic array located at nearly contact conditions with the object totally redirected the radiation into states coupled with folded dispersions of localized surface plasmon resonances. Under these conditions the Moire' effect transferring information from higher spatical frequencies into the escape cone becomes very pronounced and higher spatial frequencies can be accessed by focusing at the narrowest waist of the point-like objects.

The proposed method allows increasing the resolution of standard microscopy by a factor of 3 that allows biomedical imaging of subcellular structures, proteins, and viruses without sacrificing the simplicity and speed of the optical characterization.

CHAPTER 4: ENHANCEMENT OF MID-WAVE IR FOCAL PLANE ARRAY BY INTEGRATION WITH DIELECTRIC MICROSPHERE- AND MICROCONE-ARRAYS

4.1 Introduction

The reduction of dark current and, consequently, to increase the operation temperature of midwave infrared (MWIR) and long wave infrared (LWIR) detectors is the concept of this chapter. Typically MWIR and LWIR photodetectors are cryogenically cooled and switching to thermoelectrically coolers is a big and, potentially, industry-impacting task. Our approach to this problem is based on reducing the area of the detectors; however, just reducing the area would lead to a negative consequence of losing the signal along with the reduction of the dark current. So, our concept is to build the light-concentrating microstructure which would allow us to keep very high photon collection efficiency and to combine it with small photodetector currents. There are two distinct approaches based on two different optical principles for concentrating light: 1) focusing of light by microspheres and 2) waveguiding by tapered waveguides in microconical structures.

Previous work [6] experimentally realized the enhancement of midwave infrared (MWIR) photodetectors. This was done using a microsphere and allowing the generation of a photonic nanojet to enhance the photocurrent generated by the detector. The positioning of sapphire ($n=1.71$), polystyrene ($n=1.56$), and soda lime glass

($n=1.47$) microspheres were placed on top of MWIR photodetector mesa. This structure was then illuminated at wavelengths $\lambda=2 \mu\text{m}$ to $\lambda=5 \mu\text{m}$. The size of these microspheres ranged between 20λ - 150λ . More work has been done [3] on creating an array of microspheres for enhancing an entire array, instead of just a single element.

The infrared photodetector they used is an nBn structure grown on GaSb substrate with InAs/InAsSb type-II super lattice structure (SLS) as the material for the active region. The mesas were circular mesa detectors with a diameter of $\sim 35 \mu\text{m}$ fabricated using wet chemical etching and standard metallization for the contacts.

The positioning of the microsphere was done using an F570 Mitutoyo Microscope for observation, and a tapered metallic probe for moving the microsphere. Alignment of the microsphere and mesa is determined by the virtual image of the mesa created by the microsphere; once the image is not distorted and centered the glue is solidified.

The experiment in [6] was conducted at 80 K. Measurements of the photocurrent was taken prior to integration of the microsphere as well as after integration to measure the enhancement of the microsphere. The highest response came from a $300 \mu\text{m}$ sapphire microsphere. This is the largest diameter microsphere used. Initial conclusions made were the larger spheres allowed for more light to be collect thus increasing the photocurrent of the detector; however, this conclusion is incorrect as a $200 \mu\text{m}$ sapphire sphere and a $300 \mu\text{m}$ soda lime glass sphere were also experimentally tested. The $200 \mu\text{m}$ sapphire microsphere outperformed the $300 \mu\text{m}$ soda lime glass.

This lead to finite-difference time domain (FDTD) simulations of sapphire and polystyrene microspheres, in order to explain the experimental results. These simulations used a monochromatic illumination at $2 \mu\text{m}$ and $5 \mu\text{m}$ wavelength with a

computational box of $475 \mu\text{m} \times 475 \mu\text{m}$ 2D box with a computational grid of $\lambda/24$. These simulations gave valuable insight as to the decrease in experimental photocurrent. This decrease was ultimately attributed to the defocusing of the photonic nanojet causing part of it to be blocked by the contact structures, for the sapphire microspheres. For the polystyrene they noticed that due to the low refractive index the focusing was beyond the active region of the detector. This led to the conclusion that there is a great dependence on the refractive index of the sphere.

4.2 Assembly of Microspherical Arrays

We know that a single microsphere can enhance a pixel of a FPA. Real FPAs have multiple pixels making the creation of an array of microspheres necessary. This could be done one microsphere at a time; however, practically will never be done on larger arrays. The concept of using forced assembly to create this array can be seen in Figure 45. Each misaligned or missing microsphere creates a "*broken*" pixel. These pixels may still be functional pixels, they are just unenhanced pixels. Only a small concentration of defects, typically less than $\sim 0.1\%$, can be tolerated in these FPA structures. The high-quality thermographic cameras have the array-size of 1280×1024 pixels, while less expensive cameras with an array size of 160×120 or 320×240 pixels are still in use. This means that the self-assembly techniques cannot be used for such integration because their typical defect rates are several percent [223, 182]. Recently, we proposed suction assembly of microspheres in microhole arrays as a technique which can potentially reduce the defect rates [25, 4].

Microhole arrays with a small number of holes can be fabricated by the mechan-

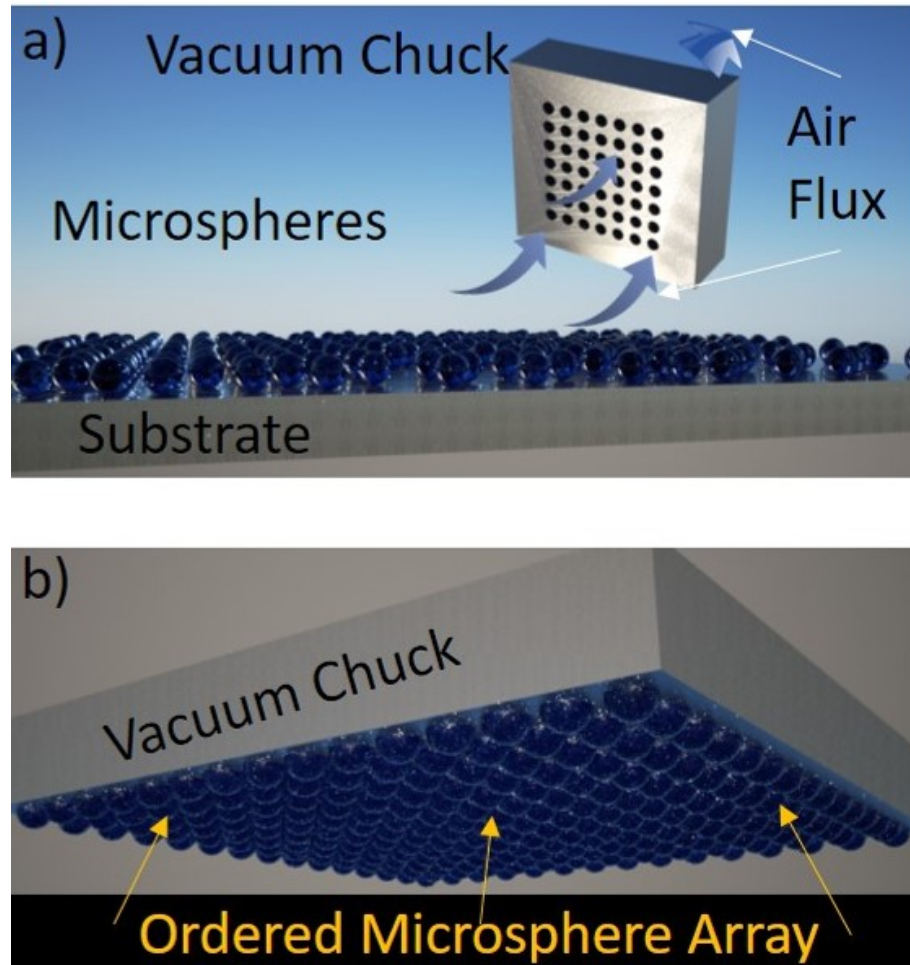


Figure 45: Schematic sketches illustrating steps of assembling microspheres by a suction force causing forced assembly: (a) lifting microspheres from the substrate by a suction force (b) perfectly ordered single monolayer of microspheres. These microspheres are held in place by micro channels which have been fabricated by etching entirely through a lapped down silicone wafer.

ical drilling [4], see Figure 46. This shows an 8×8 microhole array, each microhole is $250 \mu\text{m}$ in diameter and is fabricated in a $500 \mu\text{m}$ thick aluminum sieve. This was constructed by using a lathe with a $250 \mu\text{m}$ drill bit to mechanically drill through the aluminum piece. Microspheres are forcefully assembled in each microchannel through a suction force. The microspheres are $300 \mu\text{m}$ diameter with a pitch of $750 \mu\text{m}$. There was a single microsphere in a single microchannel with a 100% fill factor allowing for

each pixel to have a single microsphere after transferring, as well as no interstitial spheres to spoil the transfer.

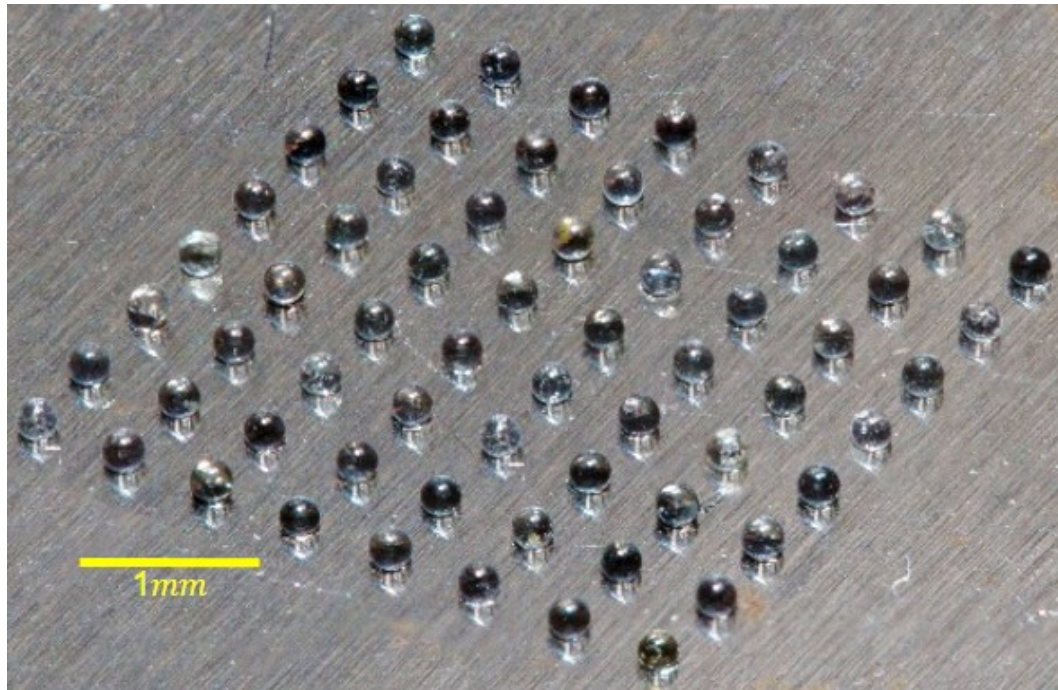


Figure 46: Picture of 8×8 micro-hole array fabricated in a $500 \mu\text{m}$ thick aluminum sieve. The microspheres are $300 \mu\text{m}$ diameter with a pitch of $750 \mu\text{m}$.

With the proof of concept done, the next step was the fabrication of larger-scale microhole arrays. This was achieved by photolithographic methods followed by etching techniques [41]. The process begins with lapping down a silicon wafer to have a $180 \mu\text{m}$ thickness. Afterwards, the wafer was cleaned using a solvent cleaning followed by a pre-bake at 60°C for 3 min. SU-8 2008 was then used to spin coat the wafer. A photomask is used to expose the resist using a Karl Suss MJB-3 mask aligner and the resist is developed using SU-8 developer. This developed wafer is then etched using dry reactive ion etching (DRIE) techniques. The DRIE is applied for 87 minutes etching at $\sim 2 \mu\text{m}$ per minute. The wafer is then turned over and etched for 5 minutes. This leaves the wafer to be $\sim 170 \mu\text{m}$ thick with straight sidewalls

through the entire silicon wafer for the microchannels, see Figure 47. The photomask that was used has 256×256 , $45 \mu\text{m}$ octagons holes with a $60 \mu\text{m}$ pitch. This allows for the use $53 \mu\text{m}$ microspheres to sit in individual channels of the sieve, see Figure 47 (a). The reason for flipping the wafer over is to ensure straight sidewalls for the microchannels and to fully etch each hole to allow for complete suction, see Figure 47 (b).

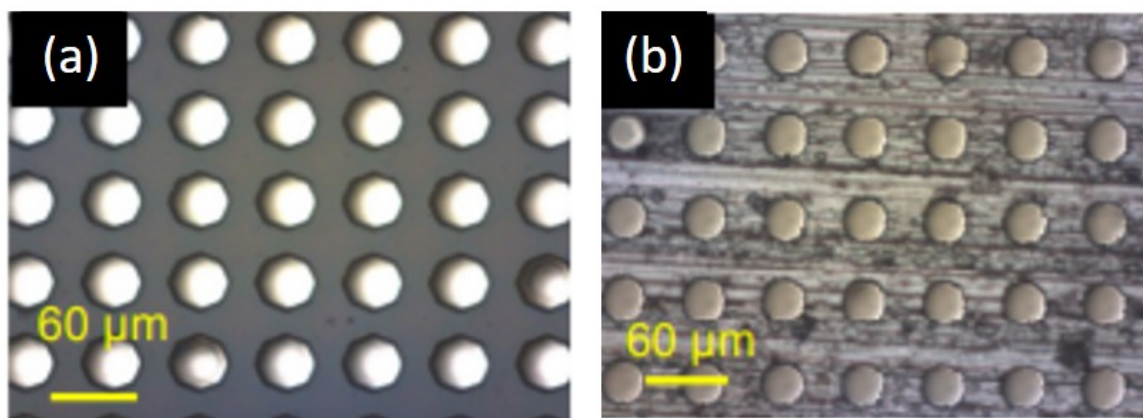


Figure 47: Picture of part of the 256×256 micro-hole array fabricated in a $170 \mu\text{m}$ thick silicon sieve, (a) Front side (b) Back side. This is designed to hold a monolayer of $53 \mu\text{m}$ microspheres.

This had to be scaled to be a larger array of $53 \mu\text{m}$ microspheres. Doing a similar procedure as in Figure 46, the larger 256×256 array showed local defects and showed the inability to create a perfect array of microspheres, see Figure 48 (a). Even though with this forced suction action used, the array has a typical defect rate of $\sim 1\%$. The straight edges of the array clearly visible in Figure 48 (b) prove that it is formed by means of forced assembly. This also shows that there is a single microsphere in each underlying microhole channel. Obtaining such straight edges would be rather difficult in methods of directed self-assembly of microspheres. It is also seen that microspheres are assembled as a single monolayer with no interstitial spheres for most of the array.

This is due to the additional sideway air flux applied to the microhole array while suction is still applied. The reduction of the defect rate below 0.1% might be possible by further advancing the proposed method.

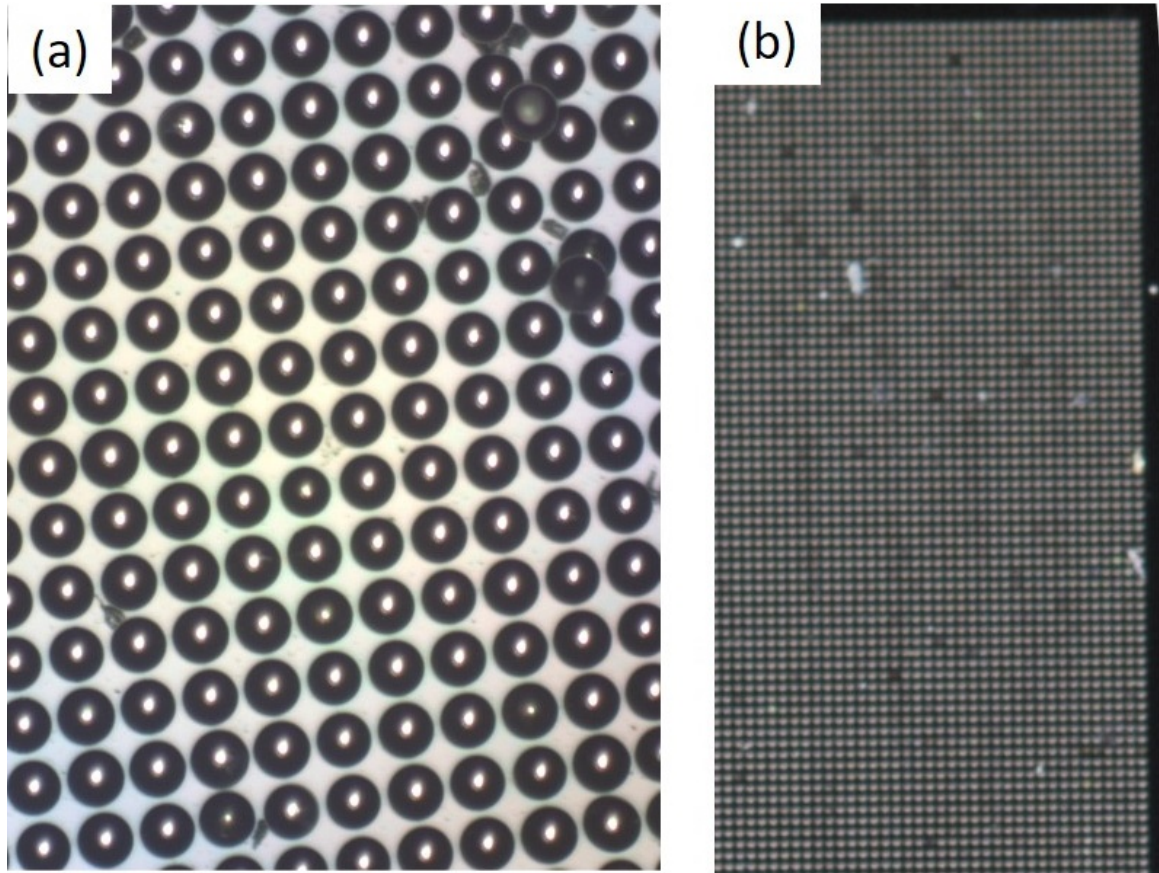


Figure 48: Picture of part of the 256×256 micro-hole array fabricated in a $170 \mu\text{m}$ thick silicon sieve, (a) Front side (b) Back side. This is designed to hold a monolayer of $53 \mu\text{m}$ microspheres.

The proposed technology of forced assembly of microspheres has advantages and disadvantages compared to standard fabrication technologies. The advantage can be seen in a fact that once the array of microholes is fabricated, it can be used multiple times for assembling and transferring arrays of microspheres from the suction chuck to the surface of FPA. In this sense, a single master microhole array can be used for fabricating hundreds of FPAs integrated with microspheres. A disadvantage comes

with the material of the master. Silicon is very brittle when lapped down to such a thin layer. When applying an air flux through the vacuum chuck, there is a risk of shearing this master as silicon is very brittle. It should be noted that the creation of this master is not trivial making it fairly inconvenient to break. In order to have the best transfer, there can be no interstitial spheres. We noticed that the additional air flux required to remove the interstitial spheres sometimes would remove the spheres in the microchannel hole. The electrostatic attraction between microspheres had to be dealt with; however, this is a very complicated process. Ultimately, the use of an NaCl and methanol solution while the microspheres were being sonicated in a dish, was utilized. After the microspheres were forced onto the vacuum chuck, and while the side air flux was being applied, deionized water was applied to the array. This gave the best results of $\sim 1\%$ defect rate.

There are still several problems that have not been resolved. These include the transferability and alignment of the microsphere array with the FPA of interest. We have attempted using a mask alignment tool in order to have the microspheres transferred onto the FPA using the virtual image to as alignment. This method has promise for working, as long as there are no interstitial spheres present. When interstitial spheres are present, when the vacuum chuck and the FPA come into contact with each other, the interstitial sphere causes the array to not be transfer to the FPA. When the chuck is removed from the FPA, the array of microspheres are distorted and no longer usable making it so the array has to be reformed from the beginning. Intense care was taken in order to ensure a single monolayer of microspheres were transferred, $\sim 25\%$ defect rate, of polystyrene microsphere were attempted and

heated. The optical surface of the melted microsphere made them unusable for future studies. We moved past the microsphere array into something new; microcones. The initial studies compared the enhancement of the microsphere to the enhancement of a microcone, see Figure 49. Figure 49 compares a $60\ \mu\text{m}$ diameter microsphere and a tapered microcone that goes from a $60\ \mu\text{m}$ top down to the size of the mesa. Figure 49 (c) compares the sphere and the pillar when it is a $2\ \mu\text{m}$ mesa and Figure 49 (d) is a $7\ \mu\text{m}$ mesa.

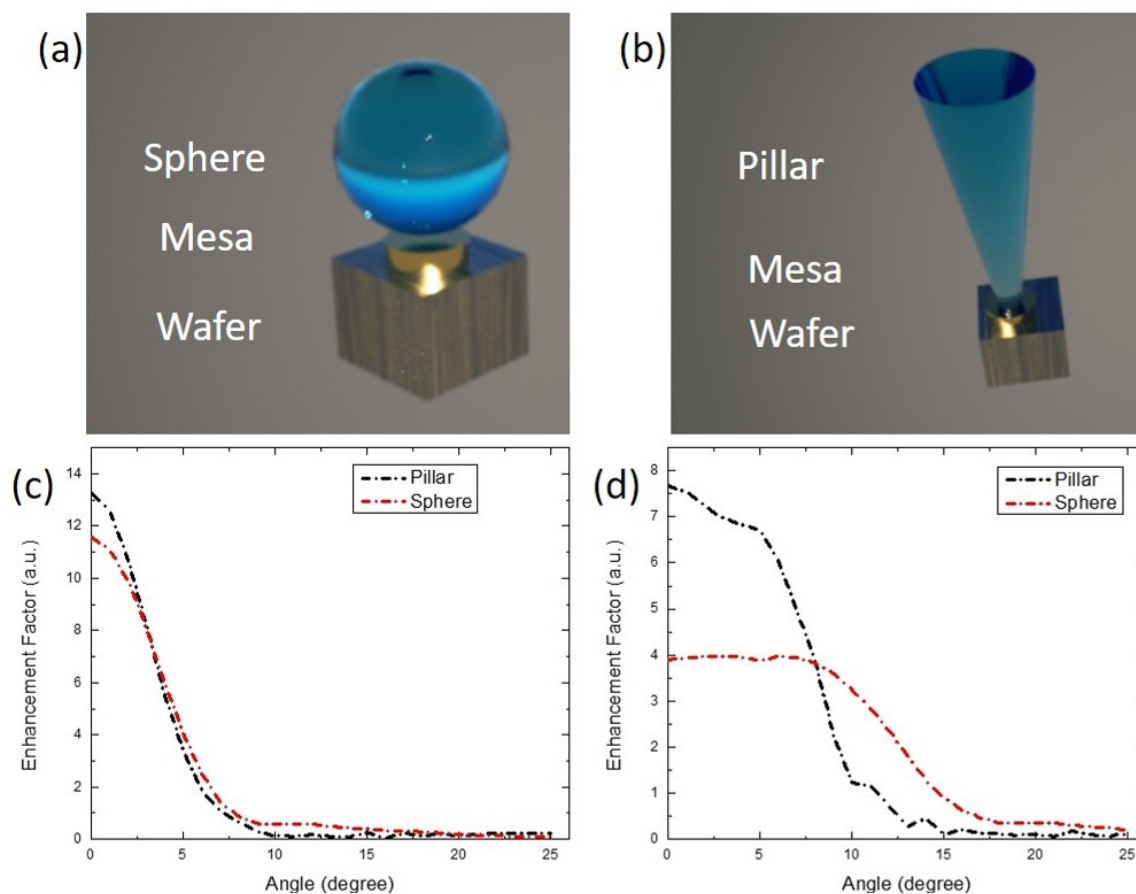


Figure 49: (a) Illustration of a microsphere positioned on top of a mesa (b) Illustration of a microcone positioned on top of a mesa. (c) Comparison of a microsphere and microcone enhancement factor as a function of angle for a $2\ \mu\text{m}$ mesa. (d) Comparison of a microsphere and microcone enhancement factor as a function of angle for a $7\ \mu\text{m}$ mesa.

4.3 Enhancement by Microcone Arrays

We modeled light concentrators formed by microcones which operate as tapered waveguides based on total internal reflection, as opposed to refractive microlenses or microspheres. We used simplified two-dimensional (2-D) numerical modeling to show high collection efficiency of photons with large angle of view provided by such arrays. We modeled such structures using finite difference time domain (FDTD) calculations performed by the Lumerical software at $\lambda=4 \mu\text{m}$ for a 2-D model. It preserves essential properties of the 3-D geometry.

It is clear from Figure 49, that at normal incidence, as well at small angles, the enhancement factor is greater for the pillar over the enhancement factor of the sphere. This is true for both small mesa, see Figure 49 (c), and for large mesa, see Figure 49 (d). This enhancement factor is a ratio between the detected signal with a structure directly fabricated onto the mesa of a FPA, and the detected signal of a bare mesa without a structure directly fabricated on top of the mesa. The idea is to use a structure such as a sphere or pillar to collect more light and guide it down directly to the mesa. The advantage of microcones is determined by their aspect ratio of their top face to the base, the pitch over the mesa size. This agrees with the geometrical limit. It is also great, as the dark current is proportional to the area of the detector, or in this case the length. One aspect that this does not take into account is the actual detected signal of the detector. The detected signal is also proportional to the length of the mesa as well, up to a point, see Figure 50.

Figure 50 shows a theoretical dark current that is normalized to the highest

dark current for the mesa sizes chosen. The mesa sizes that are considered are 1 μm , 2 μm , 4 μm , 7 μm , and 15 μm in length. The dark current is part of the overall noise of the detector and is proportional to the area of the active region of the detector itself. It is clear from the figure that a 1 μm detector has a fair superior dark current or noise over a 15 μm detector. Doing this comes with its own problems though, as the detected signal of the mesa is proportional to the size. In Figure 50, the detected signal decreases as the size of the mesa decreases linearly; however, the detected signal of 15 μm detector does not follow the linear trend and is much higher. The conclusion is that the detector becomes saturated when there is a micropillar fabricated directly onto the mesa. Another problem of the small mesa sizes is the fabrication of the pillars on top of the detector. The photoresist has adhesion issues the smaller the contact area is.

It needs to be stated that for the fabrication attempts we used real simulated data simulated using finite-difference time domain software package Lumerical. This was done using 450 μm tall pillars with a 60 μm top tapered down to a different base. One thing that is not directly apparent from Figure 50 is that the absolute photocurrent generated decreases with the size. This means that the smaller the mesa, the fewer number of photons actually interacting with the structure; however, the reduced of the pillar base size would lead to reduced absolute values of photocurrent with a tradeoff between these factors which need to be studied in future work.

The simulation parameters were generated using a wavelength $\lambda = 4 \mu\text{m}$, with a pillar generated by a photoresists called IP-Dip. This photo resist is a two photon polymerization material which is used by the Nanoscribe nanofabrication device.

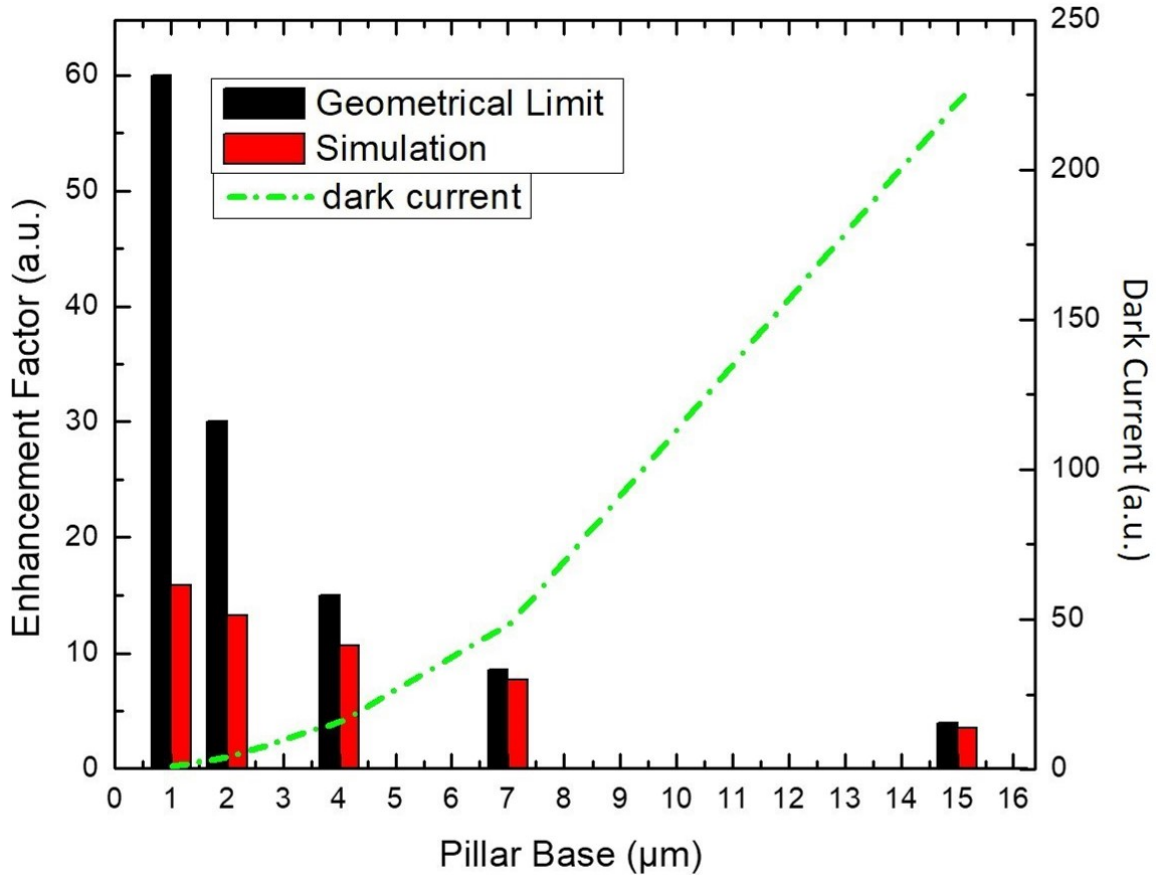


Figure 50: Graphical representation showing the difference between the geometrical limit for enhancement and the simulated enhancement using FDTD simulations. Also shows the tradeoff between the enhancement and the dark current of a FPA with different size mesas.

This photo resist is well documented to be transparent in the infrared regime of the electromagnetic spectrum. The information that is used was generated in [73].

The concept of enhancement comes from efficiently collecting light and delivering it directly to a mesa on a FPA. We study the electric field map to attempt to optimize the design of the structure. The electric field map of the area around the mesa can be seen in Figure 51 for normal incidence.

It is evident from Figure 51 a) and b) that there is a broadening out of the electric field, when the wave nears the end of the taper, allowing for some of the

electromagnetic radiation to escape the mesa. One question is to just have the mesa larger with the smaller taper. We simulated this and for brevity we are not showing as the results are actually worse, with a possible explanation being related to the fact that increased mesa sizes reduce our enhancement factor. An interesting thing happens when the base width of the pillar reaches the wavelength of illumination a photonic jet is generated at the end of the pillar. This jet has a very high concentration of electromagnetic radiation confined in a fairly limited region. This proves that we can reduce the size of the mesa to reduce the dark current without sacrificing the signal that is actually detected by the device. The main problem with the pillar base being less than the wavelength is leakage of the power. It is clear that when the base of the pillar is small there is leakage near the end of the pillar. An interesting aspect is in Figure 51 c) that when the taper of the pillar gets to $\sim 4 \mu\text{m}$ there is a large loss of EM radiation due to side leakage.

One question which has become apparent during this investigation is the real world application of these structures. When thinking about this we must consider the fabrication limitations and time to produce such an array. The height is the main limitation for the Nanoscribe; however, the time of the fabrication can be excruciatingly long. When the process is long it is no longer practical to use in the real world. With this we simulated different pillar heights. The pillars have a standard top width, $60 \mu\text{m}$, and bottom width, $7 \mu\text{m}$. The heights of the pillars range from $150 \mu\text{m}$ to $500 \mu\text{m}$ tall with a step of $50 \mu\text{m}$. We simulated these pillars in $50 \mu\text{m}$ increments and can be seen in Figure 4. The height that gives the best enhancement actually comes from the $450 \mu\text{m}$ tall pillar with $300 \mu\text{m}$ and $500 \mu\text{m}$ giving roughly the same

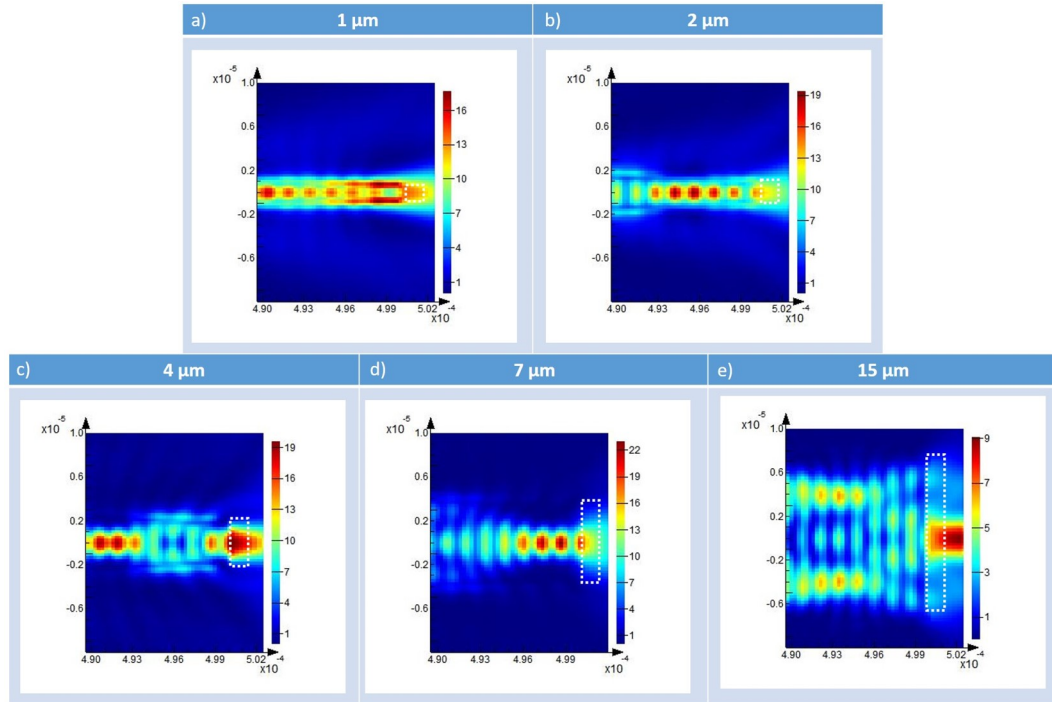


Figure 51: Electric field map calculated by FDTD simulation at $\lambda = 4.0\text{-}\mu\text{m}$ at normal incidence, a) shows a $450\text{-}\mu\text{m}$ tall pillar tapered down to $1\text{-}\mu\text{m}$, b) shows a $450\text{-}\mu\text{m}$ tall pillar tapered down to $2\text{-}\mu\text{m}$, c) shows a $450\text{-}\mu\text{m}$ tall pillar tapered down to $4\text{-}\mu\text{m}$, d) shows a $450\text{-}\mu\text{m}$ tall pillar tapered down to $7\text{-}\mu\text{m}$, e) shows a $450\text{-}\mu\text{m}$ tall pillar tapered down to $15\text{-}\mu\text{m}$.

enhancement. All enhancements are above 5 times and below 8 times enhancement at normal incidence. When placed on a real 3-D structure the enhancement factor should be integrated over the entire mesa and not just a line making the enhancement factor above 25 times and below 64 times. The relative difference is greatest from the highest enhancement, $450\text{ }\mu\text{m}$ tall pillar, and the lowest enhancement, $150\text{ }\mu\text{m}$ tall pillar, giving roughly a 40% difference between the pillar heights, see Figure 52.

Looking deeper into the electric field map at the mesa of each of these structures we develop some insight to what is actually causing the enhancement, see Figure 53. It is clear that height plays a factor in the location of the generated photonic nanojet. It is clear that in Figure 53 a) and b) the photonic nanojet is created and generated

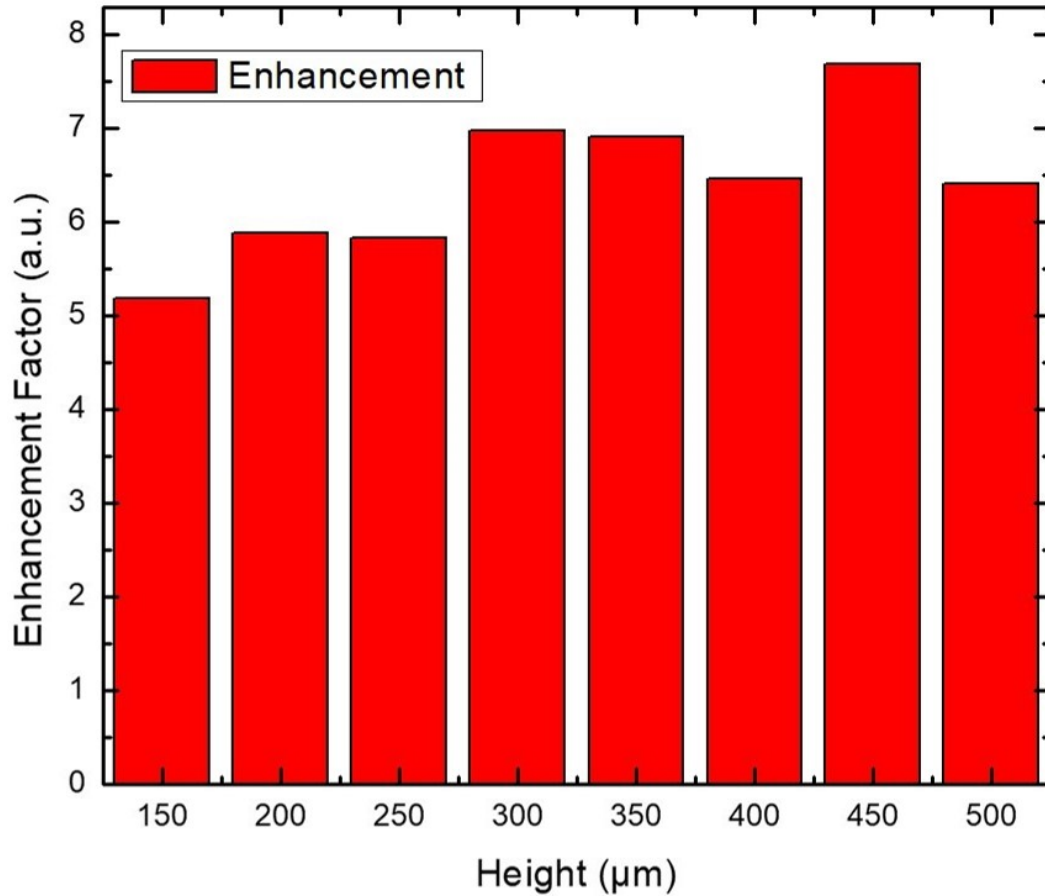


Figure 52: Calculated enhancement factor for different pillar heights at normal incidence. All pillars are $60\text{-}\mu\text{m}$ at the top and tapered down to $7\text{-}\mu\text{m}$ at the base to fit a $7\text{-}\mu\text{m}$ Mesa.

inside of the micro pillar and actually very close to the edge. Previously this was believed to be due to focusing of microspheres with high index having the focal point inside, it is not the same mechanism that generates the photonic jet inside of the pillars. In Figure 53 a) and b) the electromagnetic radiation actually splits and distributed outside of the mesa. One interesting outcome of these results actually comes from an understanding that even with a very tall pillar and a low angle taper, sometimes the conditions are not optimal for enhancing a detector, i.e. due to retro reflections.

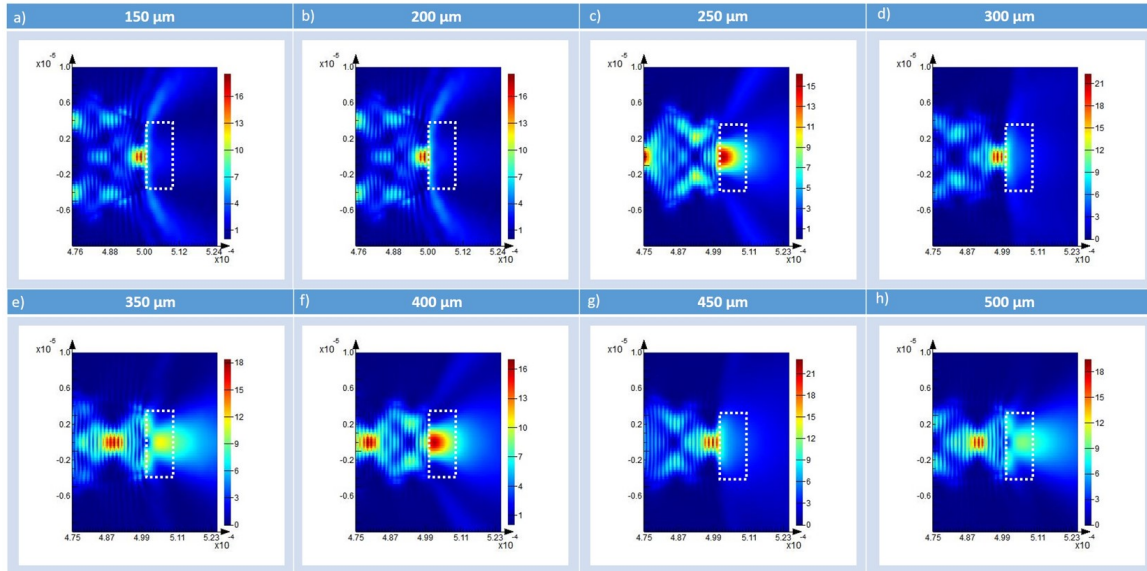


Figure 53: Electric field map calculated by FDTD simulation at $\lambda=4.0\text{-}\mu\text{m}$ at normal incidence, a) shows a $150\text{-}\mu\text{m}$ tall pillar tapered down to $7\text{-}\mu\text{m}$, b) shows a $200\text{-}\mu\text{m}$ tall pillar tapered down to $7\text{-}\mu\text{m}$, c) shows a $250\text{-}\mu\text{m}$ tall pillar tapered down to $7\text{-}\mu\text{m}$, d) shows a $300\text{-}\mu\text{m}$ tall pillar tapered down to $7\text{-}\mu\text{m}$, e) shows a $350\text{-}\mu\text{m}$ tall pillar tapered down to $7\text{-}\mu\text{m}$, f) shows a $400\text{-}\mu\text{m}$ tall pillar tapered down to $7\text{-}\mu\text{m}$, g) shows a $450\text{-}\mu\text{m}$ tall pillar tapered down to $7\text{-}\mu\text{m}$, h) shows a $500\text{-}\mu\text{m}$ tall pillar tapered down to $7\text{-}\mu\text{m}$.

It can be seen in Figure 49 c) and d) that the enhancement factor is for more than just normal incidence. For the mesa in Figure 49 c) it is clear that the microsphere enhancement and the microcone enhancement factor are close to one another and are enhanced for ~ 6 degrees. Whereas Figure 49 d) shows the pillar having a greater enhancement over the microsphere all the way out to ~ 0 degrees. This angle is generally the same for pillars and microspheres.

This led to investigate the angular dependence of different pillar tapers at a height of $450\text{ }\mu\text{m}$ as we did at normal incidence. These tapers begin at $60\text{ }\mu\text{m}$ at the top and taper down to $1\text{ }\mu\text{m}$, $2\text{ }\mu\text{m}$, $4\text{ }\mu\text{m}$, $7\text{ }\mu\text{m}$, and $15\text{ }\mu\text{m}$, see Figure 54. It is obvious that the larger the base width the larger the angle of view, similar to the

microsphere in Figure 49 d). The only explanation for this is that all electromagnetic radiation is tapered down to such a width that the taper size does not matter. This is why at the larger base width the enhancement factor is nearly a plateau and then falls off, see Figure 54; 15 micron.

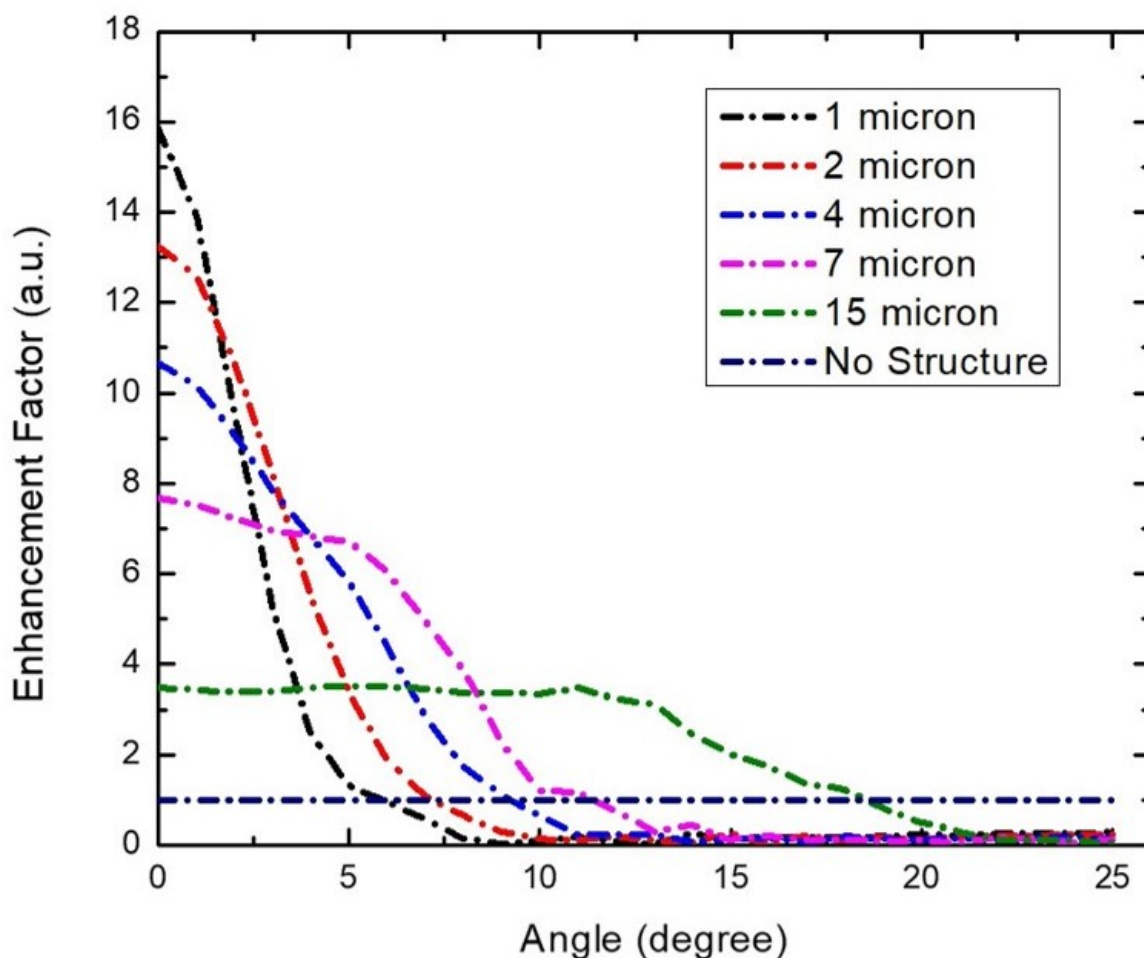


Figure 54: Graph showing the enhancement factor of different pillar tapers at $450\text{-}\mu\text{m}$ tall.

We wished to fully understand what was going on and know if our hypothesis was correct so we investigated the electric field map for each individual base width. For brevity we are only showing the electric field map for one angle for each pillar base width. This angle was chosen to be as close to half of the maximum enhancement

factor that we could find. The smallest half-AOV comes from the smallest base width of $1\ \mu\text{m}$ giving ~ 3 degrees and the largest half-AOV comes from the largest base width of $15\ \mu\text{m}$ giving ~ 13 degrees. One interesting aspect we see with the larger base widths, $7\ \mu\text{m}$ and $15\ \mu\text{m}$, is the formation of what appears to be multiple photonic nanojets out of the structure, see Figure 55 d) and e) which can be viewed as a consequence of multimode interference waveguiding effect [ref] in our structures.

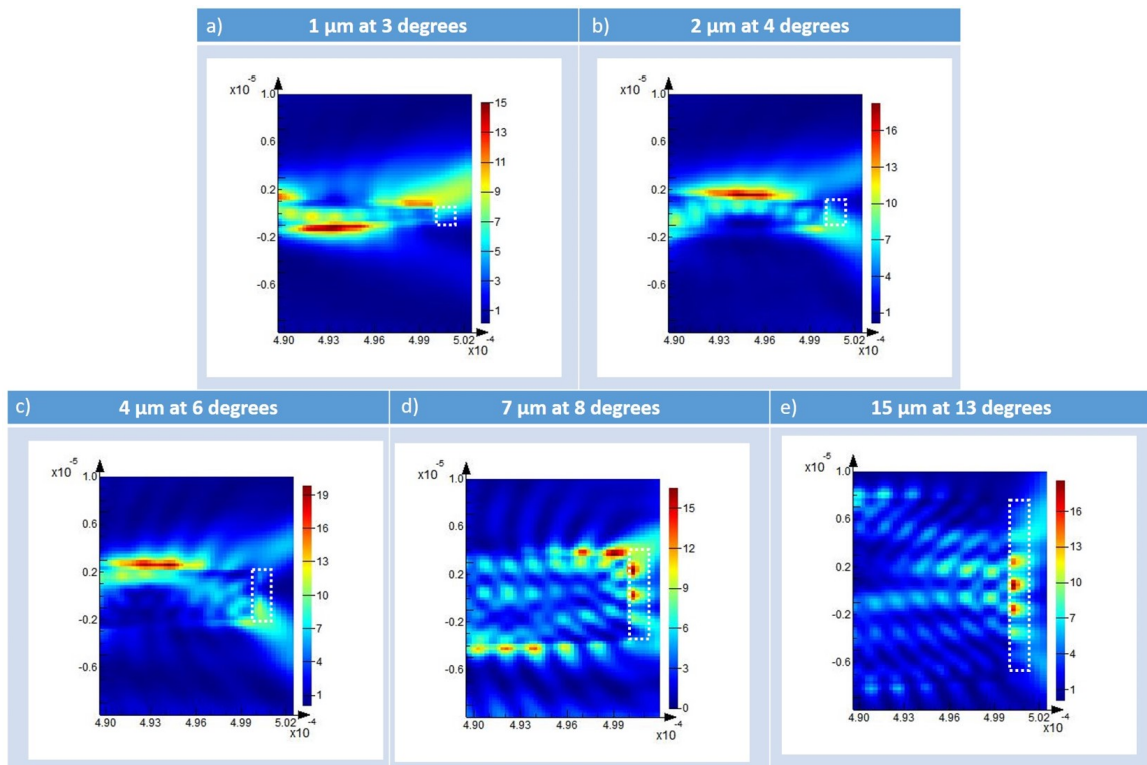


Figure 55: Electric field map calculated by FDTD simulation at $\lambda=4.0\text{-}\mu\text{m}$ at normal incidence, a) shows a $450\text{-}\mu\text{m}$ tall pillar tapered down to $1\text{-}\mu\text{m}$ at approximately half the normal enhancement factor, b) shows a $450\text{-}\mu\text{m}$ tall pillar tapered down to $2\text{-}\mu\text{m}$ at approximately half the normal enhancement factor, c) shows a $450\text{-}\mu\text{m}$ tall pillar tapered down to $4\text{-}\mu\text{m}$ at approximately half the normal enhancement factor, d) shows a $450\text{-}\mu\text{m}$ tall pillar tapered down to $7\text{-}\mu\text{m}$ at approximately half the normal enhancement factor, e) shows a $450\text{-}\mu\text{m}$ tall pillar tapered down to $15\text{-}\mu\text{m}$ at approximately half the normal enhancement factor.

We look at the angle of view for different pillar heights as well, similar to the enhancement factor seen above. We again had a standard pillar top width, $60\ \mu\text{m}$,

and bottom width, $7 \mu\text{m}$. The heights of the pillars range from $150 \mu\text{m}$ to $500 \mu\text{m}$ with $50 \mu\text{m}$ intervals again. The enhancement of a given pillar height can be seen in Figure 56.

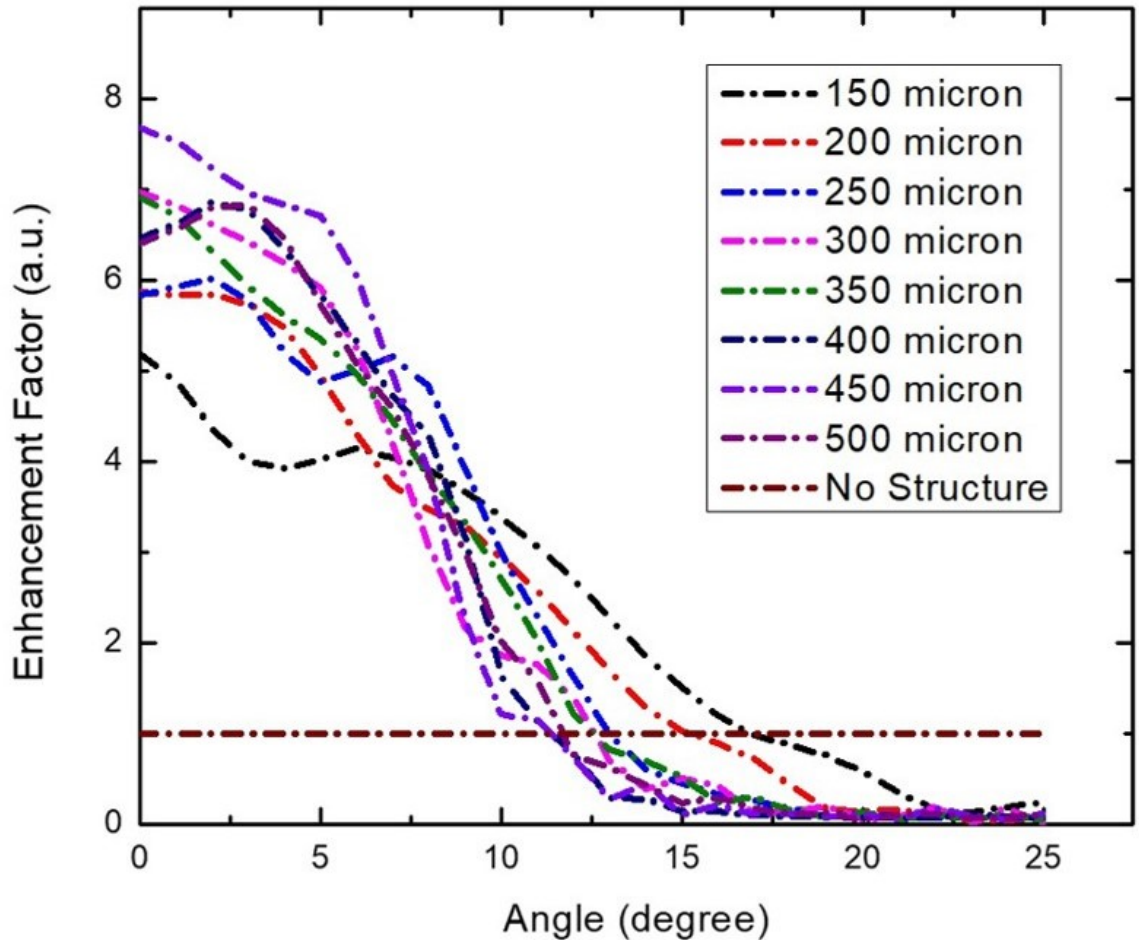


Figure 56: Graph showing the enhancement factor of different pillar heights tapers go down to $7\text{-}\mu\text{m}$.

We again turn to the electric field map to attempt to understand the effects of different pillar heights on the angle that the light is collected. The highest AOV comes from the $150 \mu\text{m}$ tall, 12 degrees, structure and decreases slightly until it saturates at the $300 \mu\text{m}$ structure, 8 degrees.

Fabrication and testing this idea for enhancing FPA has been done using short-

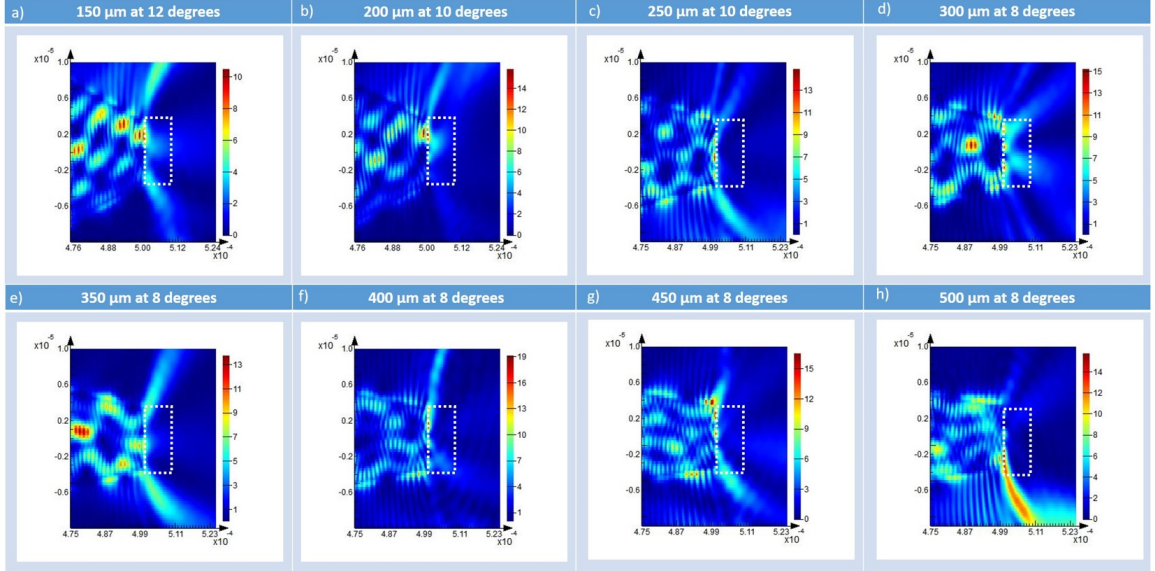


Figure 57: Electric field map calculated by FDTD simulation at $\lambda=4.0\text{-}\mu\text{m}$ at normal incidence, a) shows a $150\text{-}\mu\text{m}$ tall pillar tapered down to $7\text{-}\mu\text{m}$ at approximately half the normal enhancement factor, b) shows a $200\text{-}\mu\text{m}$ tall pillar tapered down to $7\text{-}\mu\text{m}$ at approximately half the normal enhancement factor, c) shows a $250\text{-}\mu\text{m}$ tall pillar tapered down to $7\text{-}\mu\text{m}$ at approximately half the normal enhancement factor, d) shows a $300\text{-}\mu\text{m}$ tall pillar tapered down to $7\text{-}\mu\text{m}$ at approximately half the normal enhancement factor, e) shows a $350\text{-}\mu\text{m}$ tall pillar tapered down to $7\text{-}\mu\text{m}$ at approximately half the normal enhancement factor, f) shows a $400\text{-}\mu\text{m}$ tall pillar tapered down to $7\text{-}\mu\text{m}$ at approximately half the normal enhancement factor, g) shows a $450\text{-}\mu\text{m}$ tall pillar tapered down to $7\text{-}\mu\text{m}$ at approximately half the normal enhancement factor, h) shows a $500\text{-}\mu\text{m}$ tall pillar tapered down to $7\text{-}\mu\text{m}$ at approximately half the normal enhancement factor.

wave IR (SWIR) detectors. These pillars were fabricated at AFRL on the Nanoscribe and have shown to be well aligned with the photodetector mesas. These microcones are fabricated in the photoresist IP-DIP using 2 photon polymerization, going point to point through the entire 10×10 array. The time to fabricate and to get a good result, not having a layered structure, is ~ 20 minutes.

4.4 Conclusions

Using FDTD modeling the collection of light by 2-D microcones is studied as a function of the geometrical parameters: 1) size of the pillar base with stationary

height, b) height of the pillar with stationary base, and c) angle of incidence. We calculated the power transmitted through microcones and estimated the enhancement factor which was defined as a ratio of power transmitted through microcones and the power incident on the mesa without any microcones for the same power of the incident plane waves. Along with the transmitted power, we also calculated 2-D EM maps illustrating the field buildup processes inside the microcones due to multimode interference processes.

The results generally showed the advantage of small base sizes for achieving the largest enhancement factors combined with a significantly reduction of the dark current proportional to the detector size. At the same time, further reduction of the base sizes will inevitably lead to the reduction of the signal which would negatively impact the performance of FPAs. The optimization of the base sizes is a subject of future studies.

The transmission coefficients of the microcones do not display strong dependences in the selected range of pillar heights from 150 to 500 micron at normal incidence. The studies of how transmission depends on the pillar heights at oblique incidence is a subject of future studies.

The dependences of transmission on the angle of incidence showed that AoV is strongly dependent on the size of the base. The enhancement factors are largest and AoV narrowest for the minimal base sizes. Generally, AoVs are on the order of 10 degrees which is much larger compared to AoVs provided by the commercial microlens arrays.

CHAPTER 5: OBSERVATION OF PHOTOINDUCED AGGREGATION OF PLASMONIC NANOPARTICLES IN A SOLUTION

5.1 Introduction

Our studies of photoinduced aggregation of naoplasmonic particles were initiated by research performed at MIT Lincoln Labs by Dr. Vladimir Liberman and Dr. Mordechai Rothschild [155]. They discovered a novel phenomenon of optical beam manipulation with plasmonic nanoparticles with $100\times$ on-axis rejection of beam intensity achieved. This phenomenon attracted attention because the robust agile switches for intense radiation from optical to radio frequency (RF) are needed for various applications. More specifically, in the optical regime such switches are needed for alleviating of threats to aviation security and in RF/microwave regime to enable fast phased array switching [157].

In the work performed at MIT Lincoln Lab [155] it was observed that suspensions of Au and Ag plasmonic nanoparticles, irradiated with 532-nm, ns-long pulses, exhibit nonlinear absorption, nonlinear scattering and saturable absorption [156]. Laser-induced damage is suppressed by $>100\times$ when the solvent is toluene instead of water. They determined highest optical nonlinear coefficients for Au and Ag plasmonic nanoparticle known to date. Regarding the mechanism of the observed enhancement of nonlinear coefficient, they suggested that it arises from increased local fields due to the plasmonic resonance in the nanostructures.

The work presented in this chapter was motivated by our hypothesis that the mechanism of optical nonlinearity in suspensions of plasmonic particles can have a motional contribution related to photoinduced movements of nanoparticles in a solution. As we considered in Section 1.7 of Introduction, the plasmonic particles are subject for various light-induced forces. By moving towards the gradient of the intensity, they can create formations or structures with significantly larger scattering cross-sections when just a simple sum of the individual scattering cross-sections. Such processes can take place on a millisecond (or even faster) time scale in a solution and they can cause a significant increase of nonlinear absorption and scattering[218]. In principle, such processes can be a factor contributing to the effects observed in MIT Lincoln Lab, however evaluating these effects would require obtaining more direct information about the particle distribution in response to intense laser beam illumination [157].

Initially, we started our studies of photoinduced aggregation of nanoparticles in attempt to resolve the nanoparticles in a solution using our previously developed super-resolution imaging techniques. The typical particles dimensions range from 10 to 100 nm, and, in principle, the particles larger than ~ 50 nm can be observed (if they are fixed on the substrate) using super-resolution imaging through high-index microspheres. We were motivated by our previous results of imaging of nanoplasmonic nanodisks and other objects on the substrate. We found, however, that the imaging of nanoparticles in a solution is much more challenging compared to their imaging on a substrate because of their fast Brownian motions. The nanoparticles can be seen only when they intersect an imaging plane in the course of their motion, and since the focal depth is rather narrow (submicron scale) and the motion of particles is

extremely fast, the time intervals when the nanoparticles can be visualized are rather short and reconstructing the trajectory of these nanoparticles is practically difficult by our method of super-resolution imaging.

In the course of these studies, I performed many attempts to visualize the nanoparticles using different suspensions and solutions. I also used different microscope systems including our upright Mitutoyo microscope, FL inverted Olympus microscope and laser scanning confocal Olympus microscope. I was only able to see individual nanoparticles after evaporation of the suspension when they became completely dry and immobile on a substrate.

These studies led me to very interesting observation which puzzled me, and it became a subject of studies included in this Chapter. This observation is not related to direct observation of photoinduced motions in a solution. It is rather related to a kind of, "optical memory," effect which I observed by using local photoexcitation of a thin film of nanoplasmonic suspension (such as a droplet) after its full evaporation. I noted that the position where I kept the focused spot of the mercury lamp for excitation of the FL of nanospheres became dark after the complete evaporation of solution. Using SEM analyses, we showed that dark appearance of this spot is determined by the aggregation of very small ~ 20 nm Au nanoparticles in the excitation spot. It is not clear to us if this aggregation takes place on very fast time scale directly inside the solution. Taking into account small intensity levels inside the excitation spot (attenuated focused mercury lamp), this seems to be unlikely. However, it is possible that the effect takes place gradually on the stage of suspension evaporation. At this stage, the nanoparticles are subject for microfluidic forces mentioned in Section

1.7 of Introduction. Nonuniform illumination can lead to appearance of nonuniform microfluidic forces which provide conditions for particle deposition at the position of the local external photoexcitation. In principle, the effect observed by us can be used for developing new technology of light-controlled particle deposition. The specific properties of this process require further studies. In particular, we demonstrated a principal possibility to record images on a substrate, such as image of letter A, however in this theses work we present only the results of our first observation of this effect. More detailed characterization of its properties and, first of all, its spatial resolution is outside the scope of this theses work.

We begin this Chapter with a brief description of the work performed at MIT Lincoln Lab which initiated the work on such photoinduced assembly in nanoplasmonic solutions. After that we switch to our experimental results and finally we come to conclusions.

5.2 Previous work performed at MIT Lincoln Lab

Recent irradiation studies of plasmonic nanoparticle suspensions revealed strong nonlinear response in both the nonlinear absorption and scattering coefficient [157, 156]. Correlation of the nonlinear absorption to the plasmonic properties of the nanoparticles has been suggested previously. However, detailed mechanistic studies have been limited due to damage to nanoparticle material during irradiation. The work at MIT Lincoln Lab presents pulse-by-pulse irradiation studies designed to separate multiple-pulse damage from intrinsic nonlinearities of the nanoparticle suspensions [157]. The method is used to study nanoparticle suspensions of various shapes

(spheres vs. disks), materials (Au and Ag), sizes and solvents. Dramatic reduction ($>100\times$) to material damage is found for suspensions in toluene vs. water. In the work of MIT Lincoln Lab the nonlinear absorption was separated from scattering and the experimental results were compared to modeled nonlinear susceptibility from mean-field theory [156].

In Liberman's work [157], commercial Au and Ag nanospheres were obtained in a range of diameters between 30 and 150 nm. Citrate- and PVP-capped nanoparticles were dispersed in water. Alkyl-acrylate-capped Au nanospheres were dispersed in toluene, acetonitrile and dichloroethane. Custom Ag nanodisks of 45-nm diameter and 25-nm thickness were synthesized via a solvothermal method and dispersed in water.

The nanoparticle suspensions were irradiated with 4-ns pulses from a 532-nm laser. Transmission was recorded on a pulse-by-pulse basis to separate laser-induced damage effects from intrinsic material nonlinearities. Laser intensity was varied from <20 to $>600 \frac{mJ}{cm^2}$ per pulse with an in-situ attenuator, while the irradiation spot size was kept fixed at 0.5-mm diameter at the sample. An automated translation stage ensured that each pulse exposed a fresh part of the sample. Variable-aperture experiments were performed to separate sample absorption from low-angle scattering. Experimental transmission data were analyzed by relating the local intensity I and the generalized attenuation coefficient α through beam propagation equation as follows [157]:

$$\frac{dI}{dz} = -\alpha(I)I \quad (30)$$

$$\alpha(I) = \frac{\alpha_0}{1 + \frac{I}{I_s}} + \beta I + \gamma_s I \quad (31)$$

In Eq. 31, α_0 , I_s , β and γ_s are fitting parameters, referring to initial absorbance, saturation intensity, nonlinear absorption and nonlinear scattering coefficients, respectively. The intensity from Eq. 32 [157] was integrated over sample thickness and Gaussian pulse width to fit the experimental transmission data [156].

Pulse-by-pulse irradiation of the same spot of Au nanosphere suspension in water and toluene, see Figure 58, reveal drastic differences in behavior. For the water suspension, sample transmission drops initially as would be expected from intensity-dependent nonlinear absorption, but bleaches due to damage within 2 pulses. The bleaching is accompanied by discoloration of the solution, presumably due to laser-induced fragmentation of nanoparticles. By contrast, transmission of the toluene suspension remains stable on the scale of 10^3 pulses and much less discoloration is observed.

By translating the sample to a fresh spot after every pulse, we have been able to minimize damage to the nanoparticle in water and measure the intrinsic nonlinear coefficient β , Eq. 31. Comparing this nonlinearity to previously-obtained β for, "bulk," Au [206] and Ag [226] and normalizing by volume fraction, we derive the β -enhancement parameter, see Figure 58(b) [156]. For the Ag nanoparticles, the highest enhancement is observed for the disk shape, whereas for the spheres, the enhance-

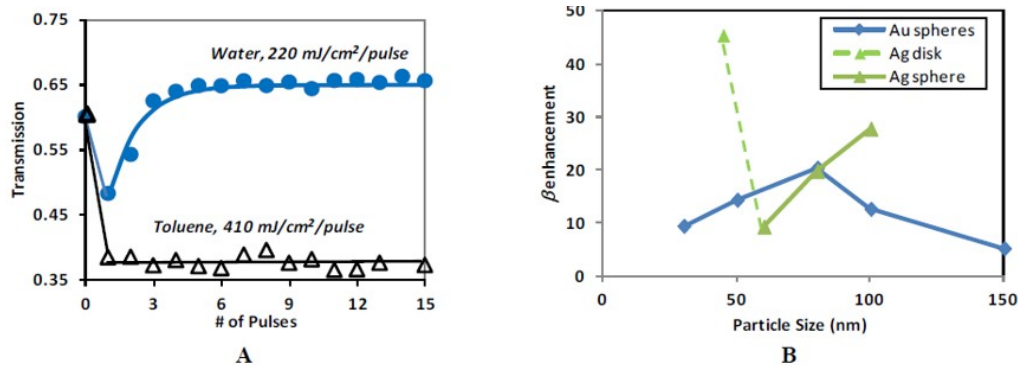


Figure 58: A) Transmission vs. number of pulses for Au nanoparticle suspension in water (solid circles) and toluene (open triangles) obtained without translating the sample. B) Nonlinear absorption enhancement for Au spheres, Ag disk, and Ag spheres; all in water suspensions, as a function of particle size.[157]

ment increases with particle diameter. On the other hand, for Au nanospheres, the enhancement is comparable to that of Ag nanospheres but the maximum value occurs at ~ 80 nm diameter and falls off for larger particle sizes. The nonlinear coefficients for Au nanoparticles in water measured in this study, see Figure 58(b) [157], are the highest reported to date for such material. We believe that minimizing damage to the particles allowed us to measure such a large nonlinear effect. In fact, when translating to a fresh sample spot after every pulse, nanoparticles in either water or toluene solvent displayed similar nonlinear absorption. It is postulated that β -enhancement arises from increased local fields due to the plasmonic resonance in the nanostructures [157]. Utilizing mean field theory, the MIT Lincoln Lab group presented the expected enhancement by explicitly averaging field intensity over the particle volume and showed qualitative agreement with the trends of β -enhancement of previous studies, see Figure 58(b) [157].

MIT LL group has also additionally separated nonlinear scattering from the nonlinear absorption loss component by performing variable-aperture exposures. They

found that for water suspensions of nanoparticles nonlinear scattering is comparable in magnitude to nonlinear absorption. For toluene suspensions, nonlinear scattering is reduced. They believed that the scattering to be related to particle break-up and microbubble formation that occurs on the nanosecond time scale during a single pulse [157].

Thus, the studies performed by MIT LL group attracted attention to very interesting mechanism of the optical nonlinearity appearing in response to strong optical pulses in suspensions of plasmonic nanoparticles. They suggested several mechanisms of the observed effects including increased optical nonlinearity at the plasmon resonance wavelengths, particle photoinduced break-up and microbubble formation. They also previously observed formation of nanourchins in such suspensions in their previous studies, as illustrated in Figure 59 [157].

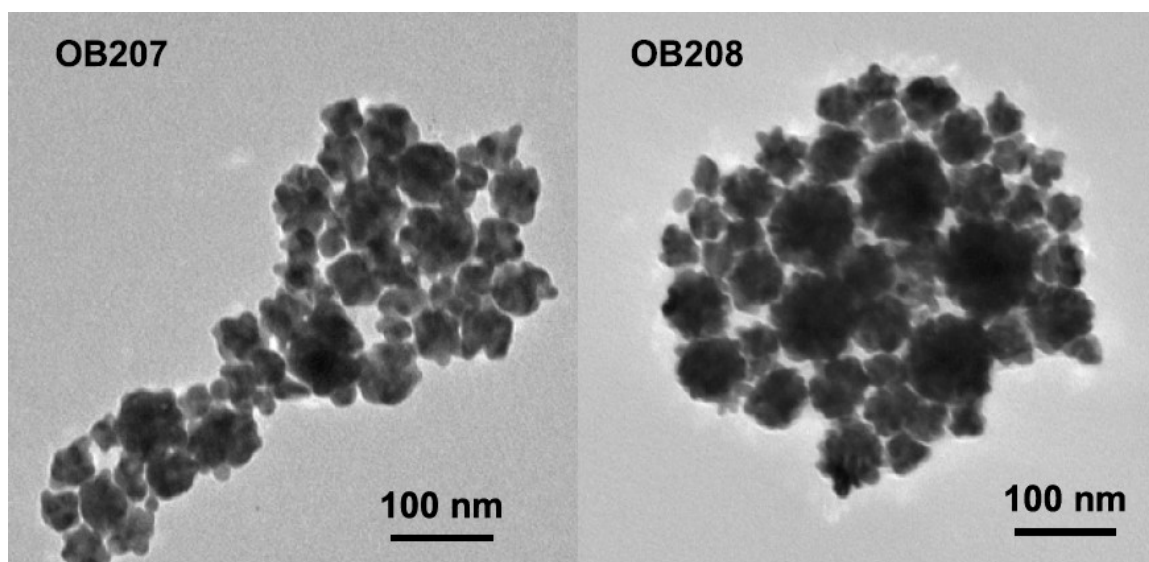


Figure 59: Representative TEM micrographs of two Au urchin samples. The micrographs show loose aggregates of the urchin, which were formed in the process of drying the solutions for TEM sample preparation. The nanourchins are dispersed in the solution.[157]

5.3 Experimental Results

The experiments performed at MIT Lincoln Lab were performed at very high laser powers which are available under conditions of pulsed laser excitation. On the other hand, we had a hypotheses that a completely different mechanism of the optical nonlinearity might take place due to laser excitation in a solution when the particle would aggregate under the influence of the optical forces. There are many different optical forces which in principle can be involved in such situations: a) photophoretic forces [16], b) light pressure [40], c) optical binding forces [19] due to complicated collective light scattering effects in such clusters of nanoparticles.

In this theses work, we decide to find some traces of these effects using significantly weaker excitation powers available using mercury lamp in our inverted Olympus microscope. On the other hand, in order to exert a prolonged photoexcitation, we decided to use a continuous illumination of the nanoplasmonic suspension with the focused beam obtained from the mercury lamp. The results of such studies are presented in the next paragraphs.

5.3.1 Size Dependence

We looked at different size nanoparticles; 20 nm, 50 nm, 70 nm. The 20 nm Au nanoparticles are in a solution of deionized water. The 50 nm Au nanoparticles are in a solution of toluene. The 70 nm nanoparticles are in a solution of deionized water and Au nanoparticles. The illumination was done by a 100W arc mercury lamp focused through a 100x objective on an Olympus IX-71 inverted microscope.

The initial work, as stated above, was to visualize 50 nm nanoparticles in an

aqueous solution to verify the ability to use these nanoparticles as an optical limiting agent to protect valuable sensing devices that are damaged by high intensity electromagnetic radiation. We found that it was possible to visualize single nanoparticle using a confocal microscope after drying using a 405 nm laser for observation. However, when we switched to FL microscopy, a 10 μ l droplet of the nanoparticle solution was deposited directly onto a coverslip which is used to observe the effect of interest. Both during evaporation and after drying there were no discernable features that were observable. Dilution of the solution had to be done in order to visualize this single nanoparticle after it is immobilization on a substrate as a result of evaporation of solution. It was not until we used 10 μ l of solution and 10 μ l of Toluene when observations of single nanoparticles were successful. The solution was still opaque during the evaporation process. We moved to white light for observation with no success.

We moved from 50 nm Au nanoparticles to 20 nm and 70 nm Au fluorescent nanoparticles. The choice of fluorescent nanoparticles was because of the signal in fluorescent imaging is so much greater than the background. The first set of fluorescent nanoparticles that we used were 70 nm nanoparticles in deionized water. The 70 nm nanoparticles were chosen due to the surface plasmon resonance, 540 nm, being nearly identical to the excitation of the mercury lamp attached to the microscope, 542 nm. We moved from a microsphere embedded coverslip to using an Ar-Ion laser illuminating from the side with microspheres inside of the solution. The idea is the generation of a photonic nanojet will attract nanoparticles and will have a high concentration of nanoparticles on the dark side of the microsphere. We then attempted

to illuminate a part of the sample with mercury lamp with the Ar-Ion laser in hopes of seeing some aggregation. We figured that it was the size of the particles that was making it so we could not see any aggregation.

We moved to 20 nm nanoparticles that have a surface plasmon resonance that is away from the output of the mercury lamp filter combination of the microscope. We noticed something very peculiar when doing this, the nanoparticles were aggregating in an area near where the mercury lamp was illuminating. We removed the Ar-Ion laser and the microspheres to see if the phenomena happened again and it did, see

Figure 60.

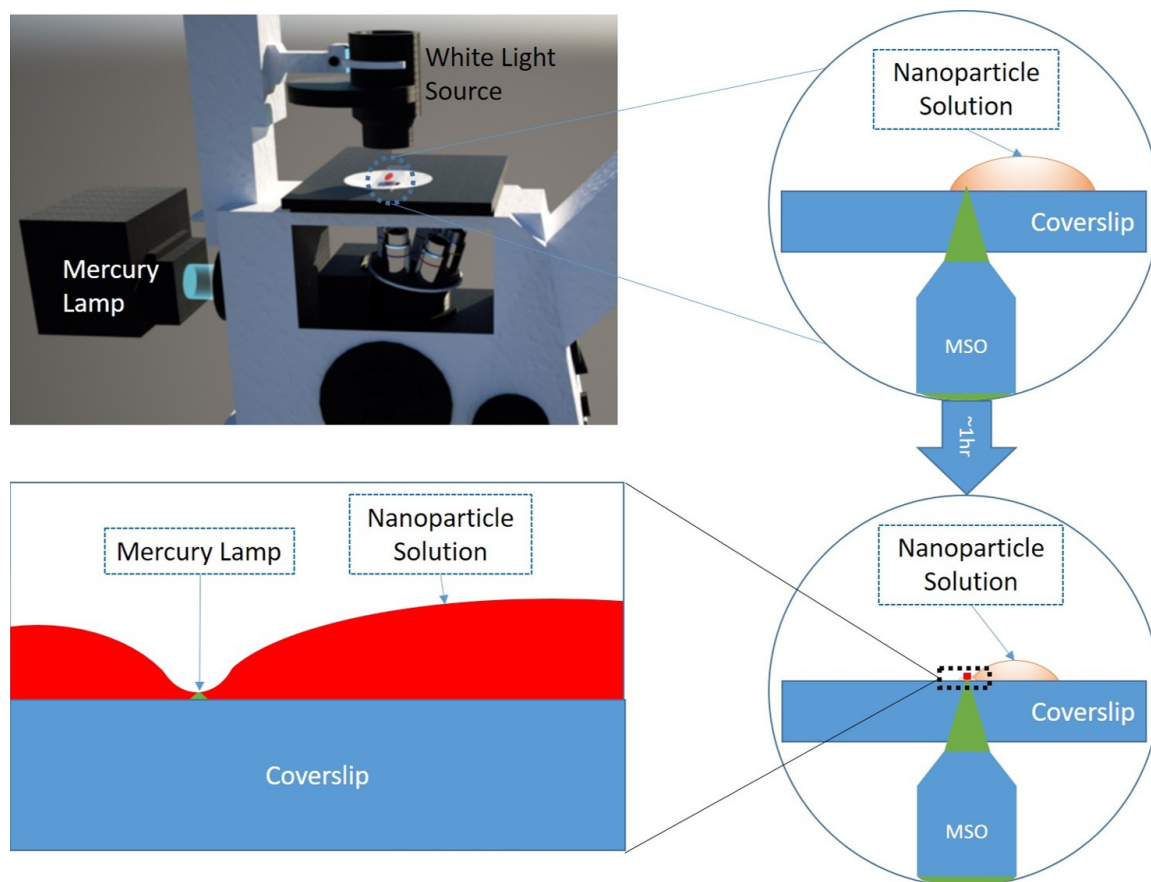


Figure 60: Schematic showing the process of aggregating nanoparticles using continuous illumination from a mercury lamp.

We also looked at the use of 20 nm nanoparticles in a more viscous form by adding IPA to the solution. Adding IPA allowed for the time of evaporation to be cut to approximately a quarter of the time of just the solution with similar results. In order to ensure that the results were valid we placed a filter with the letter A in the path of the mercury lamp and attempted to see the results, see Figure 61.

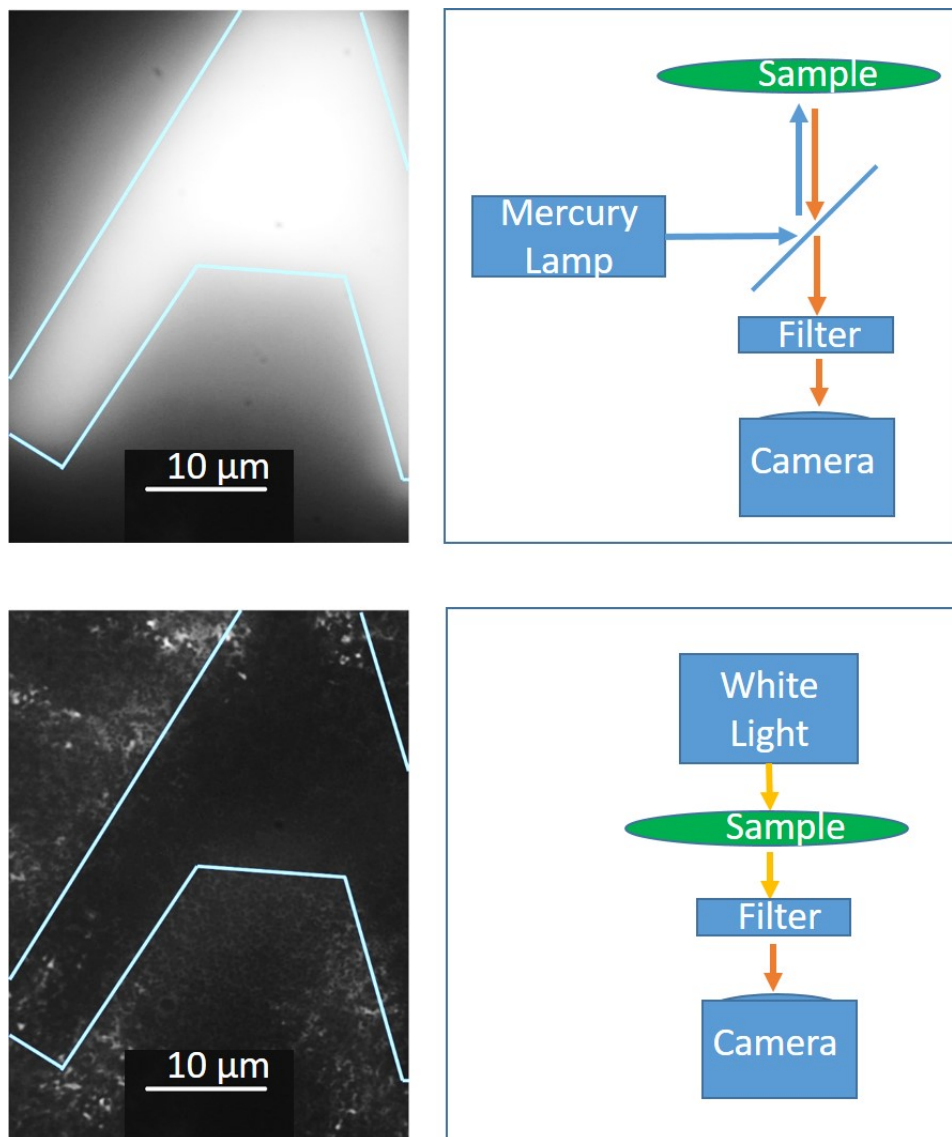


Figure 61: Experimental results showing aggregation in the form of a letter A.

5.3.2 Frequency Dependence

A dark spot in transmission mode was formed while using 20 nm nanoparticles with the severity of the spot size changing with different frequencies. We used different frequencies in order to see if there is a dependence on the frequency of illumination. In the microscope we have different filter crystals. I used a UV excitation filter crystal (center ~ 365 nm), Blue excitation (center ~ 460 nm), and Green excitation (center ~ 540 nm), see Figure 62.

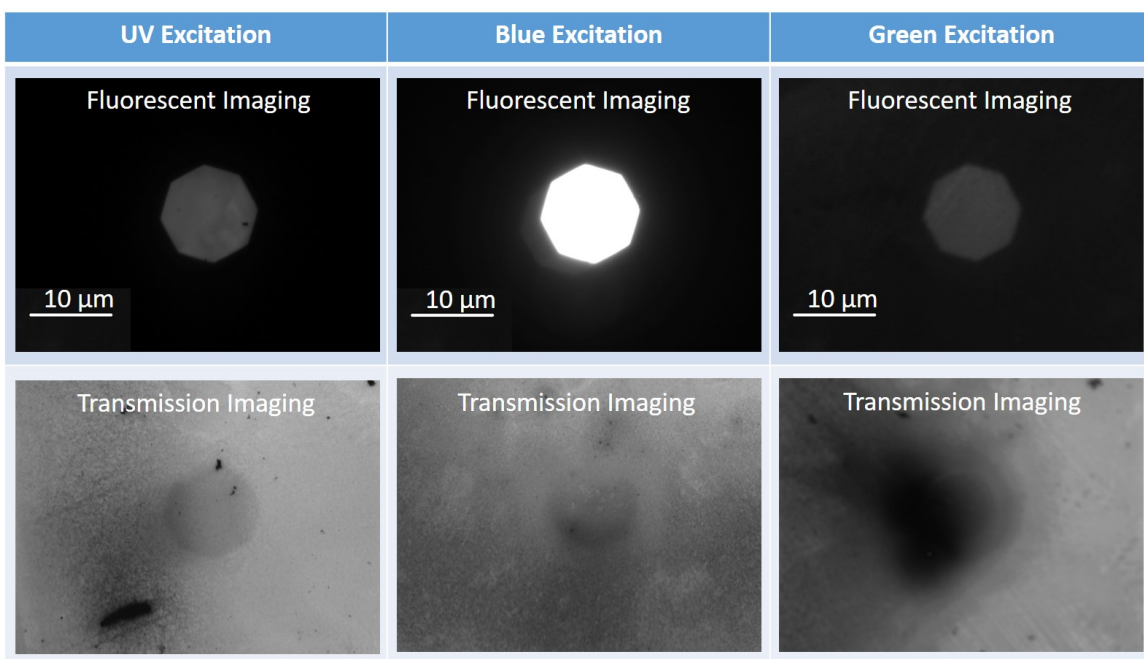


Figure 62: Frequency dependence on aggregating 20 nm Au nanoparticles.

Through transmission imaging it is clear that the light transmission is reduced using the green excitation crystal over the UV and blue excitation crystal. There is still a memory of nanoparticles where the mercury lamp excitation is illuminating the solution. This decrease in transmission is due to particles aggregating to that location. We also conclude that from the aggregation is due to localized heating of the solution.

From the UV excitation crystal it is due to localized heating of the water solution; whereas, for green excitation crystal it is due to the heating caused by the surface plasmon resonance of the nanoparticles.

5.3.3 Intensity Dependence

The final study conducted involved the intensity of the light source. We limit the intensity using neutral density (ND) filters. Measurements were taken with no ND filter, ND 12 filter, ND 25 filter, and ND 37 filter. We dropped 10 μl of the nanoparticle solution and 10 μl of IPA onto a 120 μm thick coverslip for all of these experiments and allowed for the solution to be illuminated for an hour each. We then allowed for any excess liquid to evaporate over the next week and placed it into a scanning electron microscope (SEM) and imaged two locations on each sample. The first location we looked at was the focal point of the 100x microscope objective. The second location we looked at is outside of the focal spot. A random location between the edge of the droplet and the focal point was chosen, see Figure 63.

5.4 Conclusion

Light-driven assembly of nanoplasmonic particles is observed as an optical memory effect in a sense that it became apparent after full evaporation of the liquid suspension due to nanoparticle aggregation in the illuminated regions.

The conditions required for observation of this effect are determined. This include: a) photoinduced aggregation was observed only in suspensions of small, ~ 20 nm, particles and it was not observed in suspensions of large, ~ 70 nm, particles. The exact nanoparticle size dependence of the observed effect requires further studies.

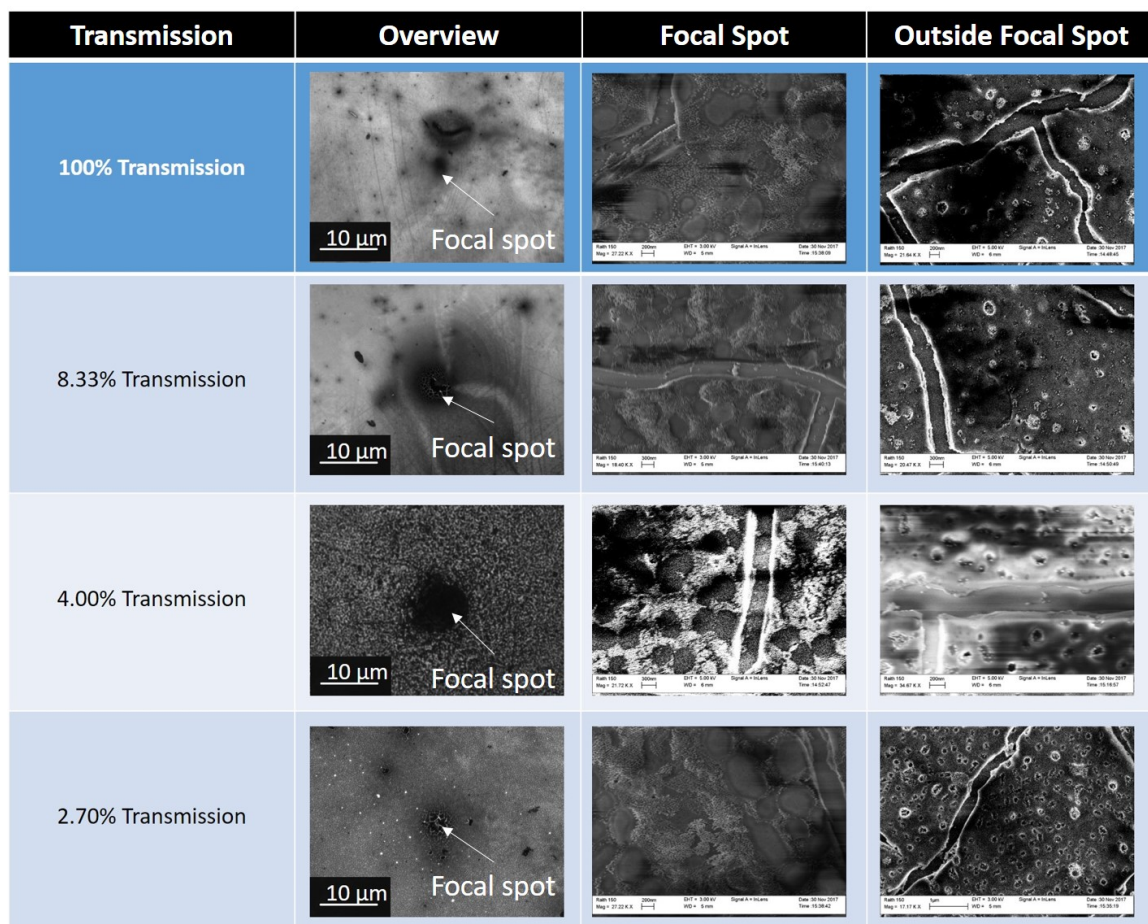


Figure 63: Experimental results showing the aggregation of nanoparticles in the focal spot and outside of the focal spot of Au nanoparticles aggregated at ~ 540 nm excitation light.

The level of photoexcitation intensity required for observation of this effect is many orders of magnitude smaller compared to the previous experiments performed in MIT Lincoln Lab where the intense laser pulses were used. We showed that the effect persists in the case of using neutral density filters reducing the intensity of focused light of the mercury lamp at least down to 2.7% of the full available intensity.

The mechanism of the observed effect requires further studies. Based on our results we suggest that this mechanism is related to the thermal effects locally speeding up the evaporation of the thin liquid film of the suspension.

Direct light action of plasmonic nanoparticles is possible in the form of photophoretic forces, radiative pressure, and/or optical binding forces. However, the intensities of photoexcitation are rather small in our experiments (we did not perform quantitative intensity measurements, but they are many orders of magnitude smaller compared to experiments where such direct light action of nanoparticles was studied previously). For this reason, we believe that the direct laser action on nanoparticles is not a likely explanation of the observed effect.

More likely explanation is based on a two-stage process. On the first stage, a prolonged illumination with the focused beam of mercury lamp causes local heating effects in the illuminated region of the thin liquid film. These local heating effects speed up the evaporation of the liquid suspension causing the thinning of the liquid thin film in the illuminated area and in the adjacent region creating wedge-like areas in the adjacent regions. On the second stage, the nanoparticles are dragged into the narrowing sections of suspension by the microfluidic forces. These forces are similar in nature to coffee-ring effects and/or Marangoni fluxes which are used for the surface deposition of nanoparticles or nanospheres. There are many possible outcomes of such self-assembly depending on the interplay of the forces involved. However, the common outcome is that the nanoparticles are sucked into the wedge-like shape by the microfluidic forces and positioned close to the interface of slowly evaporating liquid. Once the interface of evaporating liquid passed above these particles, they become firmly attached to the substrate.

The observed effect required further studies. In particular the following dependences need to be investigated in more detailed way: a) Dependence on the nanopar-

ticle size and shape, b) The role of plasmonic resonance can be revealed and studied by comparing results of assembly Au and Ag particles which have different plasmonic resonance properties which means that their assembly can be activated by illumination with different wavelengths. c) The spatial resolution of this method of assembly of nanoparticles need to be investigated. It can be achieved using projected images with different dimensions.

The observed effect can have applications for developing light-driven parallel assembly of massive number of nanoparticles. These assemblies can be used as templates for SERS or as various sensors of nanoparticles. The techniques are scalable to a massive-scale production, simple and inexpensive. However, it requires further studies to determine its spatial resolution, ability to assemble particles with different shapes, and its ultimate capability to control the speed and quality of assembly.

CHAPTER 6: INVESTIGATION OF LIGHT SCATTERING BY DIELECTRIC MICROSPHERES AIMED AT APPLICATION OF INVERSE SCATTERING ALGORITHMS

6.1 Introduction

When an optical wave is transmitted through an aperture and travels some distance in free space, the intensity distribution is called the diffraction pattern. Typically this diffraction pattern deviates from the pattern that is expected when treating light as a ray instead of a wave. This diffraction depends on the distances between the aperture and observation plane, the wavelength, and the dimensions of the aperture. The complex amplitude of the wave propagating through the aperture plane to the observation plane. This is well known as Fraunhofer diffraction and is limited to when the observation plane is sufficiently far from the aperture such that the Fresnel number is much less than one, see Eq. 32 [101].

$$N'_F = \frac{b^2}{\lambda d} \lll 1 \quad (32)$$

Where N'_F is the Fresnel number, b^2 is the radius of the aperture, λ is the wavelength of light propagating through the aperture, and d is the distance to the observation plane.

Fraunhofer diffraction is used as a tool to understand an output of an optical system. This tool can also be used as a method to get information about the aper-

ture from the retarded information obtained at the observation plane. Looking in particular at a circular aperture, we know that the intensity pattern follows [159]:

$$I(x, y) = I_p \left(\frac{\pi D^2}{4\lambda d} \right)^2 \left\langle \frac{2J_1\left(\frac{\pi D \rho}{\lambda d}\right)}{\frac{\pi D \rho}{\lambda d}} \right\rangle^2 \quad (33)$$

Where $I(x, y)$ is the intensity of the diffraction pattern on the observation plane, I_p is the peak intensity, D is the diameter of the aperture, λ is the wavelength of illumination, d is the distance from the aperture to the observation plane, $J_1(*)$ is the Bessel function of order 1, and ρ is $\sqrt{x^2 + y^2}$.

Because of this we can take a diffraction pattern and, if it is an Airy pattern we can reverse engineer the aperture that created the pattern. The entire concept of inverse scattering problems begins with this base, an output is obtained and we are interested in what created that output. The more information that one has about the system the easier it is to actually reverse back to the information that is desired.

The formulation of the inverse scattering problem is nontrivial in a sense that ultimately the information about the object is completely absent. This means that we have a diffraction or scattering pattern produced by the unknown object and we would like to find the distribution of real and imaginary part of the refractive index of such an unknown object. The recovery of the information about the object requires significant information about its scattering properties which usually can be obtained in the form of phase distributions within the scattering patterns along with the amplitude distributions. An example of such reconstruction is represented by holography where the phase information about the object is recorded in the hologram obtained as

a result of interference of the scattered light produced by the object and the incident plane wave. As it is well known, the object can be recovered by illuminating the hologram by the same incident plane wave. In a more general case, the recovery of information about the object requires the mathematical apparatus which is usually based on the Born approximation. Such algorithms are known and they were applied for the object reconstruction in experimental studies. Our collaborators, Prof. Michael Klibanov, in the Department of Mathematics and Statistics at the University of North Carolina Charlotte has developed a method that needed experimental data to test. This method is a new numerical method for solving a 3D Phaseless Coefficient Inverse Problem (CIP) for the Helmholtz equation. This is done using a single experimental measurement of the square modulus of the complex valued wave field. There is currently only one publication in which 3D phaseless CIP [134] would be computationally solved for the case when the experimental intensity data would be collected for a single measurement event [134].

The method consists of two stages: (1) asymptotic analysis is used to obtain an estimate for the scattered wave field [134] and (2) use of a globally convergent numerical method to reconstruct the desired refractive index from the total wave obtained by adding the incident wave field and the scattered wave field [134]. This approach has several benefits over different approaches as it does not require a good initial guess of the true solution to obtain good results. It consists of collecting information about the object in a form of scattering intensity distributions acquired at a large number of different wavelengths throughout as broad spectral range as possible. In practice, the various wavelengths can be realized using a broadband source with a

series of narrow spectral filters. It is also important to keep the spectral range as wide as possible. In our work, we performed such characterization throughout entire visible and near-IR regime. Generally, the spectral range is limited by the sensitivity of our imaging devices (cameras). Particularly interesting choices is related to the object of such studies. Taking into account our extensive experience with microspheres, we decided to use high-index barium titanate microspheres with various diameters as objects. They have index contrast about 2 in air which is too large to be described by Born approximation. They also have diameters on the order of several wavelengths, similar to Mie-particles. In the process of solving an inverse scattering problem using Klibanov's method, all these parameters of our objects should be considered unknown; however, we were able to compare the results of reconstruction of such unknown objects with their real parameters that was the main task of this thesis work.

6.2 Experimental Set Up and Results

Scattered images of microspheres were obtained at different narrow band frequency regions, from 400nm - 800nm. These images are intensity profiles having no phase information in the data. These images require an object with strong scattering properties as high-index microspheres where Born approximation might be difficult to be applicable, to place this object directly at the top of a sensor array.

The experimental set up uses several different optical components : microscope, detector, narrow band filters, see Figure 64. There are two distinct reasons as to why we chose to use a microscope: (1) observing microspheres that have been placed

directly onto the detector and (2) illuminating the microspheres for their imaging by Samsung Galaxy S3 cell phone camera. The narrow band filters allowed for a near monochromatic wave to illuminate the structure to acquire a scattered image from the microspheres, see Figure 64. The choice of the camera is for application purposes of miniaturization allowing for illumination through a set of narrow spectral filters covering as wide of a spectral range as possible. These images obtained are to test the algorithms of inverse scattering developed in Prof. Klibanov's group to reconstruct the spatial distribution of the real and imaginary part of the refractive index in our object in order to make a conclusion about the validity of the developed method.

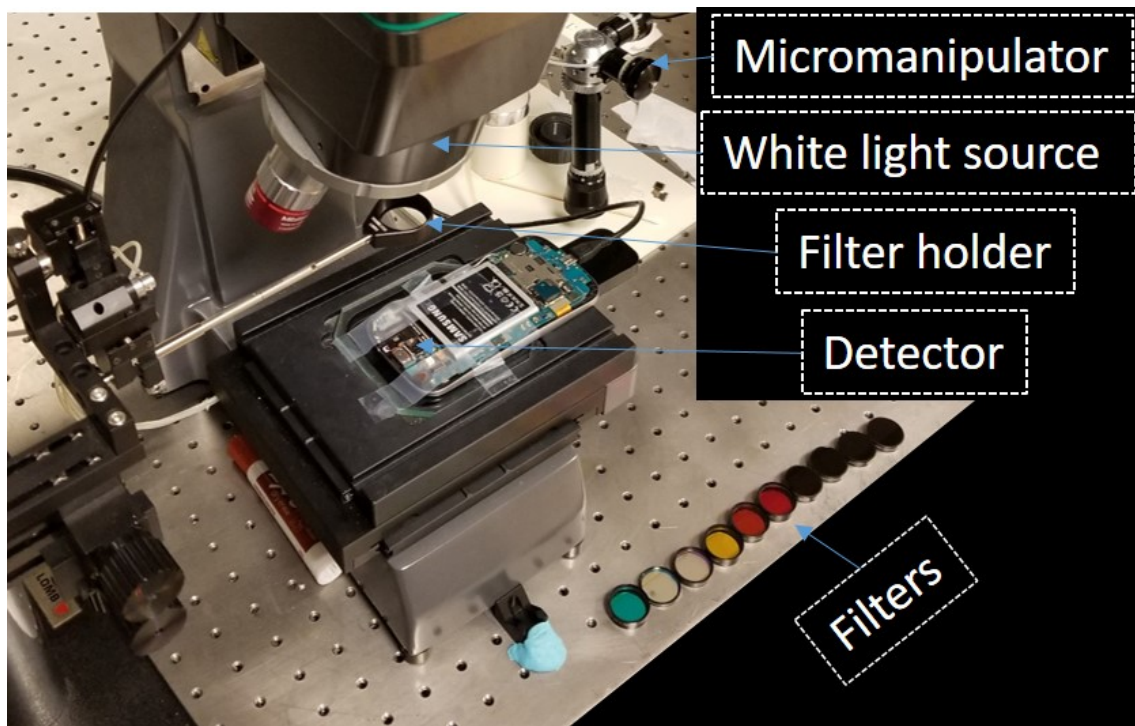


Figure 64: Picture showing the experimental set up.

The microscope that was used is a Mitutoyo upright microscope using an USHIO halogen projector lamp. This is used with no microscope objective to have a near plane wave illuminate the detector array. The microscope was also equipped with a

50x magnification long working distance objective which is used for observing microspheres that have been deposited directly onto the detector, see Figure 65.

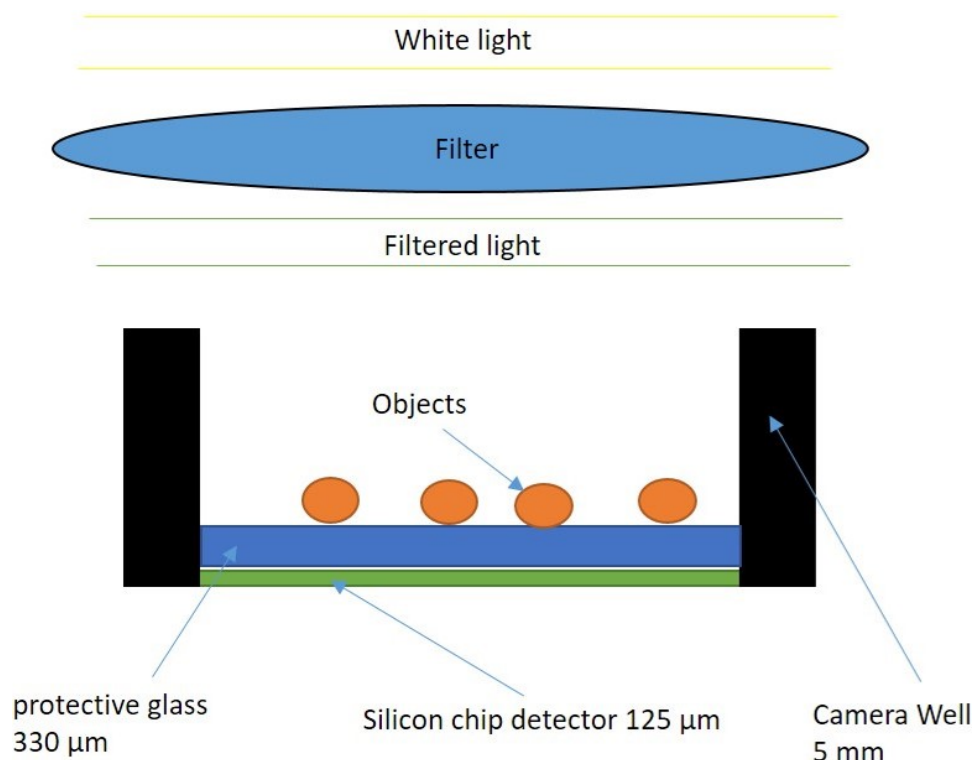


Figure 65: Schematic showing microspheres placed directly on the protective glass layer of the detector.

The Samsung Galaxy S3 camera, depicted above, is an 8 megapixel backside illuminated photodetector with a pixel size of $1.4 \mu\text{m}$ and a pitch of $1.5 \mu\text{m}$. This detector array has a layer of glass that is $330 \mu\text{m}$ in thickness placed directly above the mesa array. This layer of glass is to protect the detector array as well as act as a low-pass and high-pass filter; meaning that it limits the high and low frequency electromagnetic radiation to help protect the camera. The way we discovered this was on one camera we removed this protective glass layer which was directly on the sensor array and had a broader range of accepted frequencies the detector could detect over

when the glass layer was present.

The narrow band filters were used in order to limit the frequency of the light illuminating the detector array. This is because in the total wave field is dependent on the wavelength of illumination. Broadband illumination gives a far more complicated expression for the incident wave field and scattered wave field. The limiting of the frequency down to a near-monochromatic wave allows for computational methods to be used in order to solve the inverse scattering problem to recreate the location of the particle along with the refractive index of the object.

The objects that we have chosen to use are 1-20 μm microspheres placed directly onto the protective glass layer above the photodiodes. These microspheres were observed using the microscope and a 50x magnification far working distance objective. When a suitable microsphere or set of microsphere is found a 50 μm pinhole is micro manipulated between the objective and the camera. The objective is removed and the camera array is illuminated through the pinhole. This allows for more controllable positioning of the area of the detector array that we are interested in. Then the 50 μm pinhole is removed and different filters are placed in the optical path and images are acquired, see Figure 66.

6.3 Simulation Results

Alongside our collaborative team at the Department of Mathematics and Statistics at UNCC we put these images through their own algorithms for reconstruction of the real and imaginary part of the refractive index by solving an inverse scattering problem; in addition, we wanted to compare their results with a commercial product



Figure 66: Scattered image obtained using 473-, 525-, and 580-nm narrow band filter.

that numerically solves Maxwells equations, Lumerical. Two dimensional simulations were completed using this software with a plane wave incident on two circles of index of refraction of $n = 2.1$. This index matches the index of refraction of the microspheres that we used in the physical experiment. A $330 \mu\text{m}$ layer of material was placed directly behind the circles, this is to represent the protective glass layer. After speaking to the company, Samsung Group, the best information that we were able to obtain is that the index of refraction of this glass layer is $n = 1.5$, so we used this index for the simulation. Finally, a layer of silicon is simulated beneath this layer of glass. The scattered information is pulled directly from Lumerical software package. A plane wave is allowed to propagate from the source through this configuration and the resulting electric field map is shown in Figure 67 (c).

A detailed analysis between the photonics simulation using Lumerical and the 3d Phaseless Coefficient Inverse Problem (CIP), see Figure 68.

The inverse algorithm has very good agreement with the experimental results in terms of the refractive index and size of object that forms the scattered image. Lumerical does not have agreement with the experimental result and is far too noisy

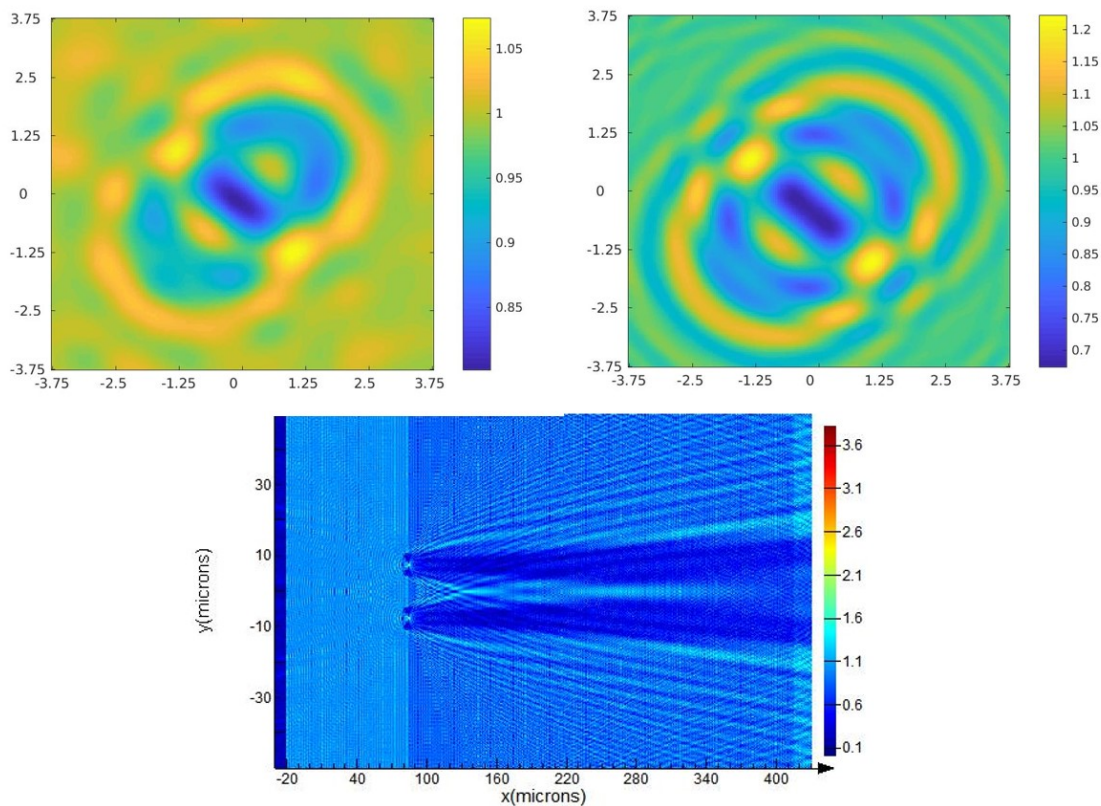


Figure 67: (a) Experimental results for inverse scattering experiments at 525nm (b) Prof. Michael Klivanov's algorithm result at 525nm. (c) Lumerical results at 525nm.

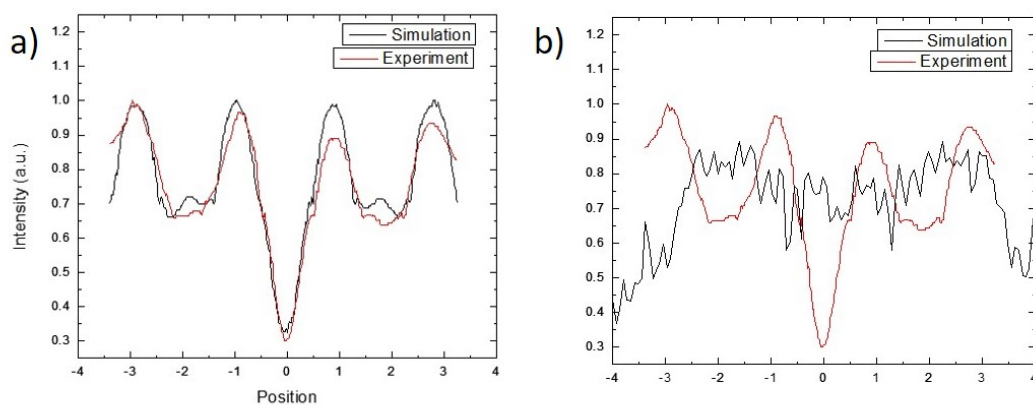


Figure 68: (a) Prof. Michael Klivanov's algorithm result at 525nm compared to the experimental result. (b) Lumerical results at 525nm compared to the experimental result.

to draw any conclusions.

6.4 Conclusion

In this Chapter we developed an experimental setup and performed the light scattering measurements aimed at testing 3d Phaseless Coefficient Inverse Problem algorithms. The choice of the object was dictated by a need to test the case of large index contrast in sizeable (several wavelengths) objects which are challenging for conventional inverse scattering reconstruction algorithms. Based on our previous experience with microspheres, we decided to use high-index barium titanate glass microbeads ($n \sim 2$) with several wavelengths in diameter. Different wavelengths were selected using a set of narrow spectral filters in combination with the broadband halogen lamp. The experiments were performed in the visible and near-IR spectral range using multiple advantages offered by the standard microscopes and cell phone camera in this spectral range.

The scattering patterns formed by high-index, $n = 2.1$, Barium-titanate glass microspheres with diameters $5.5 \mu\text{m} - 6.0 \mu\text{m}$ are measured using a set of narrow spectral filters.

This set illustrate an evolution of the scattering patterns with the wavelength. General trend is that the dimensions of the scattering images increasing with the wavelength which is an expected behavior based on a simplest diffraction theory. There are also more subtle variations with the wavelength inside the images of two microspheres which represent complicated diffraction and interference processes. Images obtained at 6 narrow spectral ranges centered at different wavelengths throughout the spectral

region from 400 nm - 800 nm were collected and sent to the collaborating group in the Department of Mathematics and Statistics at the University of North Carolina Charlotte.

These fine variations of the images with the wavelength serves as a basis for solving an inverse scattering problem. The direct scattering problem is solved for the reconstructed object in order to check the solution. Good agreement between the calculated and experimental scattering images is demonstrated based on the determined parameters of the microspheres.

Scattering pattern produced by the objects with dimensions similar to the microspheres used in the experiment were modeled in a simplified 2-D case using photonics software, Lumerical. The results showed somewhat different scattering patterns compared to 3-D case. The nature of these differences between 2-D numerical and 3-D analytical results can ascribed to differences between diffraction and interference phenomena in 2-D and 3-D cases.

CHAPTER 7: CONCLUSIONS AND FUTURE WORK

Super-resolution work represents an example where the fundamental principles of imaging based on structured illumination microscopy without postimaging processing are developed and they can be used in a broad range of applications. The general feature of such future work is based on the fact that microspherical nanoscopy provides 2-3 times better resolution compared to standard far-field diffraction-limited microscopy. This resolution advantage can be seen as relatively modest; however, it is important to recognize that many biomedical objects are just incrementally smaller than the diffraction limit, and for such objects the advantages offered by the microspherical nanoscopy are critical. One of the examples of such objects are subcellular structures. Typical biological cells have 5 to 10 μm dimensions observable in standard microscopy. In contrast, the subcellular structures have at least an order of magnitude smaller typical dimensions and very often the visibility of these structures is just at the border of what can be resolved in standard microscopy. Microspherical nanoscopy can offer a unique solution of this problem.

The embedding of high-index BTG microspheres into a rigid plastic slab allows for microspherical nanoscopy to be used for viscous solutions. The rigid slab along with nanoplasmonic arrays of Au allows for an increase in resolution ultimately the integration of the ideal nanoplasmonic structure along with dye doped biological structures and lead to the observation of subcellular structure with no post imaging

processing. It is important to note that the advanced super-resolution FL techniques such as STED or localization microscopy have higher resolution compared to microspherical nanoscopy, but have their own limitations. STED is scanning point-by-point method which is rather complicated in practical realization, especially in clinical environment. Localization microscopy is a wide field method, but it is also a rather slow method requiring taking multiple images, each subject to bleaching effects. In contrast, the microspherical nanoscopy is almost the same simple as standard microscopy.

All that is required for microspherical nanoscopy is a coverslip with embedded high-index microspheres and a substrate with nanoplasmonic array if extra resolution beyond the solid immersion lens limit is required. Due to its simplicity, the applications of microspherical nanoscopy can be developed for histological tissue analysis in a clinical environment in collaboration with the local hospitals. This technology can be also used for cellular studies in collaboration with Biology and Bioengineering departments for many different tasks. Besides the resolution, the advantage of this method is based on its inherently low intensity similar to conventional microscopy which reduces the damage to the tissue and bleaching effects. This also leads to a possibility to study biological processes in a real time scale which is important for many biomedical research tasks.

In the area of FPAs, the broader goal of our studies is to solve very important problems of MWIR and LWIR cameras related to the fact that the high-quality photon detectors are currently cryogenically cooled that increases the cost, weight, size, and power of these systems. The light-concentrating microstructures proposed in this

work will allow to reduce the dark current and to increase the operation temperature of these devices without corresponding reduction in the intensity and contrast of the optical images. This is a big task which will require significant development within the approaches proposed in the thesis work. It can be achieved step-by-step using designs with progressively smaller area of the base of the microcones with corresponding reduction in size of the photodetector mesas. This work will be developed in collaboration with the several groups at AFRL which have a strong interest in this technology.

Light-driven assembly of nanoplasmonic particles is of great research interest. Vast increases in the overall knowledge in the field of nonlinear phenomena if an understanding of the motions of these particles during the aggregation process can be known. This could ultimately lead to developing novel approaches to light-driven assembly of nanoparticles where the assembly is controlled by relatively low-level illumination through the meniscus of slowly evaporating liquid layer. The spatial resolution of these methods still require further studies. Another potentially interesting direction is represented by using nanoparticles with different shapes such as nanorods and studying how light-driven assembly changes its properties and geometrical characteristics for particles with different shapes.

For inverse scattering problems we have experimentally proven, in collaboration with the group of Prof. Klibanov, that it is possible to reconstruct 3-D object index of refraction and spatial location with great accuracy with a known phaseless scattered pattern. A big task remains in recreating an object shape. This can be done with more effort on getting more unique frequencies with a lower noise level detector.

REFERENCES

- [1] What is the marangoni effect? accessed 2018-03-25. <https://www.comsol.com/multiphysics/marangoni-effect>.
- [2] E. Abbe. Beiträge zur theorie des mikroskops und der mikroskopischen wahrnehmung. *Archiv für mikroskopische Anatomie*, 9(1):413–418, 1873.
- [3] F. Abolmaali, A. Brettin, A. Green, N. I. Limberopoulos, A. M. Urbas, and V. N. Astratov. Photonic jets for highly efficient mid-ir focal plane arrays with large angle-of-view. *Optics express*, 25(25):31174–31185, 2017.
- [4] F. Abolmaali, A. Brettin, N. I. Limberopoulos, A. M. Urbas, and V. N. Astratov. Use of photonic jets produced by dielectric microspheres for increasing sensitivity and angle-of-view of mwir detectors. In *Smart Photonic and Optoelectronic Integrated Circuits XIX*, volume 10107, page 101070V. International Society for Optics and Photonics, 2017.
- [5] M. G. Albrecht and J. A. Creighton. Anomalously intense raman spectra of pyridine at a silver electrode. *Journal of the american chemical society*, 99(15):5215–5217, 1977.
- [6] K. W. Allen, F. Abolmaali, J. M. Duran, G. Ariyawansa, N. I. Limberopoulos, A. M. Urbas, and V. N. Astratov. Increasing sensitivity and angle-of-view of mid-wave infrared detectors by integration with dielectric microspheres. *Applied Physics Letters*, 108(24):241108, 2016.
- [7] K. W. Allen, A. Darafsheh, F. Abolmaali, N. Mojaverian, N. I. Limberopoulos, A. Lupu, and V. N. Astratov. Microsphere-chain waveguides: Focusing and transport properties. *Applied Physics Letters*, 105(2):021112, 2014.
- [8] K. W. Allen, J. M. Duran, G. Ariyawansa, J. H. Vella, N. I. Limberopoulos, A. M. Urbas, and V. N. Astratov. Photonic jets for strained-layer superlattice infrared photodetector enhancement. In *Aerospace and Electronics Conference, NAECON 2014-IEEE National*, pages 32–33. IEEE, 2014.
- [9] K. W. Allen, N. Farahi, Y. Li, N. I. Limberopoulos, D. E. Walker, A. M. Urbas, and V. N. Astratov. Super-resolution imaging by arrays of high-index spheres embedded in transparent matrices. In *Aerospace and Electronics Conference, NAECON 2014-IEEE National*, pages 50–52. IEEE, 2014.
- [10] K. W. Allen, N. Farahi, Y. Li, N. I. Limberopoulos, D. E. Walker, A. M. Urbas, and V. N. Astratov. Overcoming the diffraction limit of imaging nanoplasmonic arrays by microspheres and microfibers. *Optics express*, 23(19):24484–24496, 2015.

- [11] K. W. Allen, N. Farahi, Y. Li, N. I. Limberopoulos, D. E. Walker Jr, A. M. Urbas, V. Liberman, and V. N. Astratov. Super-resolution microscopy by movable thin-films with embedded microspheres: resolution analysis. *Annalen der Physik*, 527(7-8):513–522, 2015.
- [12] K. W. Allen, A. F. Kosolapov, A. N. Kolyadin, A. D. Pryamikov, N. Mojaveharian, N. I. Limberopoulos, and V. N. Astratov. Photonic jets produced by microspheres integrated with hollow-core fibers for ultraprecise laser surgery. In *Transparent Optical Networks (ICTON), 2013 15th International Conference on*, pages 1–4. IEEE, 2013.
- [13] K. W. Allen, Y. Li, and V. N. Astratov. Reply to comment on super-resolution microscopy by movable thin-films with embedded microspheres: Resolution analysis[ann. phys.(berlin) 527, 513 (2015)]. *Annalen der Physik*, 528(11-12):901–904, 2016.
- [14] K. W. Allen Jr. Waveguide, photodetector, and imaging applications of microspherical photonics. *arXiv preprint arXiv:1503.03374*, 2015.
- [15] S. Arnold, M. Khoshshima, I. Teraoka, S. Holler, and F. Vollmer. Shift of whispering-gallery modes in microspheres by protein adsorption. *Optics letters*, 28(4):272–274, 2003.
- [16] S. Arnold and M. Lewittes. Size dependence of the photophoretic force. *Journal of Applied Physics*, 53(7):5314–5319, 1982.
- [17] S. Arnold, S. Shopova, and S. Holler. Whispering gallery mode bio-sensor for label-free detection of single molecules: thermo-optic vs. reactive mechanism. *Optics Express*, 18(1):281–287, 2010.
- [18] S. P. Ashili, V. N. Astratov, and E. C. H. Sykes. The effects of inter-cavity separation on optical coupling in dielectric bispheres. *Optics express*, 14(20):9460–9466, 2006.
- [19] A. Ashkin. Acceleration and trapping of particles by radiation pressure. *Physical review letters*, 24(4):156, 1970.
- [20] A. Ashkin. Optical trapping and manipulation of neutral particles using lasers. *Proceedings of the National Academy of Sciences*, 94(10):4853–4860, 1997.
- [21] V. Astratov, J. Franchak, and S. Ashili. Optical coupling and transport phenomena in chains of spherical dielectric microresonators with size disorder. *Applied Physics Letters*, 85(23):5508–5510, 2004.
- [22] V. Astratov, S. Yang, S. Lam, B. Jones, D. Sanvitto, D. Whittaker, A. Fox, M. Skolnick, A. Tahraoui, P. Fry, et al. Whispering gallery resonances in semiconductor micropillars. *Applied Physics Letters*, 91(7):071115, 2007.

- [23] V. N. Astratov. Fundamentals and applications of microsphere resonator circuits. In *Photonic Microresonator Research and Applications*, pages 423–457. Springer, 2010.
- [24] V. N. Astratov, F. Abolmaali, A. Brettin, K. W. Allen, A. V. Maslov, N. I. Limberopoulos, D. E. Walker, and A. M. Urbas. Label-free nanoscopy with contact microlenses: Super-resolution mechanisms and limitations. In *Transparent Optical Networks (ICTON), 2016 18th International Conference on*, pages 1–4. IEEE, 2016.
- [25] V. N. Astratov, K. W. Allen Jr, N. I. Limberopoulos, A. Urbas, and J. M. Duran. Photodetector focal plane array systems and methods, 2016. US Patent 9,362,324.
- [26] V. N. Astratov and S. P. Ashili. Percolation of light through whispering gallery modes in 3d lattices of coupled microspheres. *Optics Express*, 15(25):17351–17361, 2007.
- [27] V. N. Astratov, A. Brettin, F. Abolmaali, C. L. McGinnis, K. F. Blanchette, Y. E. Nesmelov, A. V. Maslov, N. I. Limberopoulos, D. E. Walker, and A. M. Urbas. Spotlight on microspherical nanoscopy: Experimental quantification of super-resolution. In *Transparent Optical Networks (ICTON), 2017 19th International Conference on*, pages 1–4. IEEE, 2017.
- [28] V. N. Astratov and A. Darafsheh. Methods and systems for super-resolution optical imaging using high-index of refraction microspheres and microcylinders, 2017. US Patent 9,726,874.
- [29] V. N. Astratov, A. Darafsheh, M. D. Kerr, K. W. Allen, N. M. Fried, A. N. Antoszyk, and H. S. Ying. Photonic nanojets for laser surgery. *SPIE Newsroom*, 12:32–34, 2010.
- [30] V. N. Astratov, Y. Li, O. V. Svitelskiy, A. V. Maslov, M. I. Bakunov, D. Carnegie, and E. Rafailov. Microspherical photonics: ultra-high resonant propulsion forces. *Optics and Photonics News*, 24(12):40–40, 2013.
- [31] V. N. Astratov, N. I. Limberopoulos, and A. M. Urbas. Super-resolution microscopy methods and systems enhanced by dielectric microspheres or microcylinders used in combination with metallic nanostructures, Dec. 5 2017. US Patent 9,835,870.
- [32] Y. Ben-Aryeh. Superresolution observed from evanescent waves transmitted through nano-corrugated metallic films. *Applied Physics B*, 109(1):165–170, 2012.
- [33] E. Betzig, G. H. Patterson, R. Sougrat, O. W. Lindwasser, S. Olenych, J. S. Bonifacino, M. W. Davidson, J. Lippincott-Schwartz, and H. F. Hess. Imaging intracellular fluorescent proteins at nanometer resolution. *Science*, 313(5793):1642–1645, 2006.

- [34] A. Bezryadina, J. Li, J. Zhao, A. Kothambawala, J. Ponsetto, E. Huang, J. Wang, and Z. Liu. Localized plasmonic structured illumination microscopy with an optically trapped microlens. *Nanoscale*, 9(39):14907–14912, 2017.
- [35] T. P. Bigioni, X.-M. Lin, T. T. Nguyen, E. I. Corwin, T. A. Witten, and H. M. Jaeger. Kinetically driven self assembly of highly ordered nanoparticle monolayers. *Nature materials*, 5(4):265, 2006.
- [36] G. Binnig and H. Rohrer. Scanning tunneling microscopy. *Surface science*, 126(1-3):236–244, 1983.
- [37] P. Bon, B. Rolly, N. Bonod, J. Wenger, B. Stout, S. Monneret, and H. Rigneault. Imaging the gouy phase shift in photonic jets with a wavefront sensor. *Optics letters*, 37(17):3531–3533, 2012.
- [38] A. Brettin, K. F. Blanchette, Y. Nesmelov, N. I. Limberopoulos, A. M. Urbas, and V. N. Astratov. Microsphere nanoscopy for imaging of actin proteins. In *Aerospace and Electronics Conference (NAECON) and Ohio Innovation Summit (OIS), 2016 IEEE National*, pages 269–271. IEEE, 2016.
- [39] A. Brettin, C. L. McGinnis, K. F. Blanchette, Y. E. Nesmelov, N. I. Limberopoulos, D. E. Walker, A. M. Urbas, and V. N. Astratov. Quantification of resolution in microspherical nanoscopy with biological objects. In *Aerospace and Electronics Conference (NAECON), 2017 IEEE National*, pages 189–192. IEEE, 2017.
- [40] M. M. Burns, J.-M. Fournier, and J. A. Golovchenko. Optical matter: crystallization and binding in intense optical fields. *Science*, 249(4970):749–754, 1990.
- [41] C. Chang, Y.-F. Wang, Y. Kanamori, J.-J. Shih, Y. Kawai, C.-K. Lee, K.-C. Wu, and M. Esashi. Etching submicrometer trenches by using the bosch process and its application to the fabrication of antireflection structures. *Journal of micromechanics and microengineering*, 15(3):580, 2005.
- [42] Z. Chen, H. Chu, and S. Li. Optical metrology using a photonic nanojet, 2008. US Patent 7,394,535.
- [43] Z. Chen, A. Taflove, and V. Backman. Photonic nanojet enhancement of backscattering of light by nanoparticles: a potential novel visible-light ultra-microscopy technique. *Optics express*, 12(7):1214–1220, 2004.
- [44] Z. Chen, A. Taflove, X. Li, and V. Backman. Superenhanced backscattering of light by nanoparticles. *Optics letters*, 31(2):196–198, 2006.
- [45] A. Chiasera, Y. Dumeige, P. Feron, M. Ferrari, Y. Jestin, G. Nunzi Conti, S. Pelli, S. Soria, and G. C. Righini. Spherical whispering-gallery-mode microresonators. *Laser & Photonics Reviews*, 4(3):457–482, 2010.

- [46] A. Clebsch. Ueber die reflexion an einer kugelfläche. *Journal für die reine und angewandte Mathematik*, 61:195–262, 1863.
- [47] X. Cui, D. Erni, and C. Hafner. Optical forces on metallic nanoparticles induced by a photonic nanojet. *Optics express*, 16(18):13560–13568, 2008.
- [48] A. Darafsheh and V. N. Astratov. Periodically focused modes in chains of dielectric spheres. *Applied physics letters*, 100(6):061123, 2012.
- [49] A. Darafsheh, A. Fardad, N. M. Fried, A. N. Antoszyk, H. S. Ying, and V. N. Astratov. Contact focusing multimodal microprobes for ultraprecise laser tissue surgery. *Optics Express*, 19(4):3440–3448, 2011.
- [50] A. Darafsheh, N. I. Limberopoulos, J. S. Derov, D. E. Walker Jr, and V. N. Astratov. Advantages of microsphere-assisted super-resolution imaging technique over solid immersion lens and confocal microscopies. *Applied Physics Letters*, 104(6):061117, 2014.
- [51] A. Darafsheh, N. Mojaverian, N. I. Limberopoulos, K. W. Allen, A. Lupu, and V. N. Astratov. Formation of polarized beams in chains of dielectric spheres and cylinders. *Optics letters*, 38(20):4208–4211, 2013.
- [52] A. Darafsheh, G. F. Walsh, L. Dal Negro, and V. N. Astratov. Optical super-resolution by high-index liquid-immersed microspheres. *Applied Physics Letters*, 101(14):141128, 2012.
- [53] J. Dave. *Subroutines for computing the parameters of the electromagnetic radiation scattered by a sphere*. IBM Palo Alto Scientific Center, 1968.
- [54] B.-J. de Gans, P. C. Duineveld, and U. S. Schubert. Inkjet printing of polymers: state of the art and future developments. *Advanced materials*, 16(3):203–213, 2004.
- [55] R. D. Deegan, O. Bakajin, T. F. Dupont, G. Huber, S. R. Nagel, and T. A. Witten. Contact line deposits in an evaporating drop. *Physical review E*, 62(1):756, 2000.
- [56] D. Deirmendjian, R. Clasen, and W. Viezee. Mie scattering with complex index of refraction. *JOSA*, 51(6):620–633, 1961.
- [57] S. Deng, W. Cai, and V. N. Astratov. Numerical study of light propagation via whispering gallery modes in microcylinder coupled resonator optical waveguides. *Optics express*, 12(26):6468–6480, 2004.
- [58] A. Devilez, N. Bonod, J. Wenger, D. Gérard, B. Stout, H. Rigneault, and E. Popov. Three-dimensional subwavelength confinement of light with dielectric microspheres. *Optics Express*, 17(4):2089–2094, 2009.

- [59] A. Devilez, B. Stout, N. Bonod, and E. Popov. Spectral analysis of three-dimensional photonic jets. *Optics Express*, 16(18):14200–14212, 2008.
- [60] J. A. Dieringer, A. D. McFarland, N. C. Shah, D. A. Stuart, A. V. Whitney, C. R. Yonzon, M. A. Young, X. Zhang, and R. P. Van Duyne. Introductory lecture surface enhanced raman spectroscopy: new materials, concepts, characterization tools, and applications. *Faraday discussions*, 132:9–26, 2006.
- [61] H. Ding, L. Dai, and C. Yan. Properties of the 3d photonic nanojet based on the refractive index of surroundings. *Chinese Optics Letters*, 8(7):706–708, 2010.
- [62] A. Doicu and T. Wriedt. Plane wave spectrum of electromagnetic beams. *Optics Communications*, 136(1-2):114–124, 1997.
- [63] R. G. Driggers, R. H. Vollmerhausen, J. P. Reynolds, J. D. Fanning, and G. C. Holst. Infrared detector size: how low should you go? *Optical Engineering*, 51(6):063202, 2012.
- [64] A. D’Souza, E. Robinson, A. Ionescu, D. Okerlund, T. De Lyon, R. Rajavel, H. Sharifi, N. Dhar, P. Wijewarnasuriya, and C. Grein. Mwir inassb barrier detector data and analysis. In *Infrared Technology and Applications XXXIX*, volume 8704, page 87041V. International Society for Optics and Photonics, 2013.
- [65] Y. Duan, G. Barbastathis, and B. Zhang. Classical imaging theory of a microlens with super-resolution. *Optics letters*, 38(16):2988–2990, 2013.
- [66] V. Dugas, G. Depret, Y. Chevalier, X. Nesme, and É. Souteyrand. Immobilization of single-stranded dna fragments to solid surfaces and their repeatable specific hybridization: covalent binding or adsorption? *Sensors and Actuators B: Chemical*, 101(1-2):112–121, 2004.
- [67] T. Elder and J. Strong. The infrared transmission of atmospheric windows. *Journal of the Franklin Institute*, 255(3):189–208, 1953.
- [68] P. Englebienne. Use of colloidal gold surface plasmon resonance peak shift to infer affinity constants from the interactions between protein antigens and antibodies specific for single or multiple epitopes. *Analyst*, 123(7):1599–1603, 1998.
- [69] N. Fang, H. Lee, C. Sun, and X. Zhang. Sub-diffraction-limited optical imaging with a silver superlens. *Science*, 308(5721):534–537, 2005.
- [70] P. Ferrand, J. Wenger, A. Devilez, M. Pianta, B. Stout, N. Bonod, E. Popov, and H. Rigneault. Direct imaging of photonic nanojets. *Optics express*, 16(10):6930–6940, 2008.
- [71] H. Fripp. On the limits of the optical capacity of the microscope. *Journal of Microscopy*, 16(1):15–39, 1876.

- [72] D. P. Fromm, A. Sundaramurthy, P. J. Schuck, G. Kino, and W. Moerner. Gap-dependent optical coupling of single bowtie nanoantennas resonant in the visible. *Nano letters*, 4(5):957–961, 2004.
- [73] D. B. Fullager, G. D. Boreman, and T. Hofmann. Infrared dielectric response of nanoscribe ip-dip and ip-l monomers after polymerization from 250 cm⁻¹ to 6000 cm⁻¹. *Optical Materials Express*, 7(3):888–894, 2017.
- [74] Y. E. Geints, E. Panina, and A. Zemlyanov. Control over parameters of photonic nanojets of dielectric microspheres. *Optics Communications*, 283(23):4775–4781, 2010.
- [75] Y. E. Geints, A. Zemlyanov, and E. Panina. Controlling the parameters of photon nanojets of composite microspheres. *Optics and Spectroscopy*, 109(4):590–595, 2010.
- [76] Y. E. Geints, A. A. Zemlyanov, and E. K. Panina. Photonic nanojet calculations in layered radially inhomogeneous micrometer-sized spherical particles. *JOSA B*, 28(8):1825–1830, 2011.
- [77] Y. E. Geints, A. A. Zemlyanov, and E. K. Panina. Photonic nanojet effect in multilayer micrometre-sized spherical particles. *Quantum Electronics*, 41(6):520–525, 2011.
- [78] Y. E. Geints, A. A. Zemlyanov, and E. K. Panina. Photonic jets from resonantly excited transparent dielectric microspheres. *JOSA B*, 29(4):758–762, 2012.
- [79] M. Gerlach, Y. P. Rakovich, and J. F. Donegan. Radiation-pressure-induced mode splitting in a spherical microcavity with an elastic shell. *Optics express*, 15(6):3597–3606, 2007.
- [80] R.-H. Giese. Die berechnung der lichtstreuung an kugelförmigen teilchen mit einem digitalrechner/the computation of light scattering on spherical particles by means of a digital computer. *it-Information Technology*, 3(1-6):240–245, 1961.
- [81] M. L. Gorodetsky and V. S. Ilchenko. Optical microsphere resonators: optimal coupling to high-q whispering-gallery modes. *JOSA B*, 16(1):147–154, 1999.
- [82] P. J. Goulet and R. F. Aroca. Surface-enhancement of fluorescence near noble metal nanostructures. In *Radiative Decay Engineering*, pages 223–247. Springer, 2005.
- [83] M. Groner, J. Elam, F. Fabreguette, and S. M. George. Electrical characterization of thin al₂o₃ films grown by atomic layer deposition on silicon and various metal substrates. *Thin Solid Films*, 413(1-2):186–197, 2002.

- [84] H. Guo, Y. Han, X. Weng, Y. Zhao, G. Sui, Y. Wang, and S. Zhuang. Near-field focusing of the dielectric microsphere with wavelength scale radius. *Optics Express*, 21(2):2434–2443, 2013.
- [85] M. G. Gustafsson. Surpassing the lateral resolution limit by a factor of two using structured illumination microscopy. *Journal of microscopy*, 198(2):82–87, 2000.
- [86] M. G. Gustafsson, L. Shao, P. M. Carlton, C. R. Wang, I. N. Golubovskaya, W. Z. Cande, D. A. Agard, and J. W. Sedat. Three-dimensional resolution doubling in wide-field fluorescence microscopy by structured illumination. *Biophysical journal*, 94(12):4957–4970, 2008.
- [87] A. J. Haes, L. Chang, W. L. Klein, and R. P. Van Duyne. Detection of a biomarker for alzheimer’s disease from synthetic and clinical samples using a nanoscale optical biosensor. *Journal of the American Chemical Society*, 127(7):2264–2271, 2005.
- [88] A. J. Haes, C. L. Haynes, A. D. McFarland, G. C. Schatz, R. P. Van Duyne, and S. Zou. Plasmonic materials for surface-enhanced sensing and spectroscopy. *MRS bulletin*, 30(5):368–375, 2005.
- [89] A. J. Haes and R. P. Van Duyne. A unified view of propagating and localized surface plasmon resonance biosensors. *Analytical and bioanalytical chemistry*, 379(7-8):920–930, 2004.
- [90] A. J. Haes, S. Zou, G. C. Schatz, and R. P. Van Duyne. Nanoscale optical biosensor: short range distance dependence of the localized surface plasmon resonance of noble metal nanoparticles. *The Journal of Physical Chemistry B*, 108(22):6961–6968, 2004.
- [91] A. J. Haes, S. Zou, G. C. Schatz, and R. P. Van Duyne. A nanoscale optical biosensor: the long range distance dependence of the localized surface plasmon resonance of noble metal nanoparticles. *The Journal of Physical Chemistry B*, 108(1):109–116, 2004.
- [92] K. Hamamoto, R. Micheletto, M. Oyama, A. A. Umar, S. Kawai, and Y. Kawakami. An original planar multireflection system for sensing using the local surface plasmon resonance of gold nanospheres. *Journal of Optics A: Pure and Applied Optics*, 8(3):268, 2006.
- [93] X. Hao, C. Kuang, Z. Gu, Y. Wang, S. Li, Y. Ku, Y. Li, J. Ge, and X. Liu. From microscopy to nanoscopy via visible light. *Light: Science & Applications*, 2(10):e108, 2013.
- [94] X. Hao, C. Kuang, X. Liu, H. Zhang, and Y. Li. Microsphere based microscope with optical super-resolution capability. *Applied Physics Letters*, 99(20):203102, 2011.

- [95] X. Hao, X. Liu, C. Kuang, Y. Li, Y. Ku, H. Zhang, H. Li, and L. Tong. Far-field super-resolution imaging using near-field illumination by micro-fiber. *Applied Physics Letters*, 102(1):013104, 2013.
- [96] M. Hasan and J. J. Simpson. Three-dimensional subwavelength confinement of a photonic nanojet using a plasmonic nanoantenna gap. *Microwave and Optical Technology Letters*, 56(11):2700–2706, 2014.
- [97] C. L. Haynes, A. D. McFarland, M. T. Smith, J. C. Hulteen, and R. P. Van Duyne. Angle-resolved nanosphere lithography: manipulation of nanoparticle size, shape, and interparticle spacing. *The Journal of Physical Chemistry B*, 106(8):1898–1902, 2002.
- [98] C. L. Haynes and R. P. Van Duyne. Nanosphere lithography: a versatile nanofabrication tool for studies of size-dependent nanoparticle optics, 2001.
- [99] C. L. Haynes and R. P. Van Duyne. Plasmon-sampled surface-enhanced raman excitation spectroscopy. *The Journal of Physical Chemistry B*, 107(30):7426–7433, 2003.
- [100] C. L. Haynes, C. R. Yonzon, X. Zhang, and R. P. Van Duyne. Surface-enhanced raman sensors: early history and the development of sensors for quantitative biowarfare agent and glucose detection. *Journal of Raman Spectroscopy*, 36(6-7):471–484, 2005.
- [101] E. Hecht. *Optics*. Pearson Education, 2016.
- [102] A. Heifetz, S.-C. Kong, A. V. Sahakian, A. Taflove, and V. Backman. Photonic nanojets. *Journal of computational and theoretical nanoscience*, 6(9):1979–1992, 2009.
- [103] A. Heifetz, J. J. Simpson, S.-C. Kong, A. Taflove, and V. Backman. Subdiffraction optical resolution of a gold nanosphere located within the nanojet of a mie-resonant dielectric microsphere. *Optics Express*, 15(25):17334–17342, 2007.
- [104] B. Hein, K. I. Willig, and S. W. Hell. Stimulated emission depletion (sted) nanoscopy of a fluorescent protein-labeled organelle inside a living cell. *Proceedings of the National Academy of Sciences*, 105(38):14271–14276, 2008.
- [105] S. W. Hell and J. Wichmann. Breaking the diffraction resolution limit by stimulated emission: stimulated-emission-depletion fluorescence microscopy. *Optics letters*, 19(11):780–782, 1994.
- [106] E. M. Hicks, S. Zou, G. C. Schatz, K. G. Spears, R. P. Van Duyne, L. Gunnarsson, T. Rindzevicius, B. Kasemo, and M. Käll. Controlling plasmon line shapes through diffractive coupling in linear arrays of cylindrical nanoparticles fabricated by electron beam lithography. *Nano letters*, 5(6):1065–1070, 2005.

- [107] K. R. Hiremath and V. N. Astratov. Perturbations of whispering gallery modes by nanoparticles embedded in microcavities. *Optics express*, 16(8):5421–5426, 2008.
- [108] G. C. Holst. Imaging system performance based upon $f\lambda/d$. *Optical Engineering*, 46(10):103204, 2007.
- [109] G. C. Holst and R. G. Driggers. Small detectors in infrared system design. *Optical Engineering*, 51(9):096401, 2012.
- [110] W. V. Houston. A compound interferometer for fine structure work. *Physical Review*, 29(3):478, 1927.
- [111] X. Huang, X. He, W. Xiong, Y. Gao, L. Jiang, L. Liu, Y. Zhou, L. Jiang, J. Silvain, and Y. Lu. Contrast enhancement using silica microspheres in coherent anti-stokes raman spectroscopic imaging. *Optics Express*, 22(3):2889–2896, 2014.
- [112] J. C. Hulteen and R. P. Van Duyne. Nanosphere lithography: A materials general fabrication process for periodic particle array surfaces. *Journal of Vacuum Science & Technology A: Vacuum, Surfaces, and Films*, 13(3):1553–1558, 1995.
- [113] T. C. Hutchens, A. Darafsheh, V. N. Astratov, N. M. Fried, A. Fardad, A. N. Antoszyk, and H. S. Ying. Characterization of novel microsphere chain fiber optic tips for potential use in ophthalmic laser surgery. *Journal of Biomedical Optics*, 17(6):068004, 2012.
- [114] T. C. Hutchens, A. Darafsheh, A. Fardad, A. N. Antoszyk, H. S. Ying, V. N. Astratov, and N. M. Fried. Detachable microsphere scalpel tips for potential use in ophthalmic surgery with the erbium: Yag laser. *Journal of Biomedical Optics*, 19(1):018003, 2014.
- [115] V. Ilchenko, P. Volikov, V. Velichansky, F. Treussart, V. Lefevre-Seguin, J.-M. Raimond, and S. Haroche. Strain-tunable high-q optical microsphere resonator. *Optics communications*, 145(1-6):86–90, 1998.
- [116] V. S. Ilchenko and A. B. Matsko. Optical resonators with whispering-gallery modes-part i: Basics. *IEEE Journal of selected topics in quantum electronics*, 12(1):3–14, 2006.
- [117] V. S. Ilchenko and A. B. Matsko. Optical resonators with whispering-gallery modes-part ii: applications. *IEEE Journal of selected topics in quantum electronics*, 12(1):15–32, 2006.
- [118] A. Itagi and W. Challener. Optics of photonic nanojets. *JOSA A*, 22(12):2847–2858, 2005.
- [119] T. Jalali and D. Erni. Highly confined photonic nanojet from elliptical particles. *Journal of Modern Optics*, 61(13):1069–1076, 2014.

- [120] D. L. Jeanmaire and R. P. Van Duyne. Surface raman spectroelectrochemistry: Part i. heterocyclic, aromatic, and aliphatic amines adsorbed on the anodized silver electrode. *Journal of electroanalytical chemistry and interfacial electrochemistry*, 84(1):1–20, 1977.
- [121] T. R. Jensen, M. L. Duval, K. L. Kelly, A. A. Lazarides, G. C. Schatz, and R. P. Van Duyne. Nanosphere lithography: effect of the external dielectric medium on the surface plasmon resonance spectrum of a periodic array of silver nanoparticles. *The Journal of Physical Chemistry B*, 103(45):9846–9853, 1999.
- [122] B. D. Jones, M. Oxborrow, V. N. Astratov, M. Hopkinson, A. Tahraoui, M. Skolnick, and A. Fox. Splitting and lasing of whispering gallery modes in quantum dot micropillars. *Optics express*, 18(21):22578–22592, 2010.
- [123] A. V. Kanaev, V. N. Astratov, and W. Cai. Optical coupling at a distance between detuned spherical cavities. *Applied physics letters*, 88(11):111111, 2006.
- [124] A. Kapitonov and V. Astratov. Observation of nanojet-induced modes with small propagation losses in chains of coupled spherical cavities. *Optics letters*, 32(4):409–411, 2007.
- [125] D. Kaya, V. Belyi, and M. Muthukumar. Pattern formation in drying droplets of polyelectrolyte and salt. *The Journal of chemical physics*, 133(11):114905, 2010.
- [126] K. L. Kelly, E. Coronado, L. L. Zhao, and G. C. Schatz. The optical properties of metal nanoparticles: the influence of size, shape, and dielectric environment, 2003.
- [127] P. G. Kik, S. A. Maier, and H. A. Atwater. Surface plasmons for nanofabrication. In *Micromachining Technology for Micro-Optics and Nano-Optics II*, volume 5347, pages 215–224. International Society for Optics and Photonics, 2003.
- [128] M.-S. Kim, T. Scharf, S. Mühlig, C. Rockstuhl, and H. P. Herzig. Engineering photonic nanojets. *Optics Express*, 19(11):10206–10220, 2011.
- [129] M.-S. Kim, T. Scharf, S. Mühlig, C. Rockstuhl, and H. P. Herzig. Gouy phase anomaly in photonic nanojets. *Applied Physics Letters*, 98(19):191114, 2011.
- [130] M. A. Kinch. *Fundamentals of infrared detector materials*, volume 190. SPIE press Bellingham, 2007.
- [131] M. A. Kinch. The rationale for ultra-small pitch ir systems. In *Infrared Technology and Applications XL*, volume 9070, page 907032. International Society for Optics and Photonics, 2014.
- [132] M. A. Kinch. *State-of-the-art infrared detector technology*. SPIE press Bellingham, 2014.

- [133] A. D. Kiselev and D. O. Plutenko. Mie scattering of laguerre-gaussian beams: Photonic nanojets and near-field optical vortices. *Physical Review A*, 89(4):043803, 2014.
- [134] M. V. Klibanov, N. A. Koshev, D.-L. Nguyen, L. H. Nguyen, A. Brettin, and V. N. Astratov. A numerical method to solve a phaseless coefficient inverse problem from a single measurement of experimental data. *arXiv preprint arXiv:1803.01374*, 2018.
- [135] K. Kneipp, Y. Wang, R. R. Dasari, and M. S. Feld. Approach to single molecule detection using surface-enhanced resonance raman scattering (serrs): A study using rhodamine 6g on colloidal silver. *applied spectroscopy*, 49(6):780–784, 1995.
- [136] J. C. Knight, G. Cheung, F. Jacques, and T. Birks. Phase-matched excitation of whispering-gallery-mode resonances by a fiber taper. *Optics letters*, 22(15):1129–1131, 1997.
- [137] S.-C. Kong, A. Sahakian, A. Taflove, and V. Backman. Photonic nanojet-enabled optical data storage. *Optics express*, 16(18):13713–13719, 2008.
- [138] S.-C. Kong, A. Taflove, and V. Backman. Quasi one-dimensional light beam generated by a graded-index microsphere. *Optics Express*, 17(5):3722–3731, 2009.
- [139] S.-C. Kong, A. Taflove, and V. Backman. Quasi one-dimensional light beam generated by a graded-index microsphere: errata. *Optics Express*, 18(4):3973–3973, 2010.
- [140] L. A. Krivitsky, J. J. Wang, Z. Wang, and B. Luk'yanchuk. Locomotion of microspheres for super-resolution imaging. *Scientific reports*, 3:3501, 2013.
- [141] C. Lam, P. T. Leung, and K. Young. Explicit asymptotic formulas for the positions, widths, and strengths of resonances in mie scattering. *JOSA B*, 9(9):1585–1592, 1992.
- [142] B. Lamprecht, G. Schider, R. Lechner, H. Ditlbacher, J. Krenn, A. Leitner, and F. Aussenegg. Metal nanoparticle gratings: influence of dipolar particle interaction on the plasmon resonance. *Physical review letters*, 84(20):4721, 2000.
- [143] S. Lecler, S. Haacke, N. Lecong, O. Crégut, J.-L. Rehspringer, and C. Hirlimann. Photonic jet driven non-linear optics: example of two-photon fluorescence enhancement by dielectric microspheres. *Optics express*, 15(8):4935–4942, 2007.
- [144] S. Lecler, Y. Takakura, and P. Meyrueis. Properties of a three-dimensional photonic jet. *Optics letters*, 30(19):2641–2643, 2005.

- [145] S. Lee, L. Li, Y. Ben-Aryeh, Z. Wang, and W. Guo. Overcoming the diffraction limit induced by microsphere optical nanoscopy. *Journal of Optics*, 15(12):125710, 2013.
- [146] S. Lee, L. Li, and Z. Wang. Optical resonances in microsphere photonic nanojets. *Journal of Optics*, 16(1):015704, 2013.
- [147] S. Lee, L. Li, Z. Wang, W. Guo, Y. Yan, and T. Wang. Immersed transparent microsphere magnifying sub-diffraction-limited objects. *Applied optics*, 52(30):7265–7270, 2013.
- [148] C. Li, G. Skidmore, C. Howard, E. Clarke, and C. Han. Advancement in 17-micron pixel pitch uncooled focal plane arrays. In *Infrared Technology and Applications XXXV*, volume 7298, page 72980S. International Society for Optics and Photonics, 2009.
- [149] J. Li, B. Cabane, M. Sztucki, J. Gummel, and L. Goehring. Drying dip-coated colloidal films. *Langmuir*, 28(1):200–208, 2011.
- [150] L. Li, W. Guo, Y. Yan, S. Lee, and T. Wang. Label-free super-resolution imaging of adenoviruses by submerged microsphere optical nanoscopy. *Light: Science & Applications*, 2(9):e104, 2013.
- [151] X. Li, Z. Chen, A. Taflove, and V. Backman. Optical analysis of nanoparticles via enhanced backscattering facilitated by 3-d photonic nanojets. *Optics Express*, 13(2):526–533, 2005.
- [152] Y. Li, F. Abolmaali, K. W. Allen, N. I. Limberopoulos, A. Urbas, Y. Rakovich, A. V. Maslov, and V. N. Astratov. Whispering gallery mode hybridization in photonic molecules. *Laser & Photonics Reviews*, 11(2):1600278, 2017.
- [153] Y. Li, A. V. Maslov, N. I. Limberopoulos, A. M. Urbas, and V. N. Astratov. Spectrally resolved resonant propulsion of dielectric microspheres. *Laser & Photonics Reviews*, 9(2):263–273, 2015.
- [154] Y. Li, O. V. Svitelskiy, A. V. Maslov, D. Carnegie, E. Rafailov, and V. N. Astratov. Giant resonant light forces in microspherical photonics. *Light: Science & Applications*, 2(4):e64, 2013.
- [155] V. Liberman, M. Rothschild, O. Bakr, and F. Stellacci. Optical limiting with complex plasmonic nanoparticles. *Journal of Optics*, 12(6):065001, 2010.
- [156] V. Liberman, M. Sworin, R. Kingsborough, G. Geurtsen, and M. Rothschild. Nonlinear bleaching, absorption, and scattering of 532-nm-irradiated plasmonic nanoparticles. *Journal of Applied Physics*, 113(5):053107, 2013.
- [157] V. Liberman, M. Sworin, R. Kingsborough, K. Hamad, A. Swiston, G. Geurtsen, and M. Rothschild. Nonlinear optical properties of plasmonic nanoparticles: The influence of material, size, shape and solvent. In *CLEO: QELS_Fundamental Science*, pages QTh3E–3. Optical Society of America, 2013.

- [158] Y.-H. Lin and D. P. Tsai. Near-field scanning optical microscopy using a super-resolution cover glass slip. *Optics Express*, 20(15):16205–16211, 2012.
- [159] A. Lipson, S. G. Lipson, and H. Lipson. *Optical physics*. Cambridge University Press, 2010.
- [160] C.-Y. Liu and Y.-H. Wang. Real-space observation of photonic nanojet in dielectric microspheres. *Physica E: Low-dimensional Systems and Nanostructures*, 61:141–147, 2014.
- [161] Y. Liu, B. Wang, and Z. Ding. Influence of incident light polarization on photonic nanojet. *Chinese Optics Letters*, 9(7):072901–072901, 2011.
- [162] Z. Liu, S. Durant, H. Lee, Y. Pikus, N. Fang, Y. Xiong, C. Sun, and X. Zhang. Far-field optical superlens. *Nano Letters*, 7(2):403–408, 2007.
- [163] Z. Liu, H. Lee, Y. Xiong, C. Sun, and X. Zhang. Far-field optical hyperlens magnifying sub-diffraction-limited objects. *science*, 315(5819):1686–1686, 2007.
- [164] L. Lorenz. *Lysbevægelsen i og uden for en af plane Lysbølger belyst Kugle*. na, 1890.
- [165] T. Lu, H. Lee, T. Chen, S. Herchak, J.-H. Kim, S. E. Fraser, R. C. Flagan, and K. Vahala. High sensitivity nanoparticle detection using optical microcavities. *Proceedings of the National Academy of Sciences*, 108(15):5976–5979, 2011.
- [166] B. Lukyanchuk, N. Arnold, S. Huang, Z. Wang, and M. Hong. Three-dimensional effects in dry laser cleaning. *Applied Physics A*, 77(2):209–215, 2003.
- [167] B. S. Luk'yanchuk, Y. W. Zheng, and Y. Lu. Laser cleaning of solid surface: optical resonance and near-field effects. In *High-Power Laser Ablation III*, volume 4065, pages 576–588. International Society for Optics and Photonics, 2000.
- [168] I. Mahariq, V. N. Astratov, and H. Kurt. Persistence of photonic nanojet formation under the deformation of circular boundary. *JOSA B*, 33(4):535–542, 2016.
- [169] A. Manissadjian, L. Rubaldo, Y. Rebeil, A. Kerlain, D. Brellier, and L. Mollard. Improved ir detectors to swap heavy systems for swap. In *Infrared Technology and Applications XXXVIII*, volume 8353, page 835334. International Society for Optics and Photonics, 2012.
- [170] A. Maslov, V. Astratov, and M. Bakunov. Resonant propulsion of a microparticle by a surface wave. *Physical Review A*, 87(5):053848, 2013.
- [171] A. V. Maslov and V. N. Astratov. Microspherical photonics: Sorting resonant photonic atoms by using light. *Applied Physics Letters*, 105(12):121113, 2014.

- [172] A. V. Maslov and V. N. Astratov. Imaging of sub-wavelength structures radiating coherently near microspheres. *Applied Physics Letters*, 108(5):051104, 2016.
- [173] A. V. Maslov and V. N. Astratov. Optical nanoscopy with contact mie-particles: Resolution analysis. *Applied Physics Letters*, 110(26):261107, 2017.
- [174] A. Matsko, A. Savchenkov, D. Strekalov, V. Ilchenko, and L. Maleki. Review of applications of whispering-gallery mode resonators in photonics and nonlinear optics. *IPN Progress Report*, 42(162):1–51, 2005.
- [175] T. Matsui and A. Okajima. Finite-difference time-domain analysis of photonic nanojets from liquid-crystal-containing microcylinder. *Japanese Journal of Applied Physics*, 53(1S):01AE04, 2013.
- [176] S. McCall, A. Levi, R. Slusher, S. Pearton, and R. Logan. Whispering-gallery mode microdisk lasers. *Applied physics letters*, 60(3):289–291, 1992.
- [177] D. McCloskey, J. J. Wang, and J. Donegan. Low divergence photonic nanojets from si 3 n 4 microdisks. *Optics Express*, 20(1):128–140, 2012.
- [178] A. D. McFarland and R. P. Van Duyne. Single silver nanoparticles as real-time optical sensors with zeptomole sensitivity. *Nano letters*, 3(8):1057–1062, 2003.
- [179] A. D. McFarland, M. A. Young, J. A. Dieringer, and R. P. Van Duyne. Wavelength-scanned surface-enhanced raman excitation spectroscopy. *The Journal of Physical Chemistry B*, 109(22):11279–11285, 2005.
- [180] G. Mie. Beiträge zur optik trüber medien, speziell kolloidaler metallösungen. *Annalen der physik*, 330(3):377–445, 1908.
- [181] M. M. Miller and A. A. Lazarides. Sensitivity of metal nanoparticle surface plasmon resonance to the dielectric environment. *The Journal of Physical Chemistry B*, 109(46):21556–21565, 2005.
- [182] M. S. Miller, G. J. Davidson, and T. B. Carmichael. Templated self-assembly of glass microspheres into ordered two-dimensional arrays under dry conditions. *Langmuir*, 26(7):5286–5290, 2009.
- [183] M. Moskovits. Surface roughness and the enhanced intensity of raman scattering by molecules adsorbed on metals. *The Journal of Chemical Physics*, 69(9):4159–4161, 1978.
- [184] J. R. Nagel and M. A. Scarpulla. Enhanced absorption in optically thin solar cells by scattering from embedded dielectric nanoparticles. *Optics express*, 18(102):A139–A146, 2010.
- [185] C. L. Nehl, H. Liao, and J. H. Hafner. Optical properties of star-shaped gold nanoparticles. *Nano letters*, 6(4):683–688, 2006.

- [186] S. Nie and S. R. Emory. Probing single molecules and single nanoparticles by surface-enhanced raman scattering. *science*, 275(5303):1102–1106, 1997.
- [187] P. Nussbaum, R. Voelkel, H. P. Herzig, M. Eisner, and S. Haselbeck. Design, fabrication and testing of microlens arrays for sensors and microsystems. *Pure and applied optics: Journal of the European optical society part A*, 6(6):617, 1997.
- [188] A. N. Oraevsky. Whispering-gallery waves. *Quantum electronics*, 32(5):377–400, 2002.
- [189] J. Park and J. Moon. Control of colloidal particle deposit patterns within picoliter droplets ejected by ink-jet printing. *Langmuir*, 22(8):3506–3513, 2006.
- [190] J. B. Pendry. Negative refraction makes a perfect lens. *Physical review letters*, 85(18):3966, 2000.
- [191] G. Raschke, S. Kowarik, T. Franzl, C. Sönnichsen, T. Klar, J. Feldmann, A. Nichtl, and K. Kürzinger. Biomolecular recognition based on single gold nanoparticle light scattering. *Nano letters*, 3(7):935–938, 2003.
- [192] L. Rayleigh. Xxxi. investigations in optics, with special reference to the spectroscope. *The London, Edinburgh, and Dublin Philosophical Magazine and Journal of Science*, 8(49):261–274, 1879.
- [193] G. Righini, Y. Dumeige, P. Féron, M. Ferrari, G. Nunzi Conti, D. Ristic, and S. Soria. Whispering gallery mode microresonators: fundamentals and applications. *Rivista del Nuovo Cimento*, 34(7):435–488, 2011.
- [194] M. Ritala et al. Atomic layer deposition in handbook of thin film materials, 2001, vol. 1, chapter 2.
- [195] A. Rogalski. Infrared detectors: an overview. *Infrared Physics & Technology*, 43(3-5):187–210, 2002.
- [196] A. Rogalski. History of infrared detectors. *Opto-Electronics Review*, 20(3):279–308, 2012.
- [197] A. Rogalski, P. Martyniuk, and M. Kopytko. Challenges of small-pixel infrared detectors: a review. *Reports on Progress in Physics*, 79(4):046501, 2016.
- [198] D. Rugar and P. Hansma. Atomic force microscopy. *Physics today*, 43(10):23–30, 1990.
- [199] M. J. Rust, M. Bates, and X. Zhuang. Sub-diffraction-limit imaging by stochastic optical reconstruction microscopy (storm). *Nature methods*, 3(10):793, 2006.
- [200] B. Sandnes, T. A. Kelf, H. Liu, and A. V. Zvyagin. Retroemission by a glass bead monolayer for high-sensitivity, long-range imaging of upconverting phosphors. *Optics letters*, 36(15):3009–3011, 2011.

- [201] R. Savino, D. Paterna, and N. Favaloro. Buoyancy and marangoni effects in an evaporating drop. *Journal of thermophysics and heat transfer*, 16(4):562–574, 2002.
- [202] G. C. Schatz, M. A. Young, and R. P. Van Duyne. Electromagnetic mechanism of sers. In *Surface-enhanced Raman scattering*, pages 19–45. Springer, 2006.
- [203] S. Schiller and R. L. Byer. High-resolution spectroscopy of whispering gallery modes in large dielectric spheres. *Optics Letters*, 16(15):1138–1140, 1991.
- [204] L. J. Sherry, S.-H. Chang, G. C. Schatz, R. P. Van Duyne, B. J. Wiley, and Y. Xia. Localized surface plasmon resonance spectroscopy of single silver nanocubes. *Nano letters*, 5(10):2034–2038, 2005.
- [205] H. Shroff, C. G. Galbraith, J. A. Galbraith, and E. Betzig. Live-cell photoactivated localization microscopy of nanoscale adhesion dynamics. *Nature methods*, 5(5):417, 2008.
- [206] D. D. Smith, Y. Yoon, R. W. Boyd, J. K. Campbell, L. A. Baker, R. M. Crooks, and M. George. Z-scan measurement of the nonlinear absorption of a thin gold film. *Journal of applied physics*, 86(11):6200–6205, 1999.
- [207] C. M. Sparrow. On spectroscopic resolving power. *The Astrophysical Journal*, 44:76, 1916.
- [208] W. Srituravanich, N. Fang, C. Sun, Q. Luo, and X. Zhang. Plasmonic nanolithography. *Nano letters*, 4(6):1085–1088, 2004.
- [209] T. Still, P. J. Yunker, and A. G. Yodh. Surfactant-induced marangoni eddies alter the coffee-rings of evaporating colloidal drops. *Langmuir*, 28(11):4984–4988, 2012.
- [210] H. STRZELECKA-GOLASZEWSKA, E. PRÓCHNIEWICZ, E. NOWAK, S. Zmorzynski, and W. Drabikowski. Chicken-gizzard actin: Polymerization and stability. *The FEBS Journal*, 104(1):41–52, 1980.
- [211] A. Sundaramurthy, P. J. Schuck, N. R. Conley, D. P. Fromm, G. S. Kino, and W. Moerner. Toward nanometer-scale optical photolithography: utilizing the near-field of bowtie optical nanoantennas. *Nano letters*, 6(3):355–360, 2006.
- [212] O. Svitelskiy, Y. Li, A. Darafsheh, M. Sumetsky, D. Carnegie, E. Rafailov, and V. N. Astratov. Fiber coupling to batio 3 glass microspheres in an aqueous environment. *Optics letters*, 36(15):2862–2864, 2011.
- [213] O. Svitelskiy, D. Sun, A. Darafsheh, M. Sumetsky, A. Lupu, M. Tchernycheva, and V. N. Astratov. Characterization of high index microsphere resonators in fiber-integrated microfluidic platforms. In *Laser Resonators and Beam Control XIII*, volume 7913, page 791314. International Society for Optics and Photonics, 2011.

- [214] A. M. Sydor, K. J. Czymmek, E. M. Puchner, and V. Mennella. Super-resolution microscopy: from single molecules to supramolecular assemblies. *Trends in cell biology*, 25(12):730–748, 2015.
- [215] A. Taflove and S. C. Hagness. *Computational electrodynamics: the finite-difference time-domain method*. Artech house, 2005.
- [216] C. F. Tung and J. A. Laird. Transparent glass microspheres and products made therefrom, Mar. 23 1976. US Patent 3,946,130.
- [217] K. J. Vahala. Optical microcavities. *nature*, 424(6950):839, 2003.
- [218] N. Venkatram, D. N. Rao, and M. Akundi. Nonlinear absorption, scattering and optical limiting studies of cds nanoparticles. *Optics express*, 13(3):867–872, 2005.
- [219] F. Vollmer and S. Arnold. Whispering-gallery-mode biosensing: label-free detection down to single molecules. *Nature methods*, 5(7):591, 2008.
- [220] Z. Wang, W. Guo, L. Li, B. Luk'yanchuk, A. Khan, Z. Liu, Z. Chen, and M. Hong. Optical virtual imaging at 50 nm lateral resolution with a white-light nanoscope. *Nature communications*, 2:218, 2011.
- [221] J. Ward and O. Benson. Wgm microresonators: sensing, lasing and fundamental optics with microspheres. *Laser & Photonics Reviews*, 5(4):553–570, 2011.
- [222] K. A. Willets and R. P. Van Duyne. Localized surface plasmon resonance spectroscopy and sensing. *Annu. Rev. Phys. Chem.*, 58:267–297, 2007.
- [223] A. Winkleman, B. D. Gates, L. S. McCarty, and G. M. Whitesides. Directed self-assembly of spherical particles on patterned electrodes by an applied electric field. *Advanced materials*, 17(12):1507–1511, 2005.
- [224] Y. Xiong, Z. Liu, C. Sun, and X. Zhang. Two-dimensional imaging by far-field superlens at visible wavelengths. *Nano letters*, 7(11):3360–3365, 2007.
- [225] Y. Yan, L. Li, C. Feng, W. Guo, S. Lee, and M. Hong. Microsphere-coupled scanning laser confocal nanoscope for sub-diffraction-limited imaging at 25 nm lateral resolution in the visible spectrum. *Acs Nano*, 8(2):1809–1816, 2014.
- [226] G. Yang, D. Guan, W. Wang, W. Wu, and Z. Chen. The inherent optical nonlinearities of thin silver films. *Optical Materials*, 25(4):439–443, 2004.
- [227] H. Yang, N. Moullan, J. Auwerx, and M. A. Gijs. Super-resolution biological microscopy using virtual imaging by a microsphere nanoscope. *Small*, 10(9):1712–1718, 2014.
- [228] S. Yang and V. N. Astratov. Photonic nanojet-induced modes in chains of size-disordered microspheres with an attenuation of only 0.08 db per sphere. *Applied Physics Letters*, 92(26):261111, 2008.

- [229] S. Yang and V. N. Astratov. Spectroscopy of coherently coupled whispering-gallery modes in size-matched bispheres assembled on a substrate. *Optics letters*, 34(13):2057–2059, 2009.
- [230] L. Yao, Y.-H. Ye, H. F. Ma, L. Cao, and J. Hou. Role of the immersion medium in the microscale spherical lens imaging. *Optics Communications*, 335:23–27, 2015.
- [231] R. Ye, Y.-H. Ye, H. F. Ma, L. Cao, J. Ma, F. Wyrowski, R. Shi, and J.-Y. Zhang. Experimental imaging properties of immersion microscale spherical lenses. *Scientific reports*, 4:3769, 2014.
- [232] R. Ye, Y.-H. Ye, H. F. Ma, J. Ma, B. Wang, J. Yao, S. Liu, L. Cao, H. Xu, and J.-Y. Zhang. Experimental far-field imaging properties of a $\sim 5\text{-}\mu\text{m}$ diameter spherical lens. *Optics letters*, 38(11):1829–1831, 2013.
- [233] K. Yi, H. Wang, Y. Lu, and Z. Yang. Enhanced raman scattering by self-assembled silica spherical microparticles. *Journal of applied physics*, 101(6):063528, 2007.
- [234] C. R. Yonzon, C. L. Haynes, X. Zhang, J. T. Walsh, and R. P. Van Duyne. A glucose biosensor based on surface-enhanced raman scattering: improved partition layer, temporal stability, reversibility, and resistance to serum protein interference. *Analytical Chemistry*, 76(1):78–85, 2004.
- [235] K. Yoshitsugu and I. Ueno. Effect of suspended particles on spreading of volatile droplet on solid substrate. *Journal of visualization*, 14(3):285–294, 2011.
- [236] P. Yunker, A. Yodh, and T. Still. Colloidal shape effects in evaporating drops. *Physics of Complex Colloids*, 184:447, 2013.
- [237] E. J. Zeman and G. C. Schatz. An accurate electromagnetic theory study of surface enhancement factors for silver, gold, copper, lithium, sodium, aluminum, gallium, indium, zinc, and cadmium. *Journal of Physical Chemistry*, 91(3):634–643, 1987.
- [238] Y. Zheng, B. Lukyanchuk, Y. Lu, W. Song, and Z. Mai. Dry laser cleaning of particles from solid substrates: experiments and theory. *Journal of Applied Physics*, 90(5):2135–2142, 2001.

PUBLICATIONS

- [1] V. N. Astratov, **A. Brettin**, N. I Limberopoulos, A. Urbas, Photodetector Focal Plane Array Systems and Methods Based on Microcomponents with Arbitrary Shapes. June 13, 2018, US Patent 16/006,963
- [2] **Brettin, A.**, Blanchette K. F., McGinnis C. L., Abolmaali F., Nesmelov Y. E., Limeropoulos N. I., Walker Jr D. E., Anisimov I., Urbas A. M., Poffo L., Maslov A. V., Astratov V. N. (2018) Microspherical nanoscopy using localized plasmonic structured illumination without postimaging processing. Appl. Phys. Lett. submitted.
- [3] Abolmaali, F., **Brettin, A.**, Green, A., Limberopoulos, N. I., Urbas, A. M., Astratov, V. N. (2017). Photonic jets for highly efficient mid-IR focal plane arrays with large angleofview. Optics express, 25(25), 31174-31185.
- [4] Klibanov, M. V., Koshev, N. A., Nguyen, D. L., Nguyen, L. H., **Brettin, A.**, Astratov, V. N. (2018). A numerical method to solve a phaseless coefficient inverse problem from a single measurement of experimental data. arXiv preprint arXiv:1803.01374.
- [5] Abolmaali F., Poffo L., **Brettin A.**, Walker D. E., Limberopoulos N. I., Anisimov I., Urbas A. M., Maslov A. V., Astratov V. N. (2018 July) Observation of the resonantly enhanced resolution of imaging of fluorescent nanospheres due to their coupling to the metallic nanoplasmonic arrays. In Aerospace and Electronics Conference (NAECON), 2018 (In Press) [Poster presentor award]
- [6] Poffo L., Abolmaali F., **Brettin A.**, Jin B., Page J., Limberopoulos N. I., Anisimov I., Vitebskiy I., Urbas A. M., Maslov A. V., Astratov V. N. The Art of the Impossible: Sorting Dielectric Microspheres by using Light. In Aerospace and Electronics Conference (NAECON), 2018 (In Press)
- [7] **Brettin A.**, Abolmaali F., Limberopoulos N. I., Green A., Anisimov I., Urbas A. M., Astratov V. N., (2018 July). Towards fabrication of mid-IR FPAs with enhanced sensitivity and reduced dark current by using integration with microspherical arrays. In Aerospace and Electronics Conference (NAECON), 2018 (In Press)
- [8] **Brettin A.**, McGinnis C. L., Abolmaali F., Limberopoulos N. I., Walker Jr. D., Urbas A. M., Poffo L., Maslov A. V., Astratov V. N. Superresolution imaging of fluorescent nanospheres by using high-index microspheres embedded in slabs with illumination provided by plasmonic array. In Aerospace and Electronics Conference (NAECON), 2018 (In Press)
- [9] **Brettin A.**, Limberopoulos N. I., Anisimov I., Urbas A. M., Astratov V. N. Microconical arrays as novel light-concentrating structures for enhancing sensi-

- tivity, angle-of-view, and reducing dark current of mid-IR FPAs. In Aerospace and Electronics Conference (NAECON), 2018 (In Press)
- [10] Astratov, V. N., **Brettin, A.**, Abolmaali, F., Poffo, L., Maslov, A. V. (2018, July). Plasmonics and Superresolution in Microspherical Nanoscopy. In 2018 20th International Conference on Transparent Optical Networks (ICTON) (pp. 1-4). IEEE.
- [11] Astratov, V. N., **Brettin, A.**, Abolmaali, F., McGinnis, C. L., Blanchette, K. F., Nesmelov, Y. E., Urbas, A. M. (2017, July). Spotlight on microspherical nanoscopy: Experimental quantification of super-resolution. In Transparent Optical Networks (ICTON), 2017 19th International Conference on (pp. 1-4). IEEE
- [12] **Brettin, A.**, McGinnis, C. L., Blanchette, K. F., Nesmelov, Y. E., Limberopoulos, N. I., Walker, D. E., Astratov, V. N. (2017, June). Quantification of resolution in microspherical nanoscopy with biological objects. In Aerospace and Electronics Conference (NAECON), 2017 IEEE National (pp. 189-192). IEEE.
- [13] Astratov, V. N., Maslov, A. V., **Brettin, A.**, Blanchette, K. F., Nesmelov, Y. E., Limberopoulos, N. I., Urbas, A. M. (2017, February). Contact microspherical nanoscopy: from fundamentals to biomedical applications. In Nanoscale Imaging, Sensing, and Actuation for Biomedical Applications XIV (Vol. 10077, p. 100770S). International Society for Optics and Photonics
- [14] Abolmaali, F., **Brettin, A.**, Limberopoulos, N. I., Urbas, A. M., Astratov, V. N. (2017, February). Use of photonic jets produced by dielectric microspheres for increasing sensitivity and angle-of-view of MWIR detectors. In Smart Photonic and Optoelectronic Integrated Circuits XIX (Vol. 10107, p. 101070V). International Society for Optics and Photonics.
- [15] Solomon, J., Pruthi, T., **Brettin, A.**, Astratov, V., Nesmelov, Y. (2017). Surface plasmon resonance reflects diameter of actin structures decorated with gold nanorods. In APS March Meeting Abstracts.
- [16] **Brettin, A.**, Abolmaali, F., Limberopoulos, N. I., Walker, D. E., Urbas, A. M., Astratov, V. N. (2016, July). Imaging of two-dimensional nanoplasmonic structures by nanoscopy with contact microlenses and various microscope objectives. In Aerospace and Electronics Conference (NAECON) and Ohio Innovation Summit (OIS), 2016 IEEE National (pp. 272-274). IEEE.
- [17] **Brettin, A.**, Blanchette, K. F., Nesmelov, Y., Limberopoulos, N. I., Urbas, A. M., Astratov, V. N. (2016, July). Microsphere nanoscopy for imaging of actin proteins. In Aerospace and Electronics Conference (NAECON) and Ohio Innovation Summit (OIS), 2016 IEEE National (pp. 269-271). IEEE.
- [18] **Brettin, A.**, Abolmaali, F., Limberopoulos, N. I., Walker, D. E., Urbas, A. M., Astratov, V. N. (2016, July). Superresolution imaging with contact microspheres:

Importance of numerical aperture. In Transparent Optical Networks (ICTON), 2016 18th International Conference on (pp. 1-4). IEEE.

- [19] Astratov, V. N., Abolmaali, F., **Brettin, A.**, Allen, K. W., Maslov, A. V., Limberopoulos, N. I., Urbas, A. M. (2016, July). Label-free nanoscopy with contact microlenses: Super-resolution mechanisms and limitations. In Transparent Optical Networks (ICTON), 2016 18th International Conference on(pp. 1-4). IEEE.
- [20] Astratov, V. N., Maslov, A. V., Allen, K. W., Farahi, N., Li, Y., **Brettin, A.**, Rothschild, M. (2016, April). Fundamental limits of super-resolution microscopy by dielectric microspheres and microfibers. In Nanoscale Imaging, Sensing, and Actuation for Biomedical Applications XIII (Vol. 9721, p. 97210K). International Society for Optics and Photonics.
- [21] Song, W., **Brettin, A.**, Jacobs, D. J. (2013). Image Charge Solvation Model (ICSM) with Improved Boundary Conditions. Biophysical Journal, 104(2), 507a.